ABSTRACT

Title of dissertation: DESIGN AND FABRICATION OF HIGH-PERFORMANCE INTERBAND CASCADE TUNABLE EXTERNAL CAVITY LASERS

Athanasios Nicholas Chryssis,
Doctor of Philosophy, 2010

Dissertation directed by: Professor Mario Dagenais,
Department of Electrical and
Computer Engineering

The 3–4 μm spectral region, which contains a number of important lines for chemical detection and other civilian and military applications, has proven to be one of the most challenging for semiconductor laser development. Recently alternative interband semiconductor diode laser technologies that have the potential to meet today's high power performance requirements have made groundbreaking progress. The interband cascade laser is one of the leading candidates in that particular spectral region and has recently been shown to operate continuously at room temperature, which is a significant milestone towards the widespread commercialization of the technology. In this work we are going to talk about the fundamental principles of operation of the interband cascade laser, its performance characteristics, and about the design and fabrication of an interband cascade external cavity laser that will impact the chemical sensing and free space communications industries.

Our first goal for this work was to successfully develop a fabrication process

for this new laser, based on a Gallium Antimonide (GaSb) material system. Based on our established Indium Phosphide (InP) process, we fine tuned our etching, dielectric deposition, metalization, annealing and mounting techniques in order to successfully produce ridge interband cascade lasers. Devices were then characterized by doing a series of length dependence experiments to determine critical physical parameters. Parameters like slope efficiency, threshold current density, internal loss, characteristic temperature, wall plug efficiency were extracted for different laser designs, as part of an optimization process of the quantum well structure of our interband cascade lasers. Lower cladding thickness, number of cascades, separate confinement heterostructure doping, heat dissipation and the confinement factor Γ, were found to be five of the most dominant effects affecting the device performance and high temperature operation.

Based on our extensive dielectric coating experience for the near infra red, we were able to create new, broadband, anti reflection coatings specifically designed for the mid-IR. We created a simulation platform that designs double layer dielectric coatings. Based on the desired wavelength, spectral response, reflectivity and the modal nature of the laser's output beam, our program was able to predict coating designs, optimized for ultra low reflectivity. Our designs were grown in our e-beam evaporation facility, with very high control on the thicknesses and indices of refraction of the coating layers, using an *in situ* monitoring technique.

Finally we were able to demonstrate wavelength tunability using our anti-reflection (AR) coated interband cascade lasers inside an external cavity configuration. This is the first demonstration of an interband cascade external cavity laser.

Our tunable laser also demonstrated the widest to date tuning range of 300 nm (208 cm^{-1}).

DESIGN AND FABRICATION OF HIGH-PERFORMANCE INTERBAND CASCADE TUNABLE EXTERNAL CAVITY LASERS

by

Athanasios Nicholas Chryssis

Dissertation submitted to the Faculty of the Graduate School of the
University of Maryland, College Park in partial fulfillment
of the requirements for the degree of
Doctor of Philosophy
2010

Advisory Committee:
Professor Mario Dagenais, Chair/Advisor
Professor Christopher Davis
Professor Thomas M. Antonsen
Professor Martin Peckerar
Professor Lourdes Salamanca-Riba, Deans Representative
Dr. John Bruno, Maxion Technologies Corporation

To my parents

To my brother

To Selinari

To Stella

Acknowledgments

First and foremost I would like to thank my advisor, Professor Mario Dagenais, for giving me a broad insight in the field of semiconductor lasers. Through his involvement with various collaborations, I was able to acquire an exposure to the field I would have never been able to experience otherwise. Coming from a theoretical background, my perception of the world was more abstract and described mostly by Greek letters rather than numbers. With his persistence and commitment, I was able to appreciate the importance of numbers and learn how actually close theory is to reality. For my engineering skills, Professor Dagenais gets most of the credit. After such a long collaboration, occasional disagreements and arguments are inevitable. Notwithstanding, he has always been a source of support in both personal and professional level, and for that I am deeply grateful.

I would also like to thank Dr. John Bruno and Dr. John Bradshaw, from Maxion Technologies Corporation, for their valuable time and for providing us with their priceless laser crystals and resources to our group for research. I would also like to thank Dr. Bruno for his interest in participating in my dissertation committee.

Next in the list is my good friend and colleague Geunmin Ryu. I want to thank him for his patience, but also for his selfless support and contribution to my project. I also want to thank him for his countless hours we have spent discussing during lunch breaks and office meetings. This thesis would have looked very different, had it been without his valued feedback.

Needless to say that my parents as well as my aunt and uncle deserve a lot

of credit. They have been unconditionally supportive all along the process, having showed confidence in all my decisions, demonstrating their love and trust on me.

I would like to thank all my close friends who showed their understanding, love and true excitement especially during the last stretch of my studies.

I want to acknowledge Dr. Sang Mae Lee for showing personal interest in my career, I hope the best for him.

A lot of my appreciation goes to the Fablab staff, in particular Tom Loughran and Jon Hummel, as well as Jay Pyle and Steven from the machine shop. Bryan Quinn and Joe Kselman, thank you for your great support and for making things work for us. It was fun working with all of you.

I thank my roomates Manolis, Polyvios, Vasilis, Fuat, Alp, George but also my friend Dimitris for making home a place I was looking forward to return to after a hard day at work.

I want to thank ESL and the DC crew, Joben, Tsampika, SaraX, Sandrita, Ellada, Sham, Seems, Inbali, Kevin, Nassir, Sinajoon, Mica, Katerrica, Sheiller, Sepehr, Chris, Yolanda, An, Andresi, etc., Nicholaos and Wiebke as well as my Athens crew George, Chris, 4ri5, Saya, the Godfather, Florence, Myrtoulie, and Adam. Mfitrakis, where are you?

Fiona, thank you for tolerating my beloved brother, and for Nicholas and Irene.

I finally want to thank all the professors in my committee who showed genuine interest in my work.

Contents

List of Figures

List of Tables

Chapter 1

Introduction

For a long time after the demonstration of the near infra-red double heterostructure laser, there were no efficient semiconductor light sources that cover the mid (3 - 8 μm) and the far (8 μm - THz) infra-red spectral band. The first technology that was able to achieve efficient room temperature operation in this part of the spectrum, was the Quantum cascade laser (QCL)[3] which is based on intersubband[4] transitions in a staircase geometry that connects multiple active stages in series. The most important milestone of the QCL development was room temperature continuous wave operation, which was first reported by Beck *et al.*[5]. QCLs have access to a very wide spectral region from the mid-IR to the THz region. There are many challenges, however, on either side of the spectrum. One major problem of the QCL was the vertical emission due to selection rule constraints[6] imposed by their intersubband optical transitions. This problem was addressed by Colombelly *et al.*[7] who built a photonic crystal surface emitting laser. This can be very useful in THz lasers where the mode size is very small compared to the

wavelength of the device and edge emission is small due to high facet reflectivity caused by strong diffraction. To further increase the confinement of long wavelength lasers surface plasmon waveguides[8] have been introduced in order to reduce the cladding region size. On the short wavelength side of the spectrum, QCLs are reaching their physical limits, which are determined by the conduction band offset of the barrier (InAlAs) and the well material (AlInGaAs). High performance strain compensated[9] structures have been able to emit at wavelength as short as 3.1 μm[10, 11], however room temperature CW operation has been demonstrated at wavelength no shorter than 3.8 μm[12]. As we can see from figure 2.2, we can further reduce the emission wavelength, and therefore increase the conduction band offset of the barrier material, by introducing Sb[13]. The main disadvantage of QC lasers is that they are inefficient due to the intersubband nature of the light emitting transition. Theoretically, QCLs should only go up to 10% wall plug efficiency (WPE) in CW operation at room temperature[14]. However, Pranalytica inc. has recently demonstrated 8.8 % WPE CW at room temperature with 1kA/cm^2 and very high power output of 1.6 W at 4.6. μm[15]. Recent results from Northwestern University have demonstrated a very high 18% WPE CW at room temperature at 4.65 μm[16, 17], while at cryogenic temperatures ($\sim$40 K) a WPE $>$ 0.5 has been demonstrated[18]. A very high power output of 3.4 W has been demonstrated at 4.8 μm with a large 4.85 W/A slope efficiency and 1.26 kA / cm^2 threshold current density and 0.62 W at 10 μm with a slope efficiency and threshold current density of 2.88 W/A and 0.88 kA/cm^2[19]. High CW operation temperature ($>$358 K) has also been demonstrated[20], which is due in part to the high characteristic temperature

(112 K) of this InP based material system[21].

In the meantime conventional type-I mid-IR InAs and GaSb based quantum well lasers, shown schematically in figure 2.1 and in detail in [22, 23] have been trying to bridge the spectral gap from the short wavelength side[24, 25, 26, 27]. The main limiting factor for these lasers is the lack of valence band offset, which reduces the hole confinement and thus increases the threshold carrier concentration, especially above 2.3 μm. This effect can be compensated by building heavily strained quantum wells[26] or even introducing quinary AlInGaAsSb barriers over InGaAsSb strained quantum wells, which provide us with an additional degree of freedom allowing for independent control of strain and valence band offset[28]. Very high powers up to 10W CW in an array and 1 W CW near room temperature, have been observed at 2.3 μm and 2.5 μm[29, 22, 30]. CW power drops significantly at longer wavelengths, however light emission up to 8 μm has been demonstrated at room temperature[31]. In the mid-IR spectral region, state of the art QW lasers have been able to provide over 300 mW CW[32] at 290 K at 3 μm with 0.1 W/A slope efficiency and 100 A/cm^2 threshold current density, while a much lower output power of 15 mW CW[27] at 285 K at the longer wavelength of 3.36 μm with a 0.015 W/A slope efficiency and 900 A/cm^2 of threshold current density. The characteristic temperature is around 83 K slightly lower than the QCLs but still high compared to the interband cascade lasers (ICLs).

In order to get around the hole confinement problem we have with the mid-IR QW lasers, a new InAs/GaInSb material based system was proposed by R. Q. Yang[33]. ICLs are illustrated schematically in comparison to QCLs in figure 2.4.

ICLs have a hybrid design that combines the benefits of the traditional diode lasers and the QCLs. They feature a type-II[34] interband transition in combination with a cascaded active region as was introduced in the QCLs. ICLs were introduced in 1995, then the first optically pumped RT laser was demonstrated in 1998[35], the first pulsed RT operation in 2002[36] and the first CW operation at RT in 2008[37, 38]. State of the art ICLs can operate CW at RT and can emit more than 50 mW output power[39] with a slope efficiency greater than 0.16 W/A and threshold current density as low as 400 A/cm^2. ICLs have exhibited a maximum CW operating temperature of 335 K and a maximum WPE of 2.8 % at RT while at 80 K WPE exceeds 30 %. Although ICLs have not yet been able to demonstrate higher efficiency over their QCL counterparts there is a lot of potential for improvement and optimization of the quantum design, due to the more efficient nature of the interband transition. LEDs emitting at long 5-8 μm wavelengths[40], as well as IC vertical cavity surface emitting lasers (VCSELs)[41] have also been demonstrated.

Our research goal was to study and improve laser structures that have been provided by Maxion Inc. and build tunable laser sources. In the process of achieving that goal we have done a thorough analysis of this material system. Starting from optimization of the quantum design, through length dependence analysis, beam propagation analysis (BPM), thermal analysis, then later by designing and implementing a new material system for ultra low reflectivity anti-reflection (AR) coatings, which would also be reliable and avoid delamination due to the coating thickness scaling with the design wavelength. Finally we designed and implemented the first IC tunable external cavity laser with a broad tuning range. Although there

have been tunable light sources based on voltage induced Stark shifts[42], we were able to achieve a large tuning range of 300 nm, which is almost 9% of the emission wavelength and which has enormous military as well as commercial application potential. Applications include local and remote chemical sensing, free-space optical communications, IR countermeasures, and IR lidars. For most applications, lasers are required that can operate under CW conditions at ambient temperatures or at temperatures accessible to thermoelectric coolers ($T > \sim 240$ K). Access to the mid-IR permits targeting of strong coupling to the fundamental rotational-vibrational modes of molecules like CH_4, N_2O, CO_2, CO, NO, H_2O, NH_3, C_2H_4, COS, SO_2, C_2H_5OH and C_2HO each of which can have significant application in medicine (e.g.: NH_3 or $^{13}CO_2$ breath tests for gastric disease[43], CO/CO2 ratios to monitor neonatal jaundice, asthma, and lung capacity), to industry (e.g.: H_2O trace gas monitoring in semiconductor chip manufacturing for moisture control, detection of C_2H_2 as trace contaminant of C_2H_4 reagent gas in polyethylene production[44], CO/CO_2 ratios as a measure of combustion efficiency in furnaces and reactors), and to the environment (e.g.: automobile exhaust gas monitoring and other aspects of atmospheric sensing, ambient trace NH_3 gas concentrations in agriculture or in industrial leakages [45, 46, 47, 48]). This strong coupling can provide orders of magnitude more sensitive absorption spectroscopy compared to its near-IR vibrational overtones according to the high resolution transmission and molecular absorption (HITRAN) database[49]. This allows trace gas detection using traditional [50] as well as novel spectroscopic techniques[51].

In Chapter 2 we present an introduction to this new technology, explaining

its operating principles and key effects affecting the design, fabrication as well as the performance of those Lasers. In Chapter 3 we discuss about device fabrication and present a set of numerical simulations and characterization experiments which helped us narrow down the critical device parameters and their values in order to obtain higher power and room temperature operation lasers. Chapter 4 presents a detailed analysis of multilayered AR coatings, implementation of a plane wave decomposition method for the highly diffracting laser mode, design and development of low reflectivity double layered coatings for the mid-IR. In Chapter 5 the implementation of the broad tunability external cavity laser is presented. In Chapter 6 we conclude with summarizing remarks and suggested future work. Appendix D has a list of our published work, while details on processing, coating reflectivity calculation and ellipsometry are found in Appendices A, B, C.

Chapter 2

Interband Cascade Lasers

2.1 Fundamentals

During the past decade there has been tremendous progress in the field of band structure engineering. It all started when Shockley, Gubanov and Kroemer began studying heterojunctions to be used in bipolar transistors as well as wide gap emitters back in the 1950s. Since then heterojunctions have been dominant in making photonic devices through relaxation of an excited electronic state. Figure 2.1 displays some of the early heterojunction devices. Starting from the top left corner we have the double heterostructure (DH), probably the second simplest photonic device (after the p-n homojunctions), where a narrow bandgap material is sandwiched between a wider bandgap material. The narrow bandgap region is called active region simply because the electronic transition occurs there. The outer, wide bandgap region is called cladding region. The cladding region is typically doped in order to increase the carrier concentration and therefore reduce the resistance of

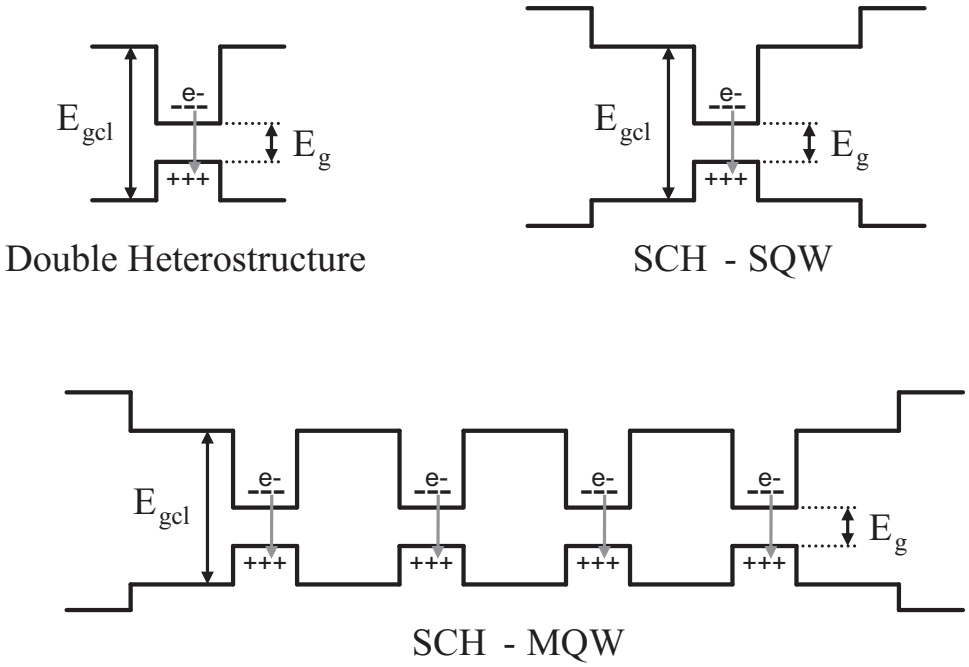

Figure 2.1: Traditional laser types

the device. In our work we did not focus on optically pumped devices, so electrically driven devices are always implied. Under bias, electrons and holes are driven from opposite directions into the active region. Due to the DH conduction and valence band offset, carriers are trapped within the typically undoped active region, where they linger for a time τ (lifetime) until they recombine. When the carriers recombine, they emit light at wavelength:

$$\lambda = \frac{hc}{E} \tag{2.1}$$

where E is the electronic transition energy. This equation can be rewritten as:

$$\lambda(\mu m) = \frac{1.24}{E(eV)} \tag{2.2}$$

In the case of the DH structure, the emitted wavelength is determined by the material bandgap. This does not provide us with flexibility in terms of precise wavelength tailoring, thus quantum well structures were created. At the top right of figure 2.1, a separate confinement heterostructure (SCH) single quantum well (SQW) is depicted. The quantized levels of the well allow us to design an emission wavelength depending on the thickness of the well. The SCH region serves the purpose of capturing carriers. Since the quantum well is very narrow, without a SCH region most of the carriers would either recombine outside the active region or reach the metal contact before they get the chance to do so. Containing carriers with a SCH region allows us to increase the active region carrier density N which determines the optical gain of our device as we will discuss shortly. The SCH and cladding region also play an additional important role in photonic devices. Typically the index of refraction depends inversely on the bandgap of the semiconductor. Therefore if a higher bandgap is used on the outside of a lower badgap region, waveguiding of light in the lower bandgap material takes place. To further improve the gain of a quantum well device the SCH can be modified by adding more quantum wells as shown in the lower part of the figure.

2.2 Material selection

When it comes to selecting which material system will be used for a desired band structure, there are three main parameters that we need to consider and that will determine our starting point in researching the optimal design.

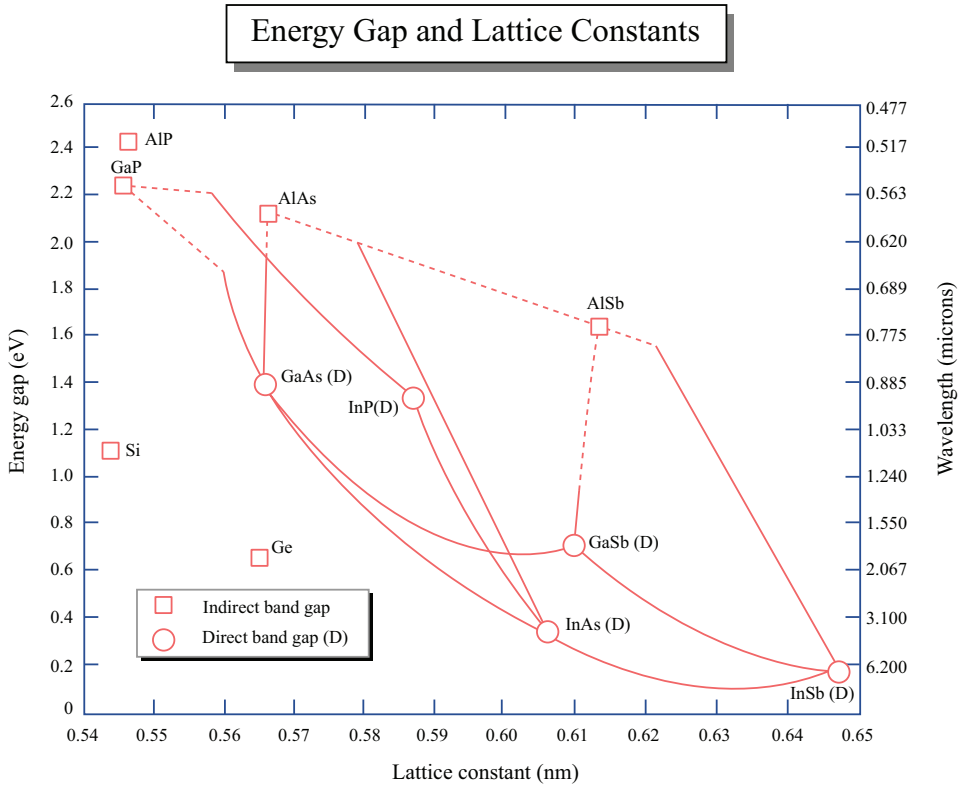

Figure 2.2: Bandgap and latice constant of popular semiconductors.[1]

- Band gap (Figure 2.2)
- Band offset (work function, electron affinity) (Figure 2.3)
- Lattice constant (Figure 2.2)

Regarding the lattice constant, when we have growth of an epitaxial structure, the grown films follow the lattice constant of the substrate. Therefore a film with larger lattice constant than its substrate will be grown under compressive stress while a film with smaller lattice constant will grow under tensile stress. Stress not only has an effect on the bandstructure of the material[52], but it also limits our material selection since heavy stress leads to dislocations which destroy the crystal structure and introduce non radiative states that are undesirable. Typically films

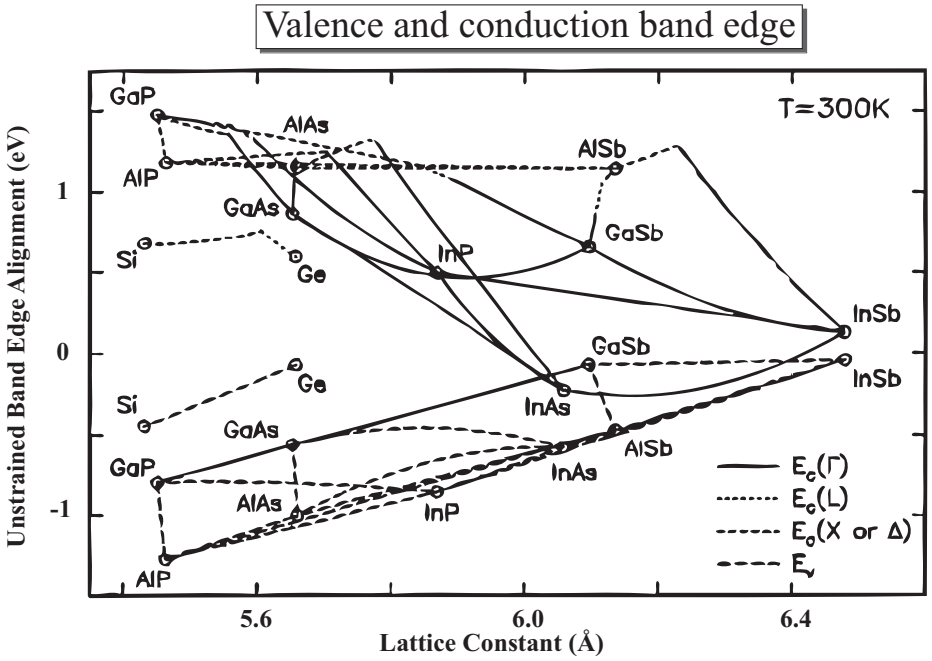

Figure 2.3: Conduction and valence band offset.[2]

are grown with less than 5% stress, since film stress is inversely proportional[53] to the maximum film thickness ("critical thickness") that can be grown without dislocations. One of the most studied material systems is GaAs/AlAs. Among its most important properties is the fact that a replacement of the Ga atom with the Al atom in the crystal structure has a very small effect on the lattice constant, which results in easy film growths with a very small defect density. In any other case where differing lattice constant materials are grown, stress has to be compensated by additional films of opposing stress. Information on the lattice constant and the band gap energy of important semiconductors are illustrated in figure 2.2. It can be seen that AlGaAs ternary devices can be designed to operate in the region of 0.5-0.8 μm wavelength region since they are lattice matched to GaAs substrates. Likewise InGaAsP quaternary devices can operate in the region of 0.9-1.8 μm since

these devices can be lattice matched to InP substrates. InP lasers have extensive application in fiber optic communications, since optical fibers have little absorption in the 1.3 and 1.55 μm wavelength range. Erbium doped fiber amplifiers also operate at 1.55 μm. InP lasers can also be used as pumps for optical amplifiers. GaAs lasers are used in data communications and CDs.

Another candidate material system that satisfies the lattice constant requirement is the InAs/ GaSb/AlSb[54] system. Other than the fact that InAs is a narrow bandgap material, there is something else that makes this system interesting. Figure 2.3 is similar to figure 2.2 but instead it shows the valence (VB) and conduction band (CB) offset with respect to Au. By looking at this figure one might realize that the CB edge of InAs is below the VB edge of GaSb. Additionally AlSb has a large CB offset compared to InAs, as much as 2eV according to Meyer *et al.*[55]. Those properties lead to two important conclusions, first InAs metal contacts do not form Schottky barriers with Au, allowing good ohmic behavior and second a new family of exotic structures can be created. This led Yang and Meyer *et al.*[33, 56] to create the interband cascade (IC) laser, a close relative to the quantum cascade laser (QCL) that was introduced by Faist *et al.*[3]. The difference between the two is that the QC lasers are intersubband lasers, therefore the electronic transition of interest is between two subbands of the same band (typically of the CB). Whereas the interband cascade laser involves type-II transitions between the CB and the VB. This is shown in figure 2.4. Type-II refers to the spatial diagonal nature of the transition. Although diagonal, type-II transition is direct in momentum space and therefore does not require phonon interaction. Although counterintuitive at

first sight, we have to keep in mind that these transitions involve quantum states of quantum wells that have their wavefunctions extending into neighboring materials allowing interaction between the CB and VB states. The large band offset we mentioned earlier allows the creation of type-II transitions with energy separation less than the bandgap of InAs. This enables access to the mid-IR and far-IR part of the spectrum through very efficient processes. In the following sections we will study the principles of operation of those lasers.

2.3 Introduction to quantum and interband cascade lasers

Figure 2.4 shows a qualitative sketch of the distinguishing characteristics of each laser type.

2.3.1 Quantum cascade laser

We are first going to examine the quantum cascade laser illustrated in figure 2.4b. The quantum cascade laser was invented in 1994 by Faist *et al.*[3, 57] and A. Y. Cho, who is also the inventor of molecular beam epitaxy. The QCL is a unipolar device, the carrier transport is conducted in the conduction band of the structure. That simplifies the design considerations and minimizes a variety of non radiative effects that have to be taken into account when designing ICLs, such as interband Auger recombination. The QCL core is comprised of the injection region and the

a) Interband Cascade laser

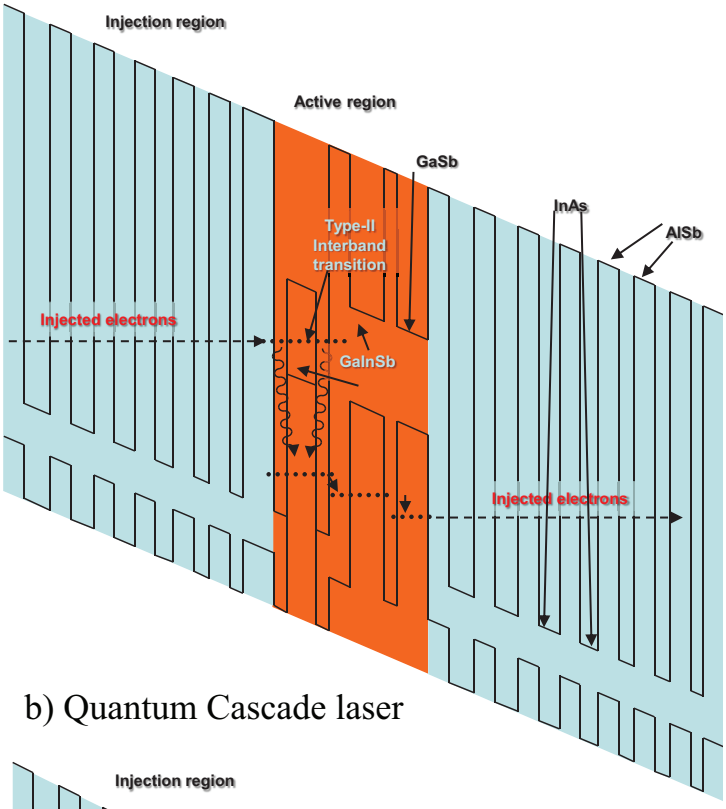

b) Quantum Cascade laser

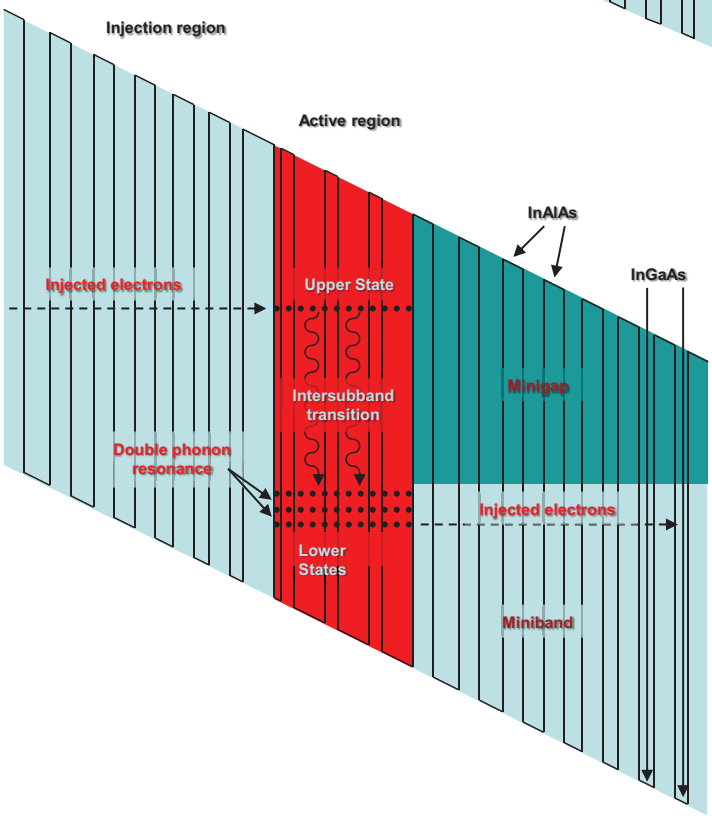

Figure 2.4: Comparison of interband cascade lasers and quantum cascade lasers.

active region.

The injection region is a chirped resonant tunneling structure whose purpose is, under the proper bias, to energize the electrons before they tunnel to the active region where they radiatively relax. The injection region is based on the InAlAs, InGaAs system, which is matched to InP and provides large conduction band offset as shown in figures 2.2 and 2.3. Large CB offset is necessary for confining the carriers and preventing hot electrons overcoming the InAlAs barrier into a band continuum, which would result in carrier leakage.

The active region is comprised of a multiple quantum well structure (four wells in this case). The first well next to the injection region is very narrow. That leads to a high energy eigenstate, which overlaps the wavefunctions on the injection region side, enabling efficient tunneling of carriers, and also the wavefunctions on the active region side are more localized in the three remaining right wells. The illustrated active region has one high energy eigenstate and three low energy eigenstates. Electrons tunneling from the injection region have a lifetime of $\tau = 4.3$ ps before they can non-radiatively relax to the lower states through fast phonon scattering[58]. Therefore, we have to compete with this very fast non-radiative process if we want to achieve population inversion. The three lower states serve as a miniband for a bound to continuum transition[59]. In order to reduce the lifetime of the lower state, a double phonon resonance[60] was introduced. The three wide wells of the active region, are designed such that the three lower energy states are separated by one LO phonon each. We have two LO phonon transitions, thus a double phonon resonance. Originally QCLs were designed with three active region wells instead of four.

However, double phonon resonance in the four well design permits the reduction of the lower state lifetime to 0.2 ps, which is necessary for more efficient lasing.

The minigap region in the illustration indicates that the injection region, which follows the active region, is designed so that there are no energy levels close to or aligning with the upper lasing state. This prevents the electrons from tunneling out of the active region before they can relax to the lower states. Finally the term cascade stands for the fact that the depicted structure gets repeated over and over again so that each electron that gets injected to the active region, can get injected to the active region of the next cascade allowing the possibility of multiple photon emission per electron, which could lead to quantum efficiencies[1] larger than 100%. The number of cascades could be as small as one and as high as 50 or even more.

Even though there has been tremendous progress in QCL development achieving pulsed and continuous wave (CW) operation all the way up to room temperature [61, 62, 63, 64, 5], QCLs are inherently very inefficient, mainly because of the fast phonon scattering processes. State of the art high power QCLs with low threshold current densities[20, 65] are still around 0.57 kA/cm^2 for pulsed mode and 0.81 kA/cm^2 for CW operation, remaining higher than the 0.4 kA/cm^2 threshold current density for the state of the art ICLs[39].

2.3.2 Interband cascade lasers

In this section we are going to explain in detail the operating principles of interband cascade lasers. As we mentioned earlier, ICLs were introduced by Yang

[1] the ratio of generated photons over injected electrons

and Meyer *et al.*[33, 56] and they share many of the fundamental operating principles of QCLs. First and foremost they are both cascade lasers. That means that each electron can produce more than one photon by going through cascaded active regions. Quantum efficiencies of more than 600% have been demonstrated[66] as a result of this. The number of cascades can be as small as one and as big as desired, typically though it is smaller than 20. It seems that high power operation does not depend proportionally to the number of cascades since thermal effects play a very significant role due to the poor thermal conductivity[67] of the IC laser material in contrast to the QC laser material. If we break down the core of the ICL into individual cascades, we get what is illustrated in figure 2.4a. This illustration shows a single cascade of an ICL, which is comprised of an injection region, just like the QCLs, and an active region, which is based on interband transitions rather than intersubband transitions.

Once again the injection region plays the role of gradually increasing the energy of the electrons before they get injected into the active region. Here the material system we use needs to be lattice matched to GaSb. Therefore the large band offset is achieved by using InAs for the well and AlSb for the barrier.

The active region has a double quantum well made of InAs, which defines the upper energy level of the radiative transition. In between the two quantum wells a GaInSb layer is inserted for the hole states. As we mentioned the transition is spatially diagonal and is called a type-II transition, although it is a direct transition in momentum space. Due to the shape of the electron and hole quantum wells this structure is called a "W" structure. Originally in the first demonstration of

ICLs[34, 68, 69], only one quantum well was used. In an attempt to improve the overlap of the electron wavefunction with the hole wavefunction, the W structure was introduced.

Once the electrons get injected into the active region they relax to the GaInSb lower energy level where they tunnel out to the next injection region. The main advantage of the interband cascade lasers is that the in-plane bands have opposite curvature, circumventing the fast phonon scattering, which is a major performance issue in QCLs. In ICLs the upper lifetime is in the order of τ =1 ns. Here the dominant non radiative loss is due to Auger recombination, which we will be analyzed in more detail in the following section. Non radiative recombination due to phonon scattering is not significant and is therefore not accounted for.

Right after the double quantum well region we have another GaInSb region. The purpose of this layer is to prevent carriers in the top lasing level from tunneling out of the active region before they relax. The thicker the GaInSb layer, the less probable that hot electron tunneling would occur. The same GaInSb layers create hole states that align energetically with the hole lower lasing states in order to enhance tunneling of the relaxed carriers to the next injection region. In this case phonon or double phonon resonance is not important since the lower lasing state has already a comparatively very low lifetime compared to the upper lasing state.

2.4 Stress, non radiative loss mechanisms, modulation doping, digital alloying

2.4.1 Stress

In the previous section we highlighted the material selection constraints when growing dislocation free lattice matched structures. Both QCLs and ICLs incorporate structures that have a slight lattice mismatch compared to the substrate.

In the GaSb based ICLs for example the quantum well material is InAs. InAs has a smaller lattice constant than its GaSb substrate lattice constant. Therefore InAs will grow under tensile strain on GaSb. Likewise the AlSb wall of the quantum well has a larger lattice constant than GaSb, therefore AlSb will grow under compressive strain. The same holds for the GaInSb hole layer. QCL and ICL manufacturing requires lengthy MBE cycles resulting in devices that have hundreds or thousands of different layers a few tens of Å thick each, resulting in structures that are a few microns thick. But how can we grow such thick structures under stress without dislocations? The answer is stress compensation. When the laser structure is designed, the thickness of each layer is not only determined by its quantum mechanical properties. The cumulative stress of all layers should amount to zero and each layer should not have a greater thickness than its critical value. The additional degree of freedom that we need in order to accommodate both of those constraints is obtained by tailoring the band structure or by adjusting the alloy composition.

Stress however is not always undesirable. It can be used to reduce the effects

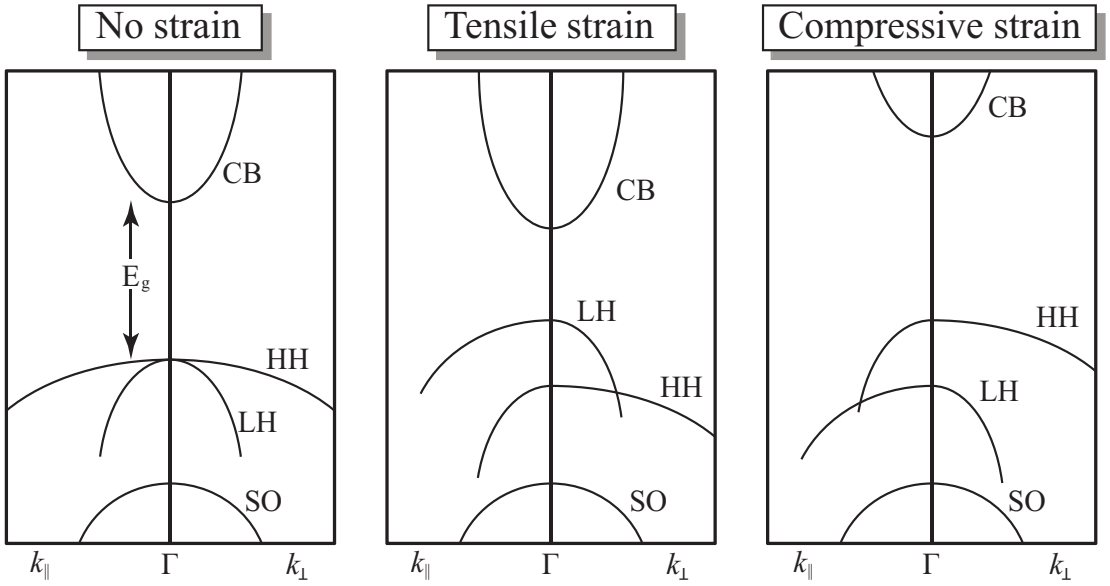

Figure 2.5: Strain effects on the band structure

of Auger recombination as discussed in section 2.4.4. Figure 2.5 illustrates those effects. Γ represents the center of the Brillouin zone of the semiconductor crystal, while $k_{||}$ and $k_\perp$ correspond to the direction parallel and perpendicular to the growth plane.

Under no strain, we can see the three Kane[2] energy band structure where the conduction band (CB) is separated by an energy gap E_g from valence band, whose triple degeneracy is lifted by a spin-orbit[3] (SO) splitting from the heavy hole (HH) and the light hole (LH) bands. The HH and LH bands are named from the hole effective mass at the origin of the Brillouin zone Γ. Bands near Γ can be approximated by a parabolic band structure, which in essence treats carriers as free particles with an effective mass m_{eff} and kinetic energy given by:

[2]The Kane model is a framework of the **k**·**p** perturbation theory for band structure calculation

[3]The interaction of the electron's spin with its motion. Not due to external field.

$$E = \frac{\mathbf{p}^2}{2m_{eff}} = \frac{(\hbar\mathbf{k})^2}{2m_{eff}} \tag{2.3}$$

It is obvious that the larger m_{eff} is, the smaller the curvature of the band becomes.

When we apply tensile strain on our grown film the energy gap tends to decrease while it also separates the LH and the HH band. From figure 2.5 we can see that the LH band gets closer to the CB while the m_{eff} along the epi plane is increasing for the LH and decreasing for the HH. The opposite is observed when we introduce compressive strain. The gap increases and the HH band moves up as the LH band moves down.

Figure 2.6 shows the effects of stress on the quantum well states of the ICL W-well. For the hole states, from figure 2.3 we see that the valence band edge for GaInSb remains fairly constant for various $Ga_{1-x}In_x$ concentrations. The number x, however, will determine the crystal lattice and therefore the amount of compressive stress of GaInSb. That stress will determine the actual band edge for the bulk material, as a result of stress induced band shifting and splitting of the HH and LH bands. In this case the HH band, thus the H_1 quantum state, will move upwards in figure 2.6, closer to the upper energy state than the LH band and thus the L_1 quantum state. This band splitting not only affects the Auger recombination[70], but can also help reduce intervalence band absorption[71], which refers to transitions between the HH, LH and SO bands leading to light absorption. Compressive stress on GaInSb could also help extending the hole wavefunction into potential energy forbidden zones by reducing the m_{eff} of the HH band, allowing more efficient

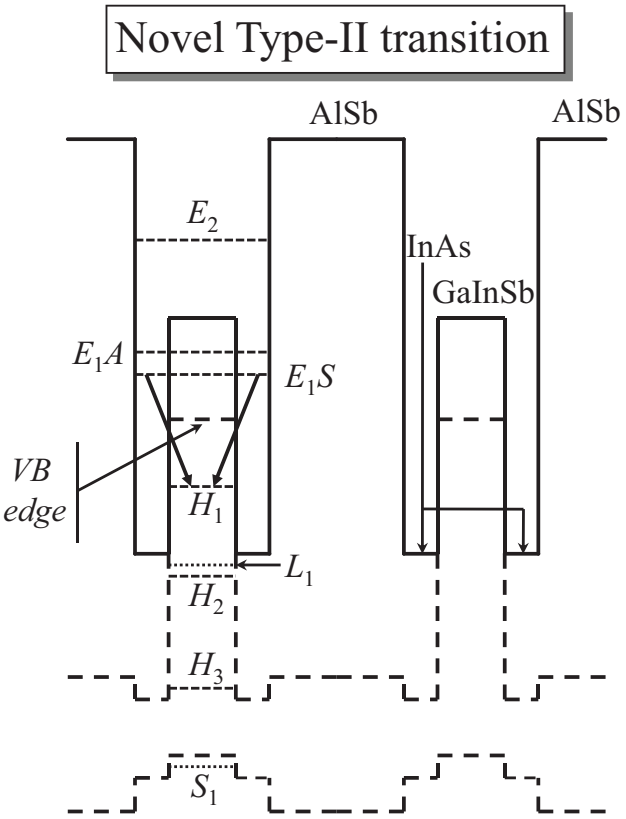

Figure 2.6: Effects of stress on the quantum levels of the interband cascade lasers.

tunneling out of the active region to the injection region, reducing the lower state lifetime. The E_1A (antisymmetric) and E_1S (symmetric) energy doublet, is due to the double InAs quantum well. Both states have similar energy, with the E_1S slightly lower due to its smaller spatial frequency. E_1S also has a longer decay length into the forbidden hole region increasing the electron-hole wavefunction overlap. So our dominant radiative transition should be $E_1S \rightarrow H_1$. Since the strain effects on the conduction band are much less significant, we are not going to talk about the tensile effects on the conduction band of InAs.

The dominant HH radiative transition is also responsible for the polarization of the radiated light. For ICLs the band GaInSb bandstructure favors the HH

transition which generates TE polarized light output. In the case of QCLs, the optical selection rules demand the electric field to be parallel to the epi growth direction, therefore the output light is TM polarized. As a result of that, although both devices can operate as edge emitters, for QCLs its more challenging to create vertical cavity emitters, because for light to come out verticaly, the electric field needs to be parallel to the growth plane.

2.4.2 Random and digital alloying

ICLs and QCLs are extremely complex quantum structures with a very large number of interfaces. Those interfaces can create scattering centers and interfacial states (Shockley-Read-Hall process, SRH) that reduce the quantum efficiency of the laser. That is why absolute control of the interface quality[72] is crucial and research on the effect of the interface bond type (IBT)[73, 74] is still ongoing. For example in the InAs/AlSb system there are two types of interface bonds, one is InSb and the other is AlAs. Due to the length difference of the In-Sb and the Al-As bond, there tends to be interfacial stress linked to the IBT. That can cause stress induced state split off and affect device performance. Obtaining control over the IBT, led to film growth using the technique of digital alloying. In contrast to random alloying where the alloying composition is determined by the effusion cells' fluxes, the alloy composition in digital growth is determined by the duty cycle of the alternating cells. Digital alloying has proved to yield growths with very high structural and optical quality evident from X-ray diffraction (XRD) and photoluminescence (PL)

data[75] and it allows better IBT control.

2.4.3 Modulation doping

To further improve the film quality, modulation doping was introduced. For the case of both quantum and interband cascade lasers, in particular for the InAs/AlSb system, we have seen that there is a very large band offset. Therefore even if there is a deep donor level on the AlSb layer, carriers will immediately drain to the InAs well, until a balance occurs produced by the charge induced electric field. Modulation doping is a preferred doping method since the spatial separation of the ionized impurities from the electrons leads to reduced impurity scattering. That further results in enhanced mobilities in comparison to bulk-doped wells.

2.4.4 Non-radiative Auger recombination

The three principal recombination mechanisms in semiconductors by which thermodynamic equilibrium is established are the Schockley-Read-Hall (SRH) recombination, radiative recombination and Auger recombination as shown in figure 2.7. In this section we are going to analyze in more detail the Auger recombination process shown in 2.7c.

The first important remark is that the Auger recombination is a three body effect. One electron carrier has to recombine with a hole carrier while the generated energy is absorbed by a third carrier. In the case of intrinsic semiconductors where the electron and hole carrier densities are equal ($n = p$), the Auger recombination

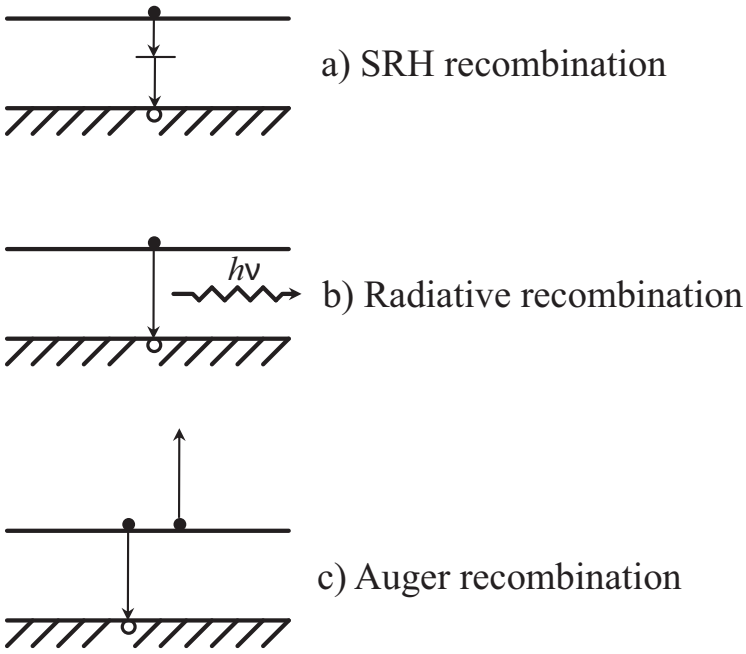

Figure 2.7: Main electronic processes in semiconductors

rate is proportional to the cube of the carrier's density:

$$R = Cn^3 \tag{2.4}$$

where C is the Auger coefficient. There are three dominant Auger mechanisms as illustrated in figure 2.8:

- CHCC (conduction band - heavy hole, conduction band - conduction band)
- CHSH (conduction band - heavy hole, split off band - heavy hole)
- CHLH (conduction band - heavy hole, light hole - heavy hole)

The allowed processes are dictated by the fundamental laws of conservation of energy and momentum. In the case of figure 2.8, the energy is depicted on the y-axis and the $\mathbf{k}$ momentum is represented by the x-axis. An allowed Auger process would require

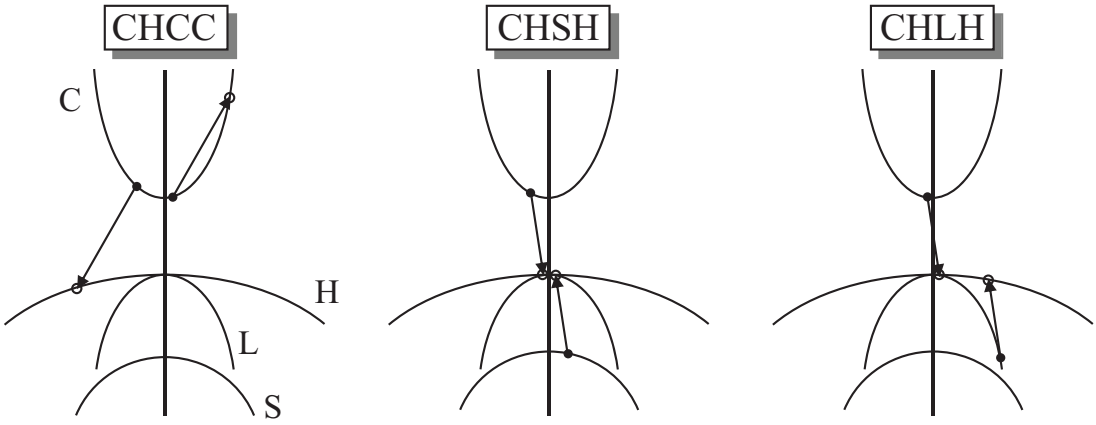

Figure 2.8: Important Auger mechanisms

two vectors, each representing an electronic process, to have the same amplitude and opposite direction. Due to Fermi's exclusion principle, for every transition there needs to be an empty state in each corresponding band. Since most empty states are in the valence band egde, most transitions end up in the heavy hole band. By applying strain in our film and combining the effects illustrated in figures 2.8 and 2.5 we can favor certain processes depending on the band gap, the band splitting and m_{eff} change. Although there are still uncertainties in the IC band parameters[55], band structures calculated using the $\mathbf{k}\cdot\mathbf{p}$ method predict that ICLs avoid direct intervalence resonances with the energy gap leading to reduced Auger rates. Recent studies have shown that a change in strain by varying the $Ga_{1-x}In_xSb$ composition of the hole region, has shown little effect on the Auger coefficient C[76] which is smaller than anticipated in earlier experiments[35], potentially due to the early lower structural quality inducing defect and interface roughness assisted Auger processes[76]. C for ICLs near the 3.5 μm emission wavelength ranges at $3.5 \cdot 10^{-28}$ cm^{-6}/s. Assuming a Boltzmann distribution of carriers, the Auger recombination

factor C for the HH band in a quantum well structure can be shown to have an exponential dependence on temperature:

$$C(T) = C_0 \exp(E_a/kT) \tag{2.5}$$

Also assuming a band shift Δ_s due to stress, this will add an additional exponential factor to the Auger rate of $\exp(\Delta_s/kT)$ due to the band occupancy change.

2.5 Fundamental device characterization theory

The focus of this section will be on chip characterization, and parameter extraction of semiconductor lasers. The study of photon generation requires the separate consideration of the photon concentration N_p and the electric carrier concentration N. N and N_p are correlated through a pair of coupled equations, which individually represent the electronic characteristics, like carrier recombination, and the photonic properties, like modal loss.

2.5.1 Carrier rate equations

In order to calculate the charge carrier concentration N, we need to know their generation rate G_{gen} and their recombination rate R_{rec}. The generation rate is simply determined by the amount of current we pump into the device,

$$G_{gen} = \frac{\eta_i I}{qV} \tag{2.6}$$

I/qV is the injected carrier concentration. In reality only a fraction η_i of the current I manages to get injected into the active region. η_i is called the internal quantum efficiency. Note that η_i is not related to other loss mechanisms like non-radiative recombination or optical loss, all of these effects happen later, after the carriers have been injected.

The recombination rate of the charge carriers can be broken into four parts,

- R_{sp} (Spontaneous emission)
- R_{st} (Stimulated recombination)
- R_l (Carrier leakage rate)
- R_{nr} (Non-radiative recombination)

The non-radiative recombination R_{nr} refers to non radiative transitions like Auger and SRH, while R_l refers to leaking carriers like the ones overcoming the AlSb barrier. R_{sp} refers to colliding carriers that radiatively recombine, it is a two body interaction and is proportional to both carrier densities. For intrinsic semiconductors $R_{sp} \backsim BN^2$ (since $n = p$). For $R_{nr} + R_l \sim (AN + CN^3)$ since, as we already mentioned Auger is a three body interaction, while other effects described by those two parameters are predominantly single, like hot electrons overcoming the injection region barrier, and three body interactions. R_{st} is proportional to the photon density N_p instead, but is also proportional to material gain which can be approximated by $g \approx a(N - N_{tr})$ under small signal conditions. N_{tr} is called transparency carrier density and represents the carrier concentration under which the material has no

gain, so light can travel through the material without being absorbed. Summing up all recombination components will give us:

$$R_{rec} = R_{sp} + R_{nr} + R_l + R_{st} = (AN + CN^3) + BN^2 + R_{st} = \frac{N}{\tau} + R_{st} \tag{2.7}$$

where τ is the carrier lifetime and depends on the carrier concentration N,

$$\frac{1}{\tau} = (A + CN^2) + BN \tag{2.8}$$

Summing up all generation and recombination rates will give us the rate that carrier concentration changes:

$$\frac{dN}{dt} = \frac{\eta_i I}{qV} - \frac{N}{\tau} - R_{st} \tag{2.9}$$

At steady state $\frac{dN}{dt} = 0$, and below threshold $R_{st} = 0$. From equation 2.9 we see that the injection current is proportional to the carrier density at steady state. At threshold the current would be:

$$\frac{\eta_i I_{th}}{qV} = \frac{N_{th}}{\tau} \tag{2.10}$$

2.5.2 Photon rate equations

As we increase the injection current, N gets larger. First it reaches its transparency value N_{tr} and then if we further increase the injection current it is going to reach its threshold value. The transparency carrier density N_{tr} is smaller than the threshold carrier density N_{th} because in order to reach laser threshold we need to

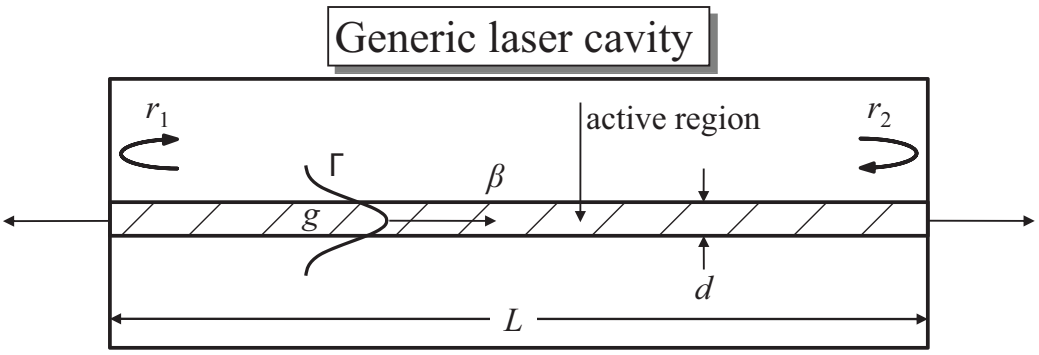

Figure 2.9: Generic laser cavity cross section

overcome additional modal loses a_i and mirror loses a_m. Modal losses are related to now optical losses rather than carrier losses, like waveguide light scattering and free carrier absorption. Mirror losses in the case of semiconductor lasers, refer to the Fresnel reflection of the cleaved facet of the laser waveguide. The index contrast of the interface allows only part of the incident light to escape. Although a_m is called a mirror loss, it is merely so since it is related to the output power of the laser which escapes the cavity, that is the useful output power.

As light is traveling in the waveguide, the photon concentration increases proportionally to the gain coefficient g and the photon concentration value N_p:

$$dN_p = gN_p dz \Rightarrow N_p + \Delta N_p = N_p e^{g\Delta z} \tag{2.11}$$

Figure (2.9) represents the optical cavity of our semiconductor laser. If r_1 and r_2 represent the field reflection coefficients at the facets, a_i represents the internal modal loss and β the propagation constant, at threshold we get:

$$r_1 r_2 e^{(\Gamma \frac{g_{th}}{2} - \frac{a_i}{2})2L} e^{-i\beta 2L} = 1 \tag{2.12}$$

where g_{th} is the gain g at threshold and Γ is called the confinement factor. Equation (2.12) states that at threshold the electric field needs to maintain its amplitude after one full round trip of length $2L$. In order for that to happen we also need to have constructive interference in the cavity, therefore $e^{-i\beta 2L} = 1 \Rightarrow \beta = n\pi/L$ has to be satisfied. The last condition defines the Fabry Perot oscillation modes of the optical cavity. The reason why we use the factor 2 in $g_{th}/2$ and $a_i/2$ is because those parameters are defined for the field intensity which is the square of the electric field. From the real part of (2.12) we get:

$$\Gamma g_{th} = a_i + \frac{1}{L} \ln\left(\frac{1}{r_1 r_2}\right) = a_i + \frac{1}{L} \ln\left(\frac{1}{R}\right) \tag{2.13}$$

where $R = r_1 r_2$ and is bare facet reflectivity if both facets are uncoated and $r_1 = r_2$. We define the factor $a_m = \ln(1/R)/L$ as the mirror loss. We can then write:

$$\Gamma g_{th} = a_i + a_m = \frac{1}{\upsilon_g \tau_p} \tag{2.14}$$

where τ_p is the photon decay lifetime and υ_p is the group velocity of light in the waveguide. In the last equation the internal and mirror loss parameters a_i and a_m affect the whole mode. The g_{th} parameter, however, only applies on the part of the mode that overlaps the active region where light is being generated. In order to treat the mode as a whole we introduce the confinement factor Γ which is the ratio of the mode overlap with the active region.

From equation (2.11) we can derive an expression for R_{st} appearing in equation (2.9).

$$dN_p = gN_p dz \Rightarrow \frac{dN_p}{dz} = gN_p \Rightarrow \frac{dz}{dt}\frac{dN_p}{dz} = \upsilon_p g N_p \Rightarrow \frac{dN_p}{dt} = R_{st} = \upsilon_p g N_p \quad (2.15)$$

Above threshold the carrier density gets clamped at its threshold value. In order to explain this we have to analyze the transient behavior of the gain medium before it reaches steady state. The moment we go above threshold, there is an instantaneous increase of the carrier density N. According to the small signal approximation, near threshold g is proportional to the carrier density N. This instantaneously increases the number of emitted photons N_p according to (2.11) which will in turn increase R_{st} and cancel the carrier increase from equation(2.9). This effect results in a carrier density steady state value of N_{th} even above threshold. If we combine (2.9), (2.10) and (2.15) we get:

$$\frac{dN}{dt} = \eta_i \frac{(I - I_{th})}{qV} - \upsilon_p g N_p \quad (2.16)$$

which under steady state yields:

$$N_p = \frac{\eta_i (I - I_{th})}{q\upsilon_p g_{th} V} \quad (2.17)$$

We earlier defined the mirror loss a_m in a way such that $E_0 a_m dz$ is the light we lose due to partially reflecting facets averaged over a full round trip of the light. E_0 is the optical power confined in the optical cavity $E_0 = N_p h v V_p$. For the power output we get $P_0 = E_0 a_m \frac{dz}{dt}$:

$$P_0 = \upsilon_p a_m N_p h v V_p \tag{2.18}$$

where V_p is the volume of the optical cavity. V is different than V_p because it refers to the volume of the active region where we have optical gain. For the case depicted in figure 2.9 the ratio $V/V_p = \Gamma$. From the equation above we get:

$$P_0 = \eta_i \left(\frac{a_m}{a_i + a_m} \right) \frac{hv}{q} (I - I_{th}) \tag{2.19}$$

by defining:

$$\eta_d = \frac{\eta_i a_m}{a_i + a_m} \tag{2.20}$$

we get

$$P_0 = \eta_d \frac{hv}{q} (I - I_{th}) \tag{2.21}$$

If we differentiate the last equation we get

$$\eta_d = \frac{q}{hv} \frac{dP_0}{dI} \tag{2.22}$$

These last four equations are very important when it comes to laser performance characterization. Note that P_0 refers to the total output power, therefore, if we want to refer to a single, uncoated facet output, we have to multiply P_0 by a factor of 2. The parameter η_d is called the differential quantum efficiency. As we can see from the last equation, it refers to the ratio of photons (dP_0/hv) being produced over the extra carriers being injected above threshold (dI/q).

2.5.3 Basic characterization experiments

Among the most important characterization measurements we can perform on a device are the current, voltage, light output (I-V-L) measurements. Those measurements can help us determine important parameters such as the threshold current I_{th}, the slope efficiency dP_0/dI, the turn on voltage, the differential resistance R_d, the wall plug efficiency (WPE), etc. The analysis that follows allows us to extract additional parameters based on the I-V-L plots by measuring devices of different lengths.

2.5.3.1 Length dependence of the slope efficiency

As we can see from equation (2.13) a_m is a length dependent parameter. Obviously the mirror loss is only determined by the cleaved facet reflectivity. In the way a_m is defined, as an exponent factor of the electric field, its effect decreases at longer device lengths. By substituting a_m into equation (2.19) we get:

$$\frac{hv}{q}\frac{1}{dP_0/dI} = \frac{1}{\eta_i} + \frac{1}{\eta_i}\frac{a_i}{a_m} = \frac{1}{\eta_i} - \frac{1}{\eta_i}\frac{a_i}{\ln R}L \tag{2.23}$$

This equation states that the left hand side factor, which is inversely proportional to the slope efficiency dP_0/dI, is a linear function of the device length. All other parameters like η_i or a_i do not depend on length, and R can be evaluated by knowing the effective index of the waveguide. We mentioned earlier that η_i is the ratio of the electric charge to the total charge that gets injected as carriers in the active region. a_i is the internal optical loss, which mostly depend on the device quantum structure,

but might increase due to waveguide sidewall effects like scattering. For that reason, the sidewall has to be very smooth. Narrow ridge devices tend to have higher value of a_i, therefore, for consistent and meaningful estimation of a_i and to avoid sidewall effects, the length dependent measurements are typically performed on broad area laser devices. The best sidewall quality of a ridge device is obtained by anisotropic wet chemical etching, however for our ICLs we have employed an isotropic etching step instead due to the lack of an anisotropic process for this material system.

By measuring the slope efficiency dP_0/dt of multiple devices at various lengths, we can do a linear fit of the data and extract the following parameters:

$$\frac{1}{\eta_i}\ , \quad \frac{1}{\eta_i}\frac{a_i}{\ln R} \tag{2.24}$$

After calculating η_i, we can calculate a_i assuming R is known. Those two parameters are characteristic of each grown sample and ridge design and provide guidance in optimizing the quantum design of our laser.

2.5.3.2 Length dependence of the threshold current density J_{th}

Another important parametric analysis method is the length dependence of the threshold current density J_{th}. Starting from $g \approx a(N - N_{tr})$ and equations (2.10)(2.13) we get:

$$\left.\begin{array}{c} g = a(N - N_{tr}) \\ \frac{\eta_i I_{th}}{qV} = \frac{N_{th}}{\tau} \\ \Gamma g_{th} = a_i + a_m \end{array}\right\} \quad \left.\begin{array}{c} g_{th} = \frac{dg}{dN}(N_{th} - N_{tr}) \\ \frac{\eta_i I_{th}}{qV} = \frac{N_{th}}{\tau} \\ \Gamma g_{th} = a_i + a_m \end{array}\right\} \quad \boxed{J_{th} = \frac{q}{\eta_i \tau}\left[n_{tr} + \frac{a_i}{\Gamma dg/dn} - \frac{\ln R}{L\Gamma dg/dn}\right]} \tag{2.25}$$

This equation[77] shows the linear dependence of the threshold current density J_{th} over the inverse of the length. Assuming that n_{tr} is small compared to $a_i/\Gamma dg/dn$, we can extract a_i from a linear fit to the length dependent measurements. This will provide a feedback to our earlier measurement of a_i mentioned in the previous section. Note that in the last equation we use n to represent the carrier density. Although N has units of cm^{-3}, n has units of cm^{-2} instead.

2.5.3.3 Dependence of laser parameters on number of cascades

From the two techniques we just mentioned and by measuring the above threshold slope efficiency dP_0/dI and the threshold current density J_{th} at various cavity lengths, we are able to extract the following key parameters:

- a_i (internal loss)
- η_i (internal quantum efficiency)
- η_d (differential quantum efficiency)
- a_m (mirror loss)
- Γ (confinement factor)

How do those parameters depend on the number of cascades? We attributed the internal loss a_i to intervalence band absorption, free electron absorption and sidewall scattering. Assuming that the sidewall effect is negligible, we can claim that a_i is proportional to the number of cascades. η_i has to do with the injection efficiency of carriers to the active region, therefore the number of cascades should not be affected by that number. The differential quantum efficiency η_d is the ratio of emitted photons over injected carriers, so this number should also be proportional to the number of cascades. The mirror loss only has to do with the reflectivity of the cleaved device facet. In order to calculate the confinement factor, we first need to calculate the optical mode inside the waveguide. Then we divide the amount of modal power overlapping the active region over the whole power. In cascade lasers the active region is divided into many stages with interjecting injection regions. Since the gain only depends on the carrier density at the InAs, GaInSb transition layers, we take the spacing between the two InAs quantum wells as the size of the active region. Then Γ is given by the ratio of the total width of all the active regions in the different cascades to the total width of the mode.

2.5.3.4 Temperature dependence of threshold current

Equation (2.10) gives the threshold current dependence on the threshold carrier density N_{th} and the carrier lifetime τ. According to that, N_{th} and τ should dictate the temperature behavior of the threshold current. From (2.10) and (2.7) we get:

$$I_{th} = \frac{qV}{\eta_i}(AN_{th} + BN_{th}^2 + CN_{th}^3) \tag{2.26}$$

As we discussed in (2.5) assuming Boltzmann carrier statistics, the carrier density as well as the Auger parameter C will have an exponential dependence on temperature. Equation (2.26) can therefore be simplified in the following form:

$$I_{th} = I_0 e^{T/T_0} \tag{2.27}$$

T_0 is called the characteristic temperature of the laser and the higher its value, the better and the higher the operating temperature of the device. Typical characteristic temperature for ICLs is around 47 K.

Chapter 3

Experimental results

3.1 Introduction

In this chapter we are going to analyze in more detail and characterize the behavior of our lasers, evaluate critical performance parameters that will allow us to improve the temperature behavior of our devices. Our epi-layers were grown by Maxion Technologies Corporation. After device fabrication in our cleanroom facility, we coat, mount and test our lasers. After a long optimization process we have established our fabrication procedure, which we will elaborate in the following section. For testing our laser to below dew point temperatures ($<\sim 12^{\circ}C$) we created a TE cooled laser testing Dewar which allows access to the emitted light through a transparent mid-IR window.

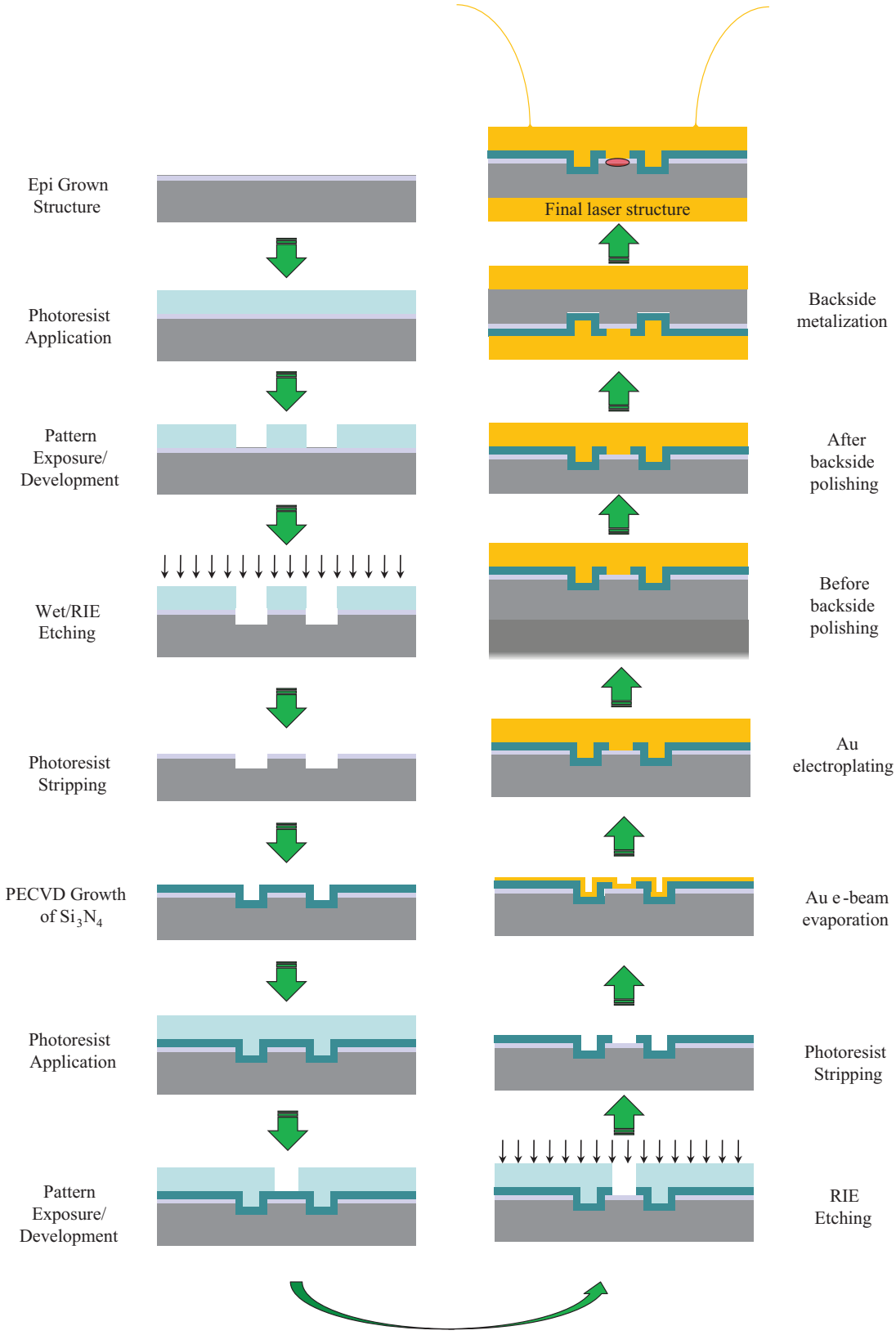

Figure 3.1: Device fabrication process steps.

3.2 Device fabrication

Our starting point is the epi grown GaSb wafer. Our goal is to fabricate a ridge waveguide laser. The process we follow is summarized right below:

- Wafer Cleaning.
- Photolithography of the ridge waveguide using wet etching.
- PECVD of dielectric.
- Dielectric opening patterning and dry etching using RIE.
- Epi side metal contact e-beam evaporation and patterning through liftoff process.
- Backside lapping and polishing.
- Backside metal e-beam evaporation
- Cleaving and dicing

Then depending on what our application goal is, we can:

- AR (anti-reflection), HR (high-reflectivity) coat the facets of our device
- Mount the device epi side up or epi side down on a submount
- Perform wire bonding
- Finally optical alignment for characterization or other practical uses like building an external cavity laser.

Figure 3.1 illustrates the whole process.

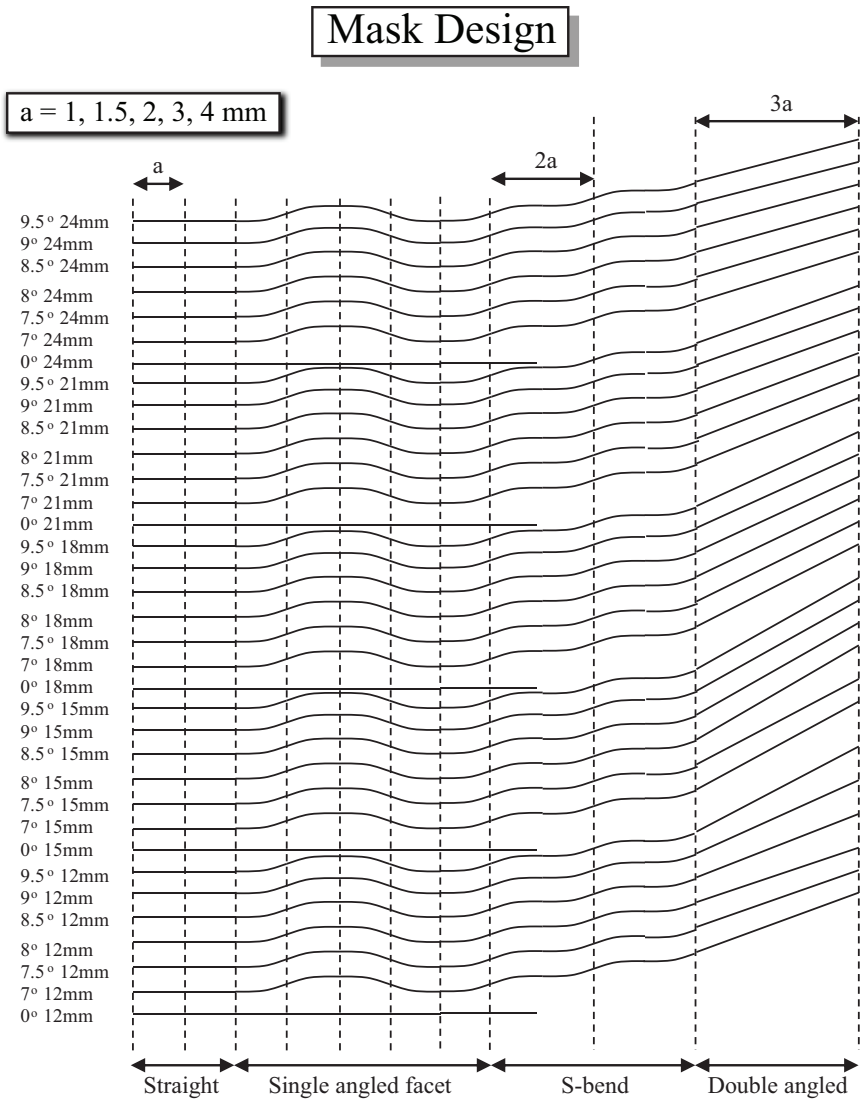

Figure 3.2: Mask Schematic

3.2.1 Fabrication details

The process parameters for each step are discussed here. Detailed process instructions can also be found in appendix B. For the wafer cleaning we first go through a typical solvent cycle, which includes three 30 s individual rinses with acetone, methanol and isopropanol. Then we bake at 120 °C for 10 mins to get rid of all humidity that has potentially impregnated the surface. Finally in order to

make sure that we have no organic residue on the surface we add an extra 100 mW oxygen plasma cleaning cycle at 400 mTorr for 15 secs.

The clean wafers are immediately put on the spinner for Hexamethyldisilazane (HMDS) adhesion promoter and photoresist application. Although HMDS is recommended for use on dielectrics, we have found its use critical for high smoothness sidewalls especially in isotropic wet etching processes. For the etching process we use a solution based on Tartaric acid ($C_4H_6O_6$), Phosphoric acid (H_3PO_4) Hydrogen peroxide (H_2O_2) and deionized water (DI) (H_2O) at a ratio of 5 gr : 30 ml : 30 ml : 90 ml. This is an isotropic etchant for GaSb, but due to the varying etching rate of the different materials of the complex superlattice structure, we observe some undercutting along the sidewall as shown in figure 3.4. For the photolithographic process we used the MicroChemicals AZ5214E photoresist which produces a 1.4 μm thick coating when applied at 4000 rpm. The mask design is illustrated in figure 3.2. The mask was made in such a way so that we can test a variety of design parameters with one processing run, minimizing the expense of precious epi grown laser material. Not depicted in the figure, the mask also featured a few straight broad area lasers as well as tapered waveguides. The various design parameters are summarized right below.

- Device length (a = 1, 1.5, 2, 3, 4 mm)
- Ridge width (w = 12, 15, 18, 21, 24 μm)[1]

[1]Please note that this is not the actual ridge width. The isotropic etching process results in severe undercutting which results to a 7 μm total width reduction for a 3.5μm etch depth.

- Facet angle ($\vartheta = 0°$, 7°, 7.5°, 8°, 8.5°, 9°, 9.5°)
- Device type (Straight, single angled facet, S-bend, double angled, broad area, tapered waveguide)

In the mask we have allowed for various type of devices like double angled facet devices for making semiconductor optical amplifiers (SOA's), but in this study we will primarily study straight waveguides.

After the ridge definition, we deposit 3000 Å of silicon nitride (Si_3N_4) using plasma enhanced chemical vapor deposition (PECVD). Originally we tried to use spin-on as well as e-beam deposited dielectrics, but we ran into coverage problems, especially in the case of spin-on dielectrics, due to the fact that the ridge trench is very deep, resulting in the case of the double trench waveguide, illustrated in fig.3.4, in poor conformal coverage and carrier leakage out of the ridge. The e-beam dielectric resulted in very low quality dielectric layer with poor adhesion that flaked sometimes even during the fabrication process. The PECVD Si_3N_4 layer provides a very good quality layer, uniform and most importantly conformal, even when there is an undercut as shown in the SEM close-up in figure 3.4.

After the PECVD process, we use photolithography to define the dielectric opening. The dielectric opening is shown in figure 3.4.a. It forces carriers to flow through the ridge. The dielectric etching of the opening is performed using directional SF_6 based reactive ion etching (RIE) process. SF_6 etches Si_3N_4 and attacks slightly the photoresist. For that purpose, especially in trenches deeper than 3.5 μm, we use thicker photoresist because its thickness tends to be much smaller near

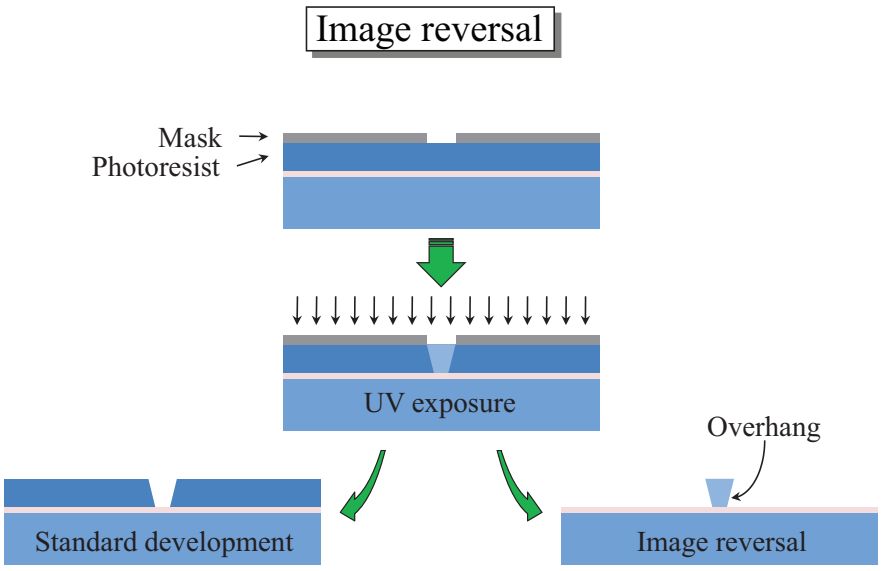

Figure 3.3: Illustration of the image reversal developing process.

the edges of the trench, opposite from the ridge sidewall, and could result in carrier leakage. For that purpose we use the SPR-220 7μm photoresist spun at 6000 rpm creating a film thickness of about 5 μm.

After the dielectric opening we define the metal contact pattern. One important property of the AZ5214E is that it is an image reversal photoresist. That means that after exposure we have the choice to use the photoresist as a negative photoresist. As the photoresist does not get fully exposed right under the edge of the mask features, that creates a small angle on the developed feature sidewall as shown in figure 3.3. The reversed image creates an overhang, which is critical for the metal lift-off process. After the metal evaporation we fully immerse the wafer into a solvent which removes the metal in areas covered by the photoresist. The overhang is essential in achieving metal discontinuity at the contact edges, thus ease of lift-off without the use of potentially harmful ultrasonic bath. Before the metalization we

used a bath of 10% HCl for 30 seconds in order to remove interface native oxidation. Then we subjected our contact interface under Ar^+ ion bombardment for 50 secs, in order to get rid of oxide forming during the sample transfer from the wet bench to the vacuum chamber, before we evaporate a Ti/Pt/Au, 200Å/1500Å/1000Å contact. Ti is used for good adhesion, Pt is used as a diffusion barrier of the Au which is our contact layer and also an oxidation barrier. The ion bombardment has shown to improve our metal adhesion preventing contact delamination occurring under mechanical stress, like during the wire bonding process. It is worth mentioning that originally we tried various recipes for epi[78, 79] and backside[80, 81, 82] metalization as well as a Ti/Ag epi metalization as suggested by Giehl *et al.*[83]. However, we did not observe any improvement in the annealing process, as discussed in section 3.4.3 and especially with the Ti/Ag case, we dealt with adhesion quality problems which lead to impulsive delamination due to high tensile strain of the Au layer[84].

In order to improve the thermal dissipation of our devices especially when we operated our devices CW, we occasionally electroplate our devices with Au. The electroplating occurs after liftoff. We use a Transene, Inc. TSG-250 plating solution and a platinized electrode as our anode. Our sample acts as the cathode, and by vigorous agitation we were able to get a fairly smooth plated coating as shown in figure 3.4b. After plating we evaporate again layers of Pt/Au in order to improve the smoothness and also the quality of the outside Au, as well as to provide a diffusion barrier for the Au for the case of Au/Sn epi down mounting as we will discuss shortly.

At this point the epi-side of our devices are ready. All that is left now is to thin

down and polish the back side and evaporate the backside metal contact. We polish the sample using a standard polishing jig and acetone dissolvable wax for fixing it on the jig. The main reason we thin down the sample is to be able to create a perfectly flat cleaved facets for our semiconductor Fabry Perot cavity avoiding stress induced striations along the facet that scatters the light resulting in large variation of device performance. After polishing down the sample from 500 μm to 100 μm, we scribe the sample with a diamond tip in order to precisely select the cleaving plane.

Cleaving leaves us with laser bars which we then dice for individual devices. The length of the device is determined during the cleaving process. This concludes the IC laser fabrication process. The next step is to coat the devices. This elaborate process is discussed into detail in Chapter 4. Finished devices are mounted and wirebonded, as we are going to discuss shortly, before they can be characterized or used in an optical setup.

3.2.2 Fabricated devices

In figure 3.4 some of the devices we fabricated are illustrated. Those images exhibit some of the fabrication issues we had to deal with and are not therefore representing well performing devices. In 3.4.a we see the effect of not using HMDS on the wafer by comparing the smoothness of the two waveguides at the top and middle left of the figure. The smoother waveguide has also been Au plated for improved thermal dissipation. The edge roughness is detrimental to the device internal loss α_i and is responsible for the large data spread that we have observed when characteriz-

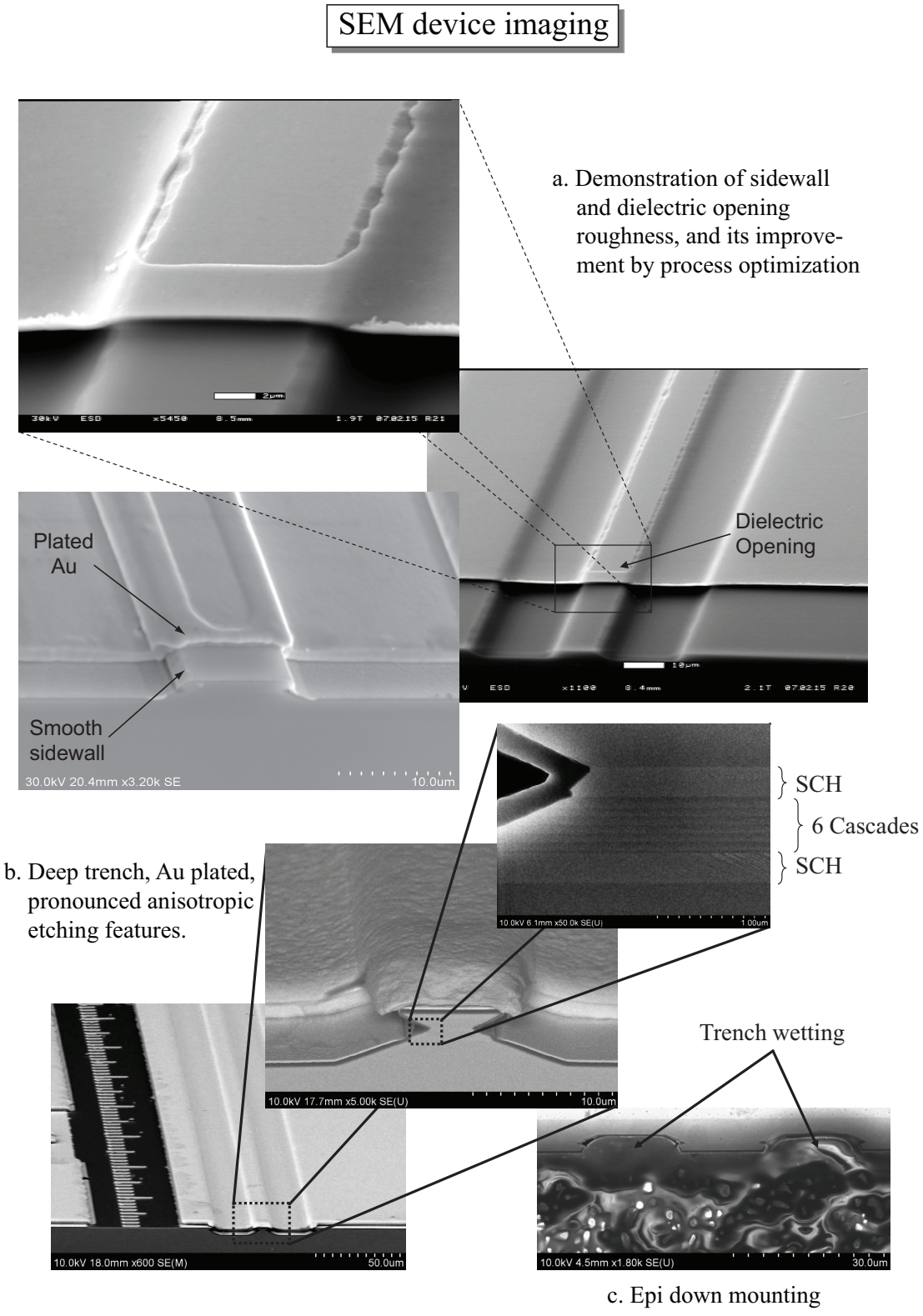

Figure 3.4: SEM of some fabricated devices.

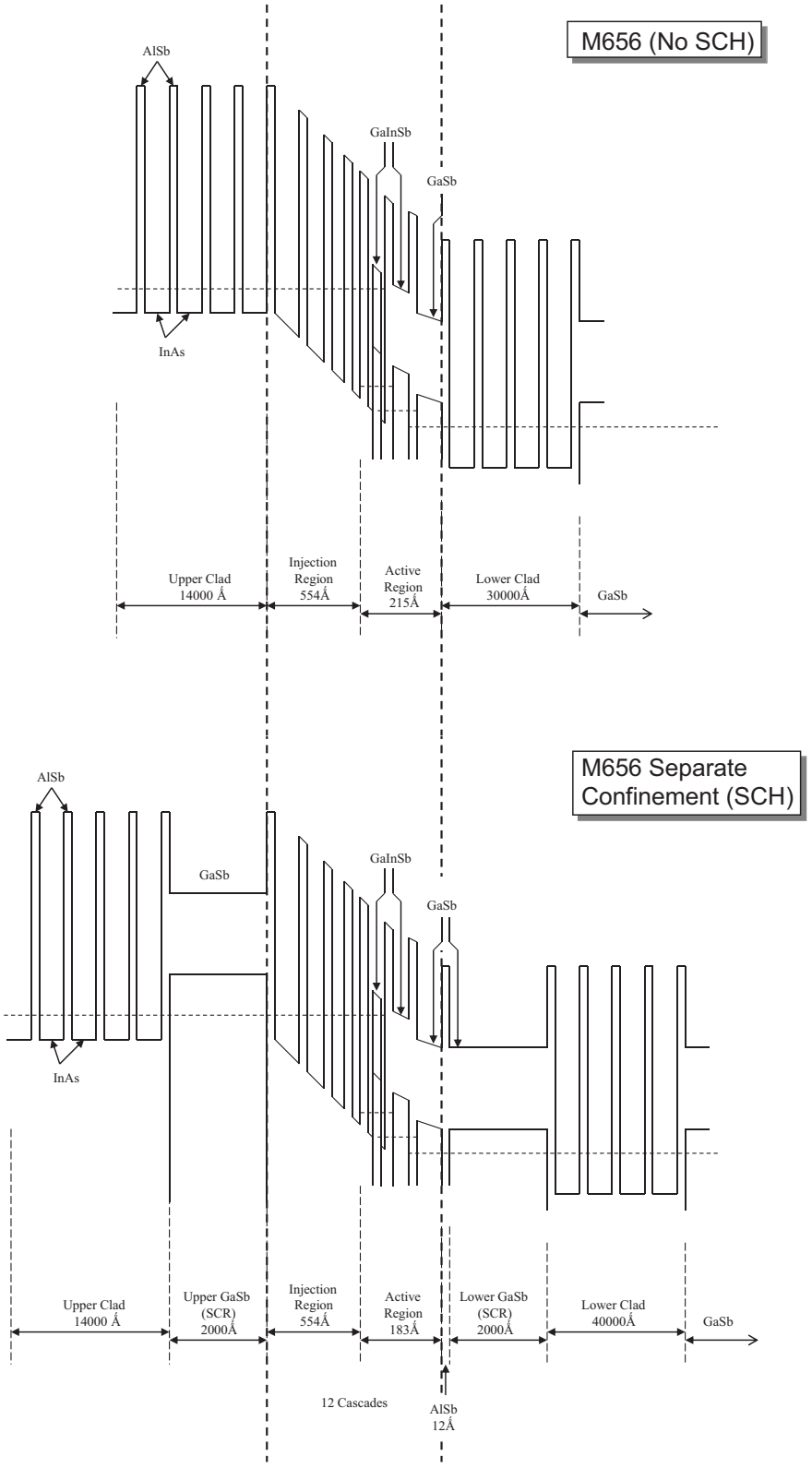

Figure 3.5: ICL epi layers of (top) non-SCH vs (bottom) SCH structures.

ing the laser material. In those same pictures we can also see the dielectric opening and the evaporated contact. In 3.4.b we have a device featuring a deep trench mainly as a consequence of prolonged etching time in order to create narrower ridges, since the appropriate mask was not available. The reason we want to create narrow ridges is because, as we will present in our thermal analysis in a following section, there is significant heat dissipation sideways due to poor cladding thermal[67] conductivity. Not coincidentally, only narrow ridge waveguides have demonstrated CW operation at room temperature[37] while broad area lasers typically still operate at much lower temperatures[85]. In our attempt to create ridges as narrow as 3 μm we were strongly affected by the anisotropic etching of the cladding and the active region which created the undercut illustrated. The void created did not allow conformal metalization and subsequent plating. In combination with increased sidewall roughness induced scattering, those devices underperformed compared to wider devices. By analyzing the active region close-up in 3.4.b, also shown in detail in 3.5, we can distinguish the various constituent layers of our ICLs. At the very top we have the InAs/AlSb top cladding layer. That layer is a superlattice structure (SLS), lattice matched to the GaSb substrate, where carriers resonantly tunnel through. Then we have the GaSb separate confinement heterostructure (SCH) whose original purpose was to increase the confinement factor Γ by attracting the mode closer to the active region due to the GaSb high index of refraction. Coincidentally due to the GaSb's comparatively high thermal coefficient of 33 W/mK compared to 3-4 W/mK for the cladding and the active region, it also acts as an active region heat sink that dissipates heat faster to the plated side of the device. This dual function of the SCH

layer has significantly improved the device performance. The improvement on the confinement factor Γ has been anticipated by numerical calculations and the results are shown in figure 3.6. It is very important to note that in the simulation, Γ is given by the mode overlap with the ICL core (cascade) region which includes both the injection and the active region. In order to obtain the real Γ parameter used in equations (2.12), (2.13) and (2.25) we have to normalize over the thickness of the active, InAs/GaInSb layers, where we have light emitting transitions, divided by the core which includes the injection region. That normalization parameter, based on the structure from Canedy *et al.*[86], is close to 0.09 for the standard W double quantum well active region as shown in figure 3.5. From the numerical simulations we clearly see that the introduction of the SCH improves by almost a factor of 3 the confinement factor Γ especially when the number of cascades is close to 5. This according to eq.(2.25) significantly improves the threshold current density J_{th} and therefore the amount of heat generated at threshold $V_{th} \cdot I_{th}$ that needs to be dissipated to the heat sink.

3.3 Performance improvement strategies

Part of this work was focused in the improvement of the laser performance characteristics. In summary this is a six front battle:

- Reduction of mode coupling to substrate modes
- Optimization of the upper and lower clad thickness for loss reduction

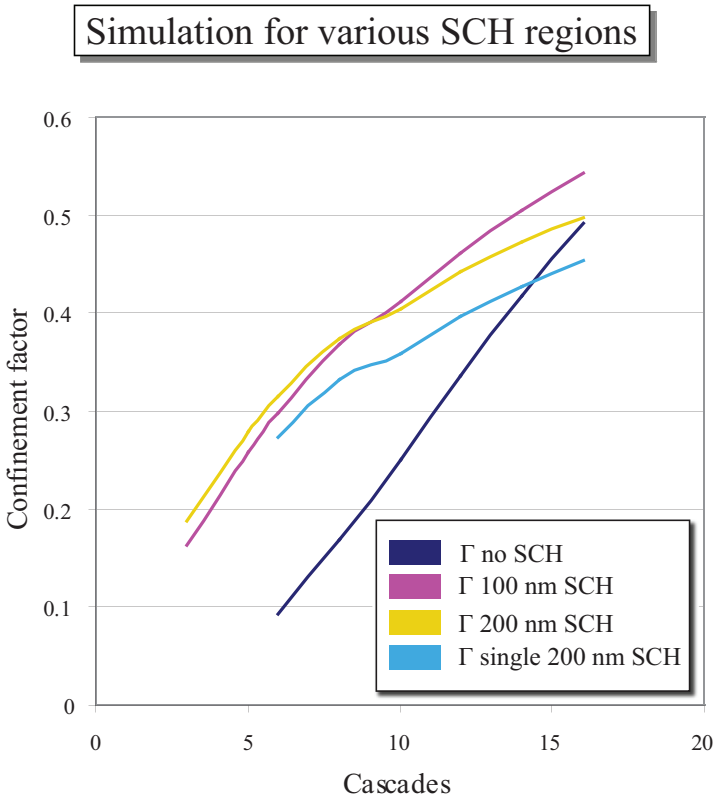

Figure 3.6: Confinement factor numerical simulation results for SCH structures.

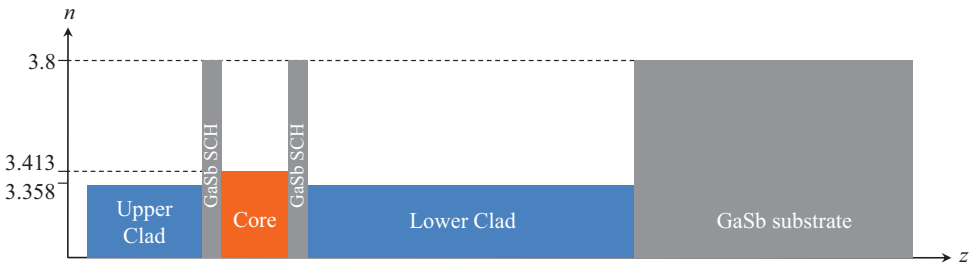

Figure 3.7: Device index profile.

- Efficient dissipation of heat generated in the active region
- Device yield improvement and consistent performance
- Reduction of internal loss a_i
- Reduction of the threshold current density J_{th}

The device yield is something we have already made steady progress on and is very dependent on the waveguide surface quality. The cladding thickness as well as the mode coupling to the substrate is one of the first problems we had to overcome. As we can see from figure 3.7 we can distinguish two issues. First the core has a refractive index similar to the one of the cladding regions, resulting in weak guiding of the mode, and second the GaSb substrate has substantially higher index of refraction compared to the core, allowing the weak guided mode to leak to the substrate. Figure 3.8 shows numerical calculations based on the structures illustrated in 3.5.top. The two plots show the loss coefficient a_i due to mode leakage with respect to the lower cladding thickness as well as the ridge width. We conclude that for lower cladding thickness smaller than 4 μm there is a sharp increase in the mode loss. We also calculated the effect of the ridge width on a_i, which for narrow width value tends to push the mode down to the substrate. That effect is prominent for widths smaller than 6-7 μm. However below that point the increasing loss due to sidewall roughness is gaining significant ground dominating over the substrate leaking effect. Based on these conclusions we have standardized our lower cladding thickness to be 4 μm. As for the ridge widths most of the devices we fabricate have a width around 7-10 μm. We are currently investigating the effect of the upper cladding thickness

reduction on a_i. The effect under study is the mode loss induced by the metal contact. Preliminary study has shown that due to the high conductivity of the contact the mode penetration in the conductor is very small, therefore the loss is not very much dependent on the upper cladding region thickness. Given that the upper clad has bad thermal conductivity, there might be a benefit in reducing the upper clad thickness from the now 1.4 μm to less than 1 μm. This change should proportionally improve the device thermal resistance, which will be introduced shortly. In an attempt to reduce the metal loss we made devices with increased upper cladding thickness of 3 μm. That resulted in a 12.5 % reduction in the slope efficiency. According to eq.(2.25) and figure 3.9, by doing a linear fit on the J_{th} we can get an estimate on the a_i if we assume that n_{tr} is negligible due to the small value of the confinement factor Γ. By dividing the linear fit constants we obtain for the thick upper clad 12.5 cm^{-1} and 17 cm^{-1} for the thin upper clad device. Substituting a_i in equation (2.23) we can extract η_i from the slope of the linear fit on the slope efficiency. Although we can extract η_i from the constant of the linear fit, due to the data spread we have a large error determining the constant value. That is why we use the slope of the fit. Doing that we get η_i of 31 % for the thick upper clad and 48 % for the thin upper clad. The decreasing trend for both the η_i and the a_i when increasing the upper clad thickness, are expected. Reduced η_i values are associated with increased carrier leakage or non radiative SRH recombination due to interfacial states, which is proportionally larger for thicker upper clad structures.

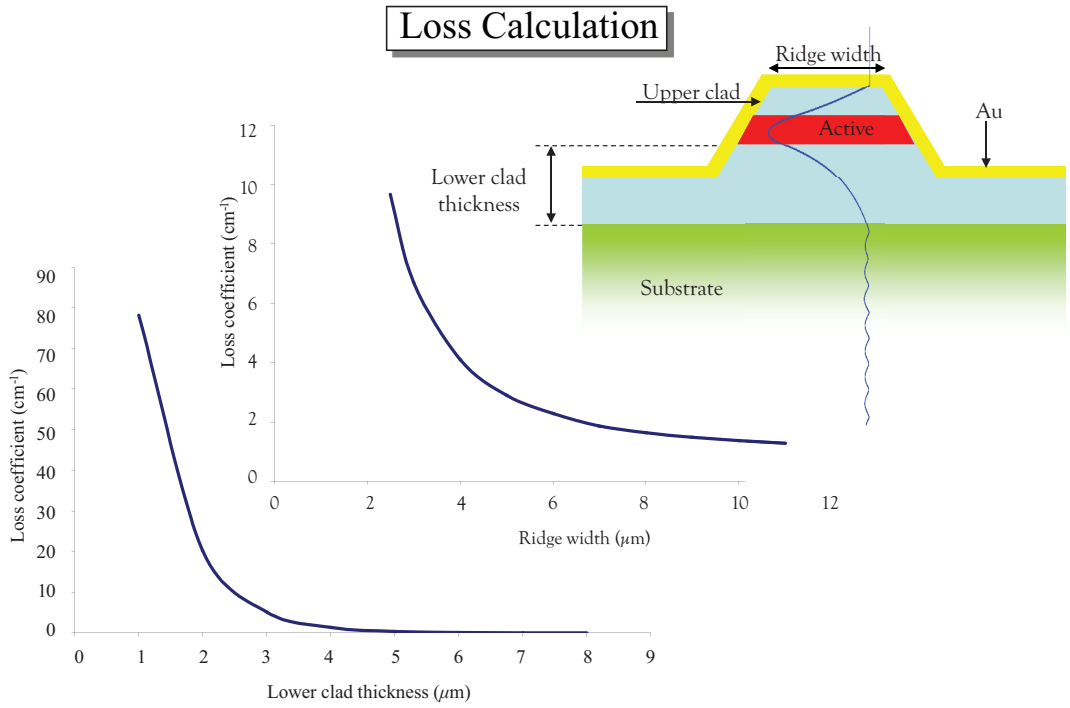

Figure 3.8: Numerical simulation of loss coefficient for varying ridge parameters.

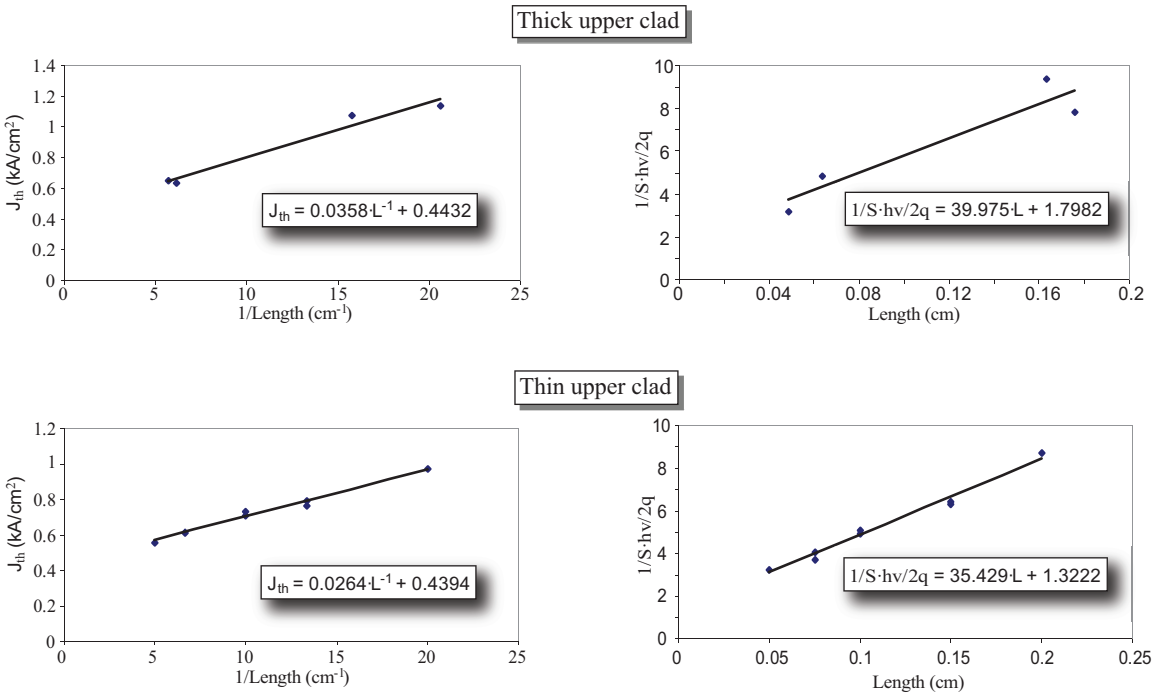

Figure 3.9: Length dependence of thick vs thin upper clad devices. ($2S = {}^{dP_0}/_{dI}$)

Therm. cond. coefficients

Material	k(W/mK)
AlN	140
In	82
Au	317
SiO2	1.4
InAs	27
AlSb	46
Clad	3.6
Active region	4.0
GaSb	33

Table 3.1: Thermal conductivity coefficients for materials of interest in interband cascade lasers.

3.4 Heat generation in interband cascade lasers

3.4.1 Duty cycle effect on power output

One of the most challenging issues of the interband cascade lasers is heat dissipation. Table 3.1 shows the thermal conductivities of the materials used in ICLs. We see that due to very poor clad conductivity heat does not easily escape from the active region. That is why, not only do we need to operate in pulsed mode in order to extract the laser parameters accurately, but also the pulse duration needs to be shorter than 200ns before we start having significant core temperature increase as shown in figure 3.10. In detail figure 3.10 shows at the top the I-L curves at various duty cycles at room temperature. We see that typically for the same duty cycle we get the same peak power as expected. However, when the duty cycle is increased above 5% we start seeing a drop of power due to thermal effects.

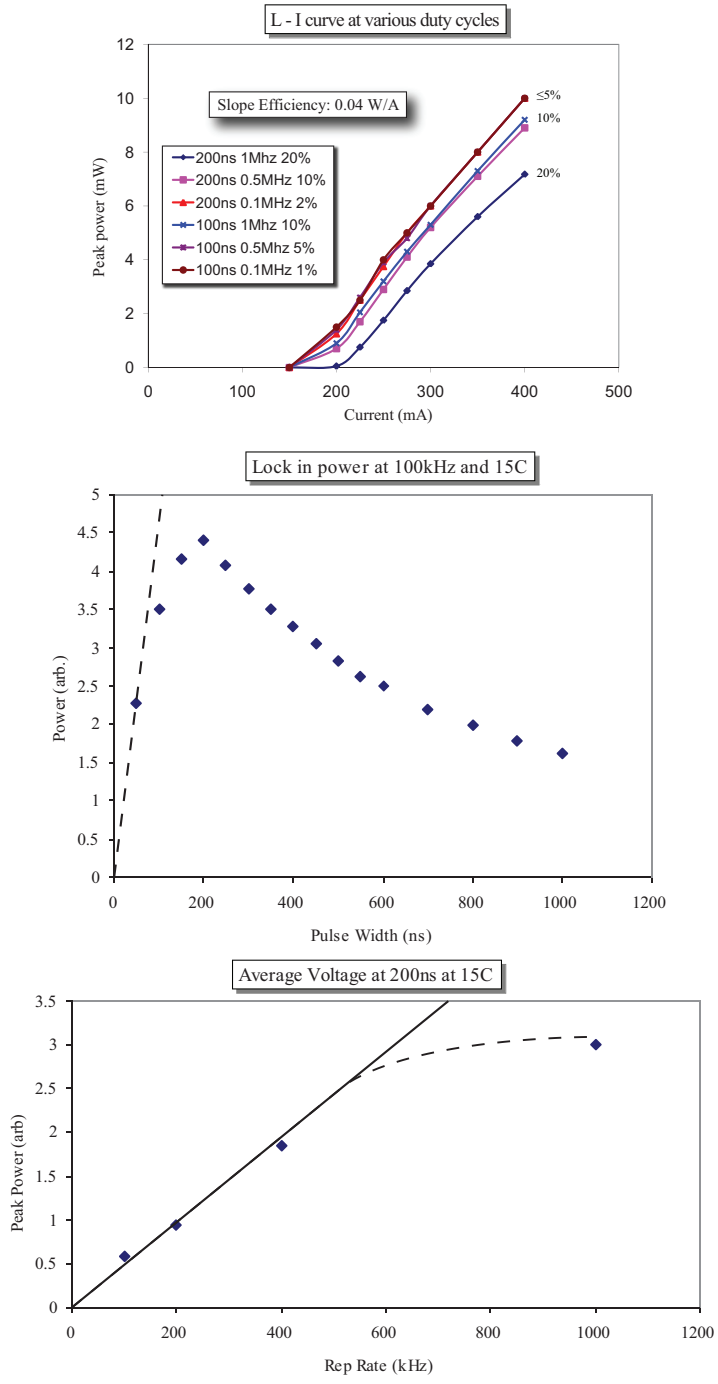

Figure 3.10: Room temperature measurements, (Top) I-L at various duty cycles. (Middle) Pulse power vs. pulse width. (Bottom) Peak power vs. rep rate.

Please note that there is no soft turn-on on those devices. The continuous line is just a smooth line connecting the data points. There are two ways that the duty cycle affects the power output. First, as expected the pulse width affects the power output as shown in the middle plot giving the power vs. pulse width. Theoretically they should be proportional as indicated by the dotted line, however, thermal effects seem to dominate for pulses broader than 200 ns. Second, high rep rate seem to reduce the output peak power as shown at the bottom plot illustrating the peak power vs. rep rate. The pulse power is expected to be proportional to the repetition rate, however for high rep rate heat doesn't have enough time to dissipate before the following cycle. We conclude therefore that for pulsed measurements, in order to avoid thermal effects, the pulse needs to have a pulse width of less than 200 ns and a rep rate less than 1 MHz, or even more preferably less than half of both values.

3.4.2 Thermal resistance and device thermal simulation

Table 3.1 shows the thermal conductivities of each layer of our laser structure. We already pointed out how poor it is for the active and cladding regions. To get an idea of how much it affects the device performance we did a numerical calculation of the heat flow based on a standard 10 μm wide ridge design. For the simulation we used the finite element solver for partial differential equations FlexPDE. In this case the partial differential equation we want to solve is:

$$S = k\nabla T \tag{3.1}$$

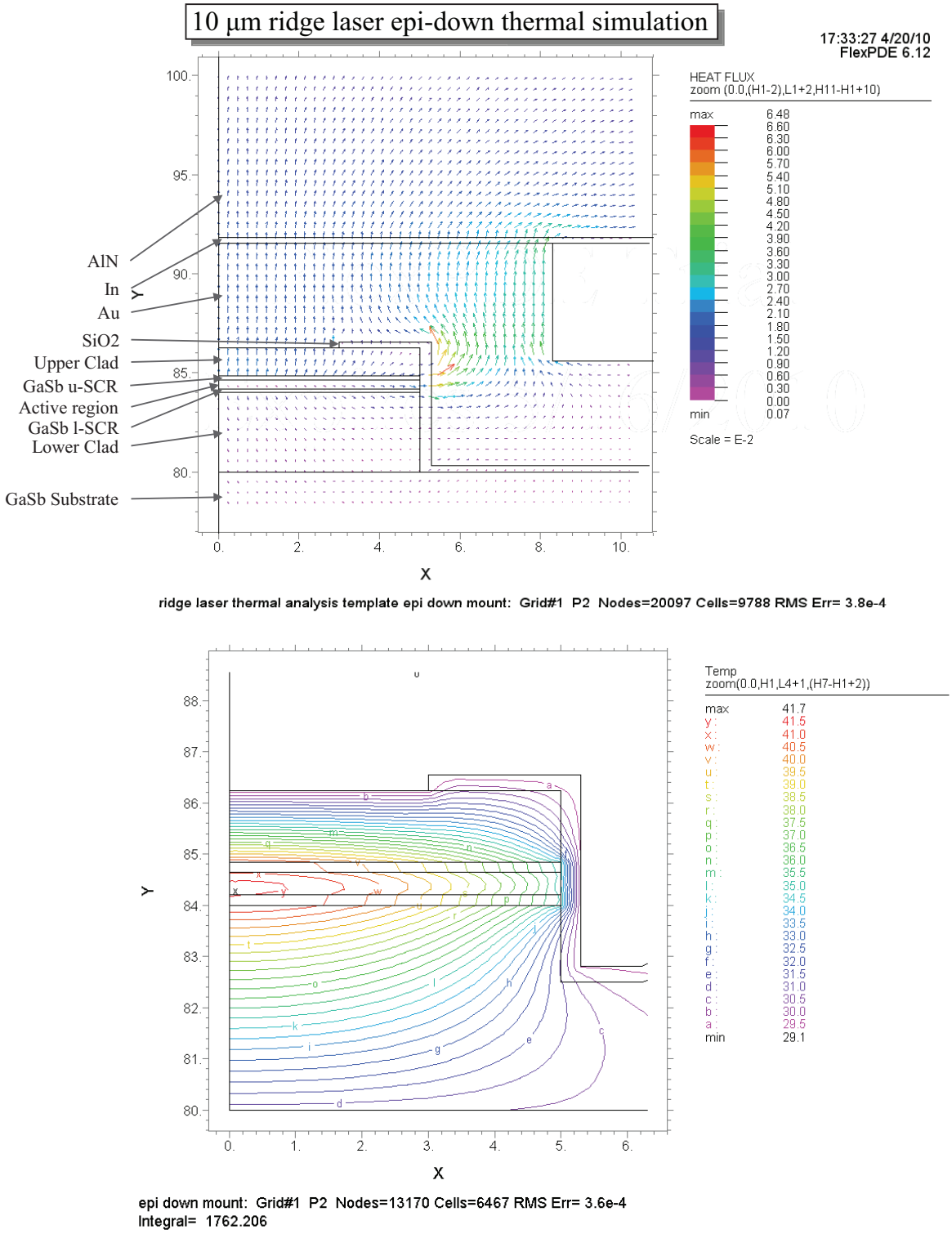

Figure 3.11: Thermal simulation of standard 6 cascade SCH IC laser at room temperature on threshold. (Top) Heat flux, (Bottom) Temperature contour

where k is the thermal conductivity of the material.

T is the temperature

S is the power density

For simplicity we assumed that the material is isotropic so k is a scalar. We tested various scenarios like plated and non-plated devices, epi-up, epi-down etc. In figure 3.11 a 6 cascade, Au plated, device mounted epi down is simulated at threshold. The most important remark here is the strong lateral outflux of heat. This confirms the claim we made earlier that narrow ridge devices can operate CW easier than broad area lasers. The temperature contour is illustrated at the bottom of the figure where we observe a maximum of 41.7 °C active region temperature for a 25 °C heatsink temperature. High power operation of this laser system would require more efficient heat sinking. From the simulation we estimated the thermal resistance of various configurations. The thermal resistance is defined as follows:

$$R_{th} = \frac{\Delta T}{\Delta P} \tag{3.2}$$

where ΔP is the power dissipated on the device (typically $V \cdot I$).

ΔT is the temperature difference between the active region and the heat sink.

This definition of the thermal resistance is specific to the device geometry. The thermal resistance is proportional to the device area. In order to eliminate area dependency we use the following definition of R_{th} for device characterization:

$$R_{th} = \frac{\Delta T}{\Delta P} A \tag{3.3}$$

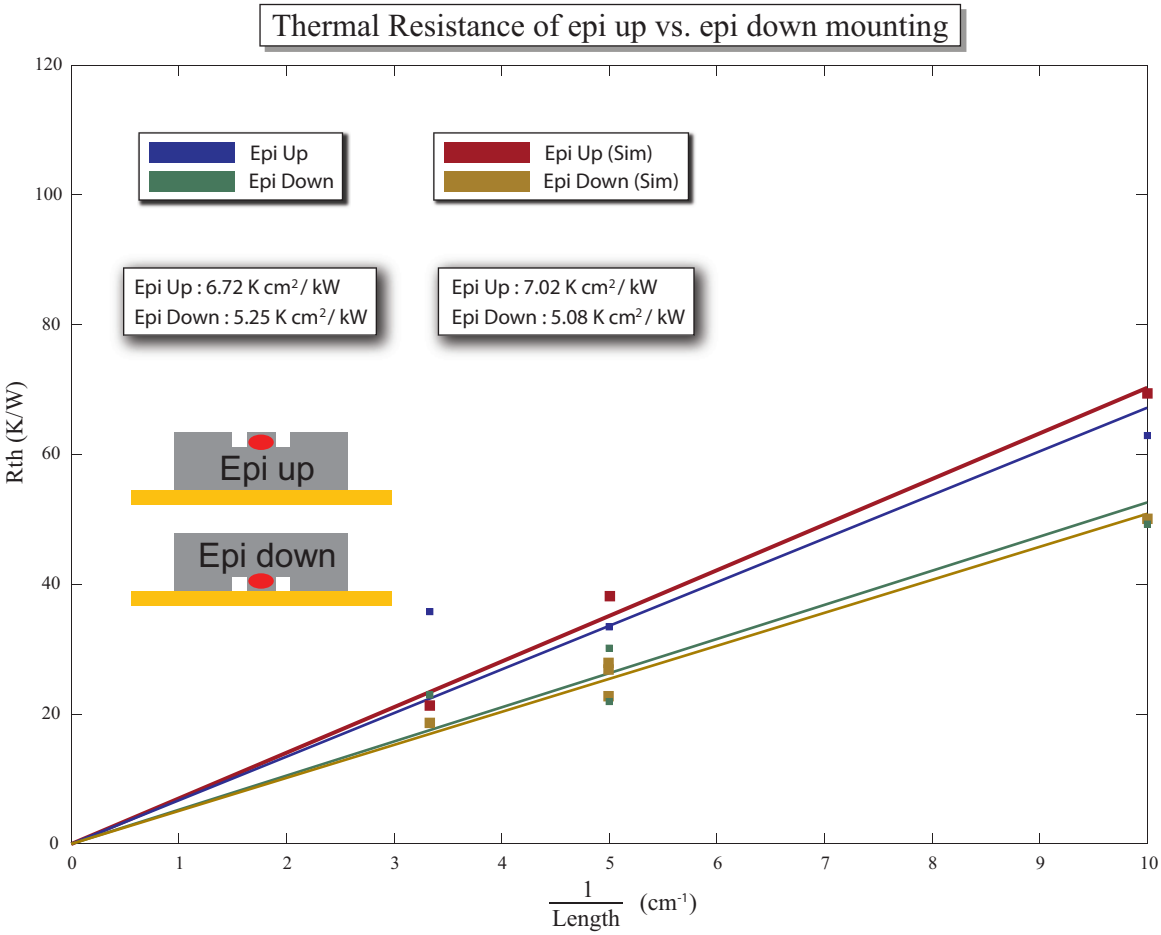

Figure 3.12: Theoretical vs. experimental thermal resistance.

where A is the area of the thermal interface.

The theoretical results of R_{th} were compared with actual R_{th} measurements of real devices. As we can see from figure (3.12), there is good agreement between the experimental and the theoretical results. For the simulated epi-up device we got 7.02 Kcm^2/kW and 6.72 Kcm^2/kW for the real device, while for the epi-down we got 5.08 Kcm^2/kW and 5.25 Kcm^2/kW correspondingly. What is important here is that there is a 4/3 improvement in R_{th} when implementing epi-down mounting.

3.4.3 Epi-down mounting

For the epi down mounting we used Aluminum Nitride (AlN) submounts. AlN is the standard submount used for InP due to thermal expansion coefficient (CTE) match of 4.5 ppm/°C. GaSb however has a CTE of 7.75 ppm/°C and would work better with other ceramic materials like BeO that has a CTE of 8 ppm/°C. For that purpose Au/Sn soldering was not successful. We encountered two problems, first the device would come out of the submount after applying a bit of shear stress (eg. during wirebonding), often peeling the whole contact of the device and second the high melting temperature of the Au/Sn solder seems to deteriorate the device performance. ICLs seem to be particularly sensitive to temperatures above 320 °C. Devices either degrade significantly or become ohmic after soldering or prolonged annealing. A similar effect has been observed while operating the laser at high duty cycle and at high current. However, in the latter case we observed that if we cleave out the facets we can restore device performance. This leads us to the conclusion that there is significant heat build-up at the facets. Our conclusion therefore is that high temperature creates ohmic (shorting) paths, however we have not yet determined the process responsible for this behavior.

In order to overcome the problems above, we decided to use Indium for the mounting of these devices. Indium is soft in contrast with Au/Sn which is hard, and therefore the stress due to the CTE mismatch between the AlN submount and the GaSb substrate is alleviated. Indium is also a low temperature solder, therefore it does not affect the device performance. As shown in figure 3.4.c we have been

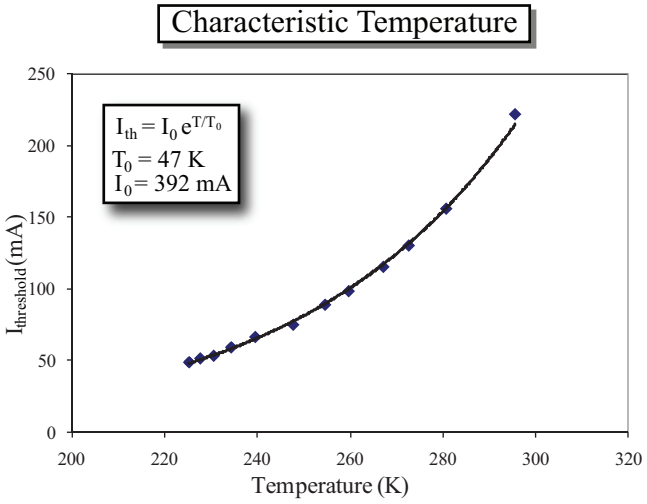

Figure 3.13: Current threshold temperature dependence.

able to get very good wetting of the double trench. The submounts were made by thermally evaporating 3.5 μm of In on AlN. We prefer fluxless soldering, especially when mounting epi-down, therefore the In coated submounts were always prepared right before mounting in order to minimize In oxidation.

3.4.4 Maximum CW temperature

In the last two chapters, we introduced the following expressions (2.19), (2.27) and (3.2):

$$\begin{aligned} P_0 &= \eta_i \left(\frac{a_m}{a_i + a_m}\right) \frac{hv}{q} (I - I_{th}) \\ I_{th} &= I_0 e^{(T+\Delta T)/T_0} \\ R_{th} &= \frac{\Delta T}{\Delta P} \end{aligned} \tag{3.4}$$

where T_0 is the characteristic temperature of the device.

This set of equations describes the CW power output. $\Delta P = V \cdot I$ is the amount

of heat that is generated in the device. The higher the I, the higher the ΔP, the higher the active region temperature ΔT, the higher the threshold current I_{th}, the smaller the output power P_0. For this calculation we are going to have to know T_0 and R_{th}.

The characteristic temperature T_0 is easy to measure. Figure 3.13 shows the threshold current of a 2 mm long, 10 μm wide, 6 cascade laser at various operating temperatures. By fitting with an exponential curve we obtain the characteristic temperature $T_0 = 47$ K, which is typical for ICLs.

Small T_0 is not desirable, however in this case it makes the R_{th} measurement easier. We measure ΔT by operating the same laser in pulsed and CW mode at different temperatures. The selected temperatures are such that both operating modes have the same threshold current. That means that at threshold, we have the same active region temperature for both cases, even though the heat sink temperature is different. Assuming that in pulsed mode the duty cycle is small enough to avoid heating of the active region, as discussed in section 3.4.1, the active region temperature is the same as the heat sink temperature. In CW the way we estimate the active region temperature difference from the heat sink, is by comparing the heatsink temperature difference between the pulsed and CW measurement that gives us the same threshold. This method is quite accurate, however it is based on the fact that the characteristic temperature is small. For devices with large characteristic temperature, estimation of ΔT requires very accurate measurement of the threshold current. There are other methods[87] to measure ΔT that go around that problem, however the main advantage of this method is that it is very simple to

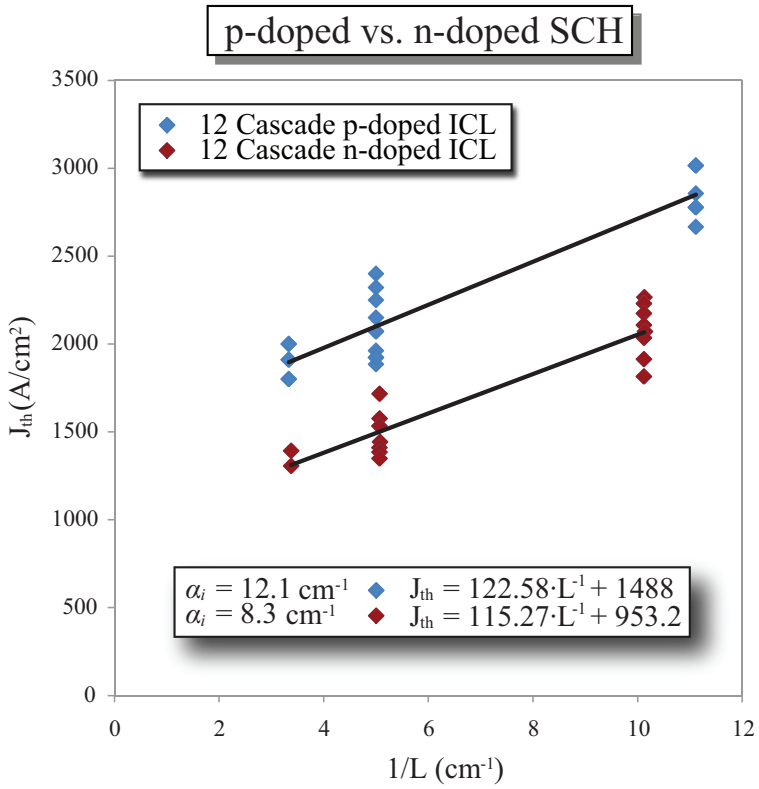

Figure 3.14: Improvement of the internal loss by using Te-doped (n) GaSb SCH.

implement. By plugging in all the numbers in the set of equations (3.4), we can obtain the expected L-I curve for the device operating CW. We can also project the maximum CW operating temperature, by finding the smallest value of T that keeps the expression for P_0 strictly non-positive. By doing this projection for our state of the art lasers, we estimated a 5 °C maximum CW temperature, which was close to the 3 °C of actual maximum CW temperature, but still below the target room temperature operation of 25 °C.

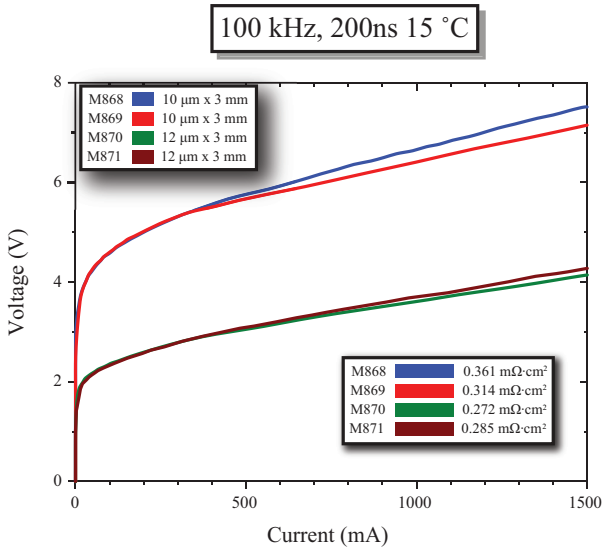

Figure 3.15: I-V characteristic for M868, M869, M870, M871.

3.5 Quantum well design optimization

In the last few sections we described, quantified and analyzed the first three out of six issues highlighted in section 3.3. In regard to the yield issue, it was overcome by gaining processing experience and optimization of the fabrication process. This significantly improved our device characterization reliability and consistency, which set the roadmap for optimal quantum well design leading to higher power and temperature laser devices. The last two parameters we are going to focus on are the internal loss a_i and the threshold current density J_{th}. As we discussed in the last chapter, equations (2.23) and (2.25) show how a_i, J_{th}, Γ, etc. are all related to each other. With the introduction of the SCH region we increased by more than double the Γ factor as shown in figure 3.6. What can we do to decrease a_i?

One of the most important improvements of the quantum well design was to n-dope the SCH region. We introduced the GaSb SCH region in order to increase the Γ confinement factor, however even undoped GaSb is intrinsically p-doped (1-$2{\cdot}10^{17}$ cm^{-3}). This p-type doping is responsible for higher optical absorption due to intervalence band absorption (IVBT)[88]. In order to compensate the doping type, we decided to dope the GaSb SCH layer with Te. High doping levels help reduce the resistance of the layer, however high levels of Te-doping might increase the free carrier absorption, which would also result in increasing a_i. So in our first attempt we decided to dope the SCH with $2.5{\cdot}10^{17}$ cm^{-3} of Te. We grew two ICL samples (M868, M869) featuring two (upper, lower) 2000Å thick layers of SCH and 12 cascades. The length dependence measurements of those two samples are illustrated in figure 3.14. M868 has an intrinsically doped SCH region, while M869 has the Te doped SCH region. Both samples have 12 cascades. By doing the same analysis as the one described in section 3.3, we were able to extract the internal loss a_i for both cases. We concluded that by introducing Te doping at the SCH region we were able to significantly reduce a_i from 12.1 cm^{-1} to 8.3 $cm^{-1}$and the threshold current density considerably for all lengths. Figure 3.15 also shows the current-voltage (I-V) characteristics of those devices. For M868 and M869 we see that there is an improvement in the differential resistance from 0.361 $m\Omega \cdot cm^2$ to 0.314 $m\Omega \cdot cm^2$. That could be attributed on the higher electrical conductivity of the n-doped GaSb SCH. This effect reduces the heat generated in the device while improving the device wall plug efficiency.

The device wall plug efficiency is defined as the output power ratio over the

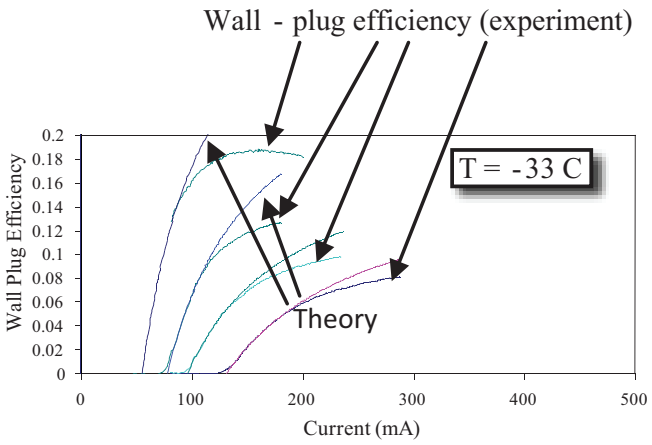

Figure 3.16: WPE of a 10 μm ridge laser (M868) at various device lengths (from left to right, 0.5 mm, 1 mm, 1.5 mm, 2 mm).

dissipated power $V \cdot I$.

$$\text{WPE} = \frac{P_0}{V \cdot I} \overset{eq.2.21}{=} \frac{h\upsilon}{qV}\eta_d \left(1 - \frac{I_{th}}{I}\right) \tag{3.5}$$

where WPE stand for wall plug efficiency.

We observe that our maximum pulsed WPE at 240 K was almost 20%. At 273 K we also observed a WPE of 10 % and 9 % for 280 K (not in figure). State of the art ICLs have demonstrated wall plug efficiencies of 27% at 80 K CW[89] and about 2.8% at 300 K[39]. By comparing the theoretical and the experimental curve of the WPE we can see that very soon, within 1.5 times the J_{th}, the curves start splitting. This is attributed to the poor thermal behavior of the ICLs. By extrapolation of the theoretical curve we can anticipate WPEs greater than 30% if pulsed with no heating effects. We also observe that the shortest devices exhibit the largest WPEs.

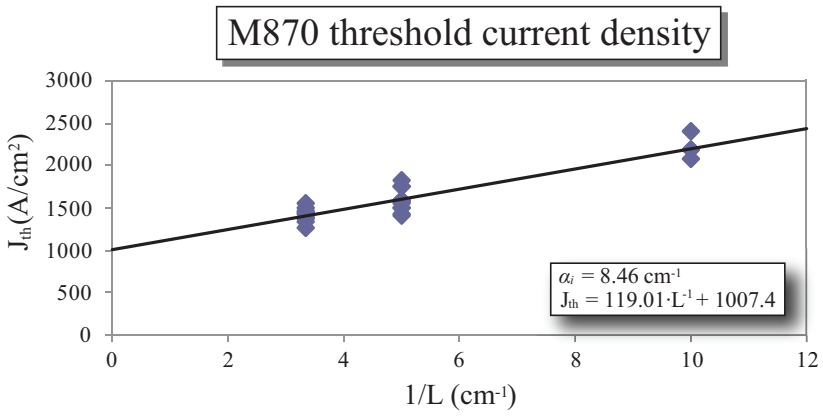

Figure 3.17: Threshold current density of M870.

However as shown in figure 3.14 the threshold current density is high and therefore heating is bigger of a concern here and that is manifested by the sharp roll-off of the 0.5 mm WPE curve.

The second design change we attempted was to reduce the number of cascades. The motivation behind this change lies in the attempt to reduce potentially increased IVBT in the p-doped regions of the active region. We were expecting that there should be a proportional effect on the a_i to the number of cascades. After growing the sample M870, and after doing the length dependence analysis shown in figure 3.17, the extracted value of a_i was 8.46 cm^{-1} which is very similar to the 8.3 cm^{-1} we obtained for the 12 cascade M869. This is the first indication that IVBT is not a dominant effect in the active region. The second indication comes from the M871 sample, which was grown exactly the same as M870 being different only in the amount of p-doping in the active region, which was half that of M870. The results are shown in figure 3.18. The extracted value of a_i for M871 was 8.3 cm^{-1} also very similar to M869. These results overrule our assumption of proportionality

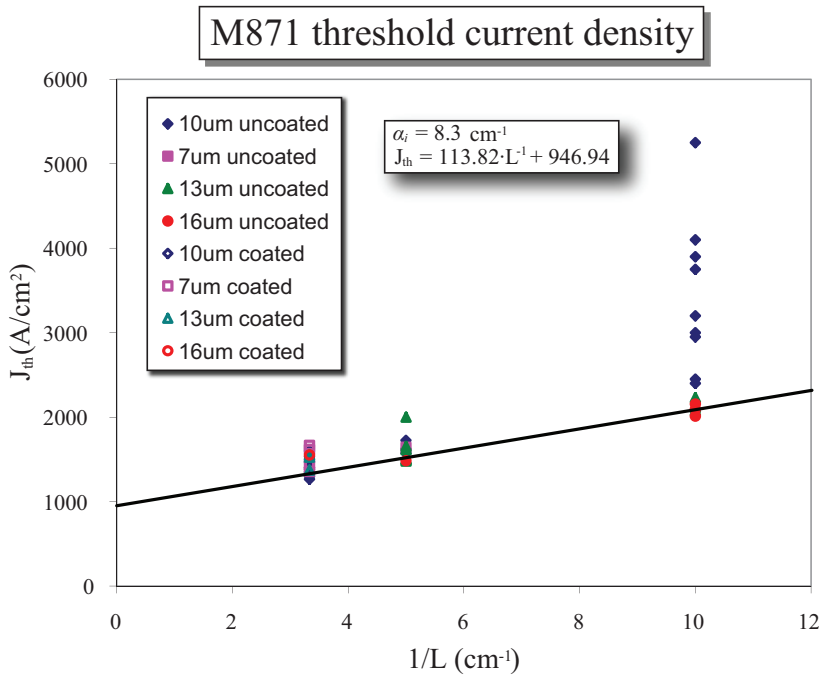

Figure 3.18: Threshold current density of M871.

of the internal loss to the number of cascades. Figure 3.15 also shows the V-I characteristic of M870 and M871. As expected the voltage is almost half the voltage of their 12 cascade counterpart and their differential resistance is almost the same, but smaller than the M869's due to a shorter active region.

One thing that stands out in figure 3.18 is the large spread of data especially in the 1 mm long devices. This plot made us realize the importance of the waveguide quality during fabrication as we discussed in section 3.3. Another thing we realized from the same plot is that for accurate fitting, it is better if we only accept the data around the lowest values of J_{th} and reject the rest. Fitting based on averaging all the data points just gives a larger error margin. Also the effect of the ridge width on the threshold current density seems to be small compared to the waveguide roughness spread, so it was neglected in our analysis.

Chapter 4

Anti reflection coating

4.1 Plane wave reflection

4.1.1 Fresnel equations

The Fresnel reflection of a plane wave incident on a smooth interface is a well studied problem. A plane wave incident on an interface, as shown in figure 4.1, with an incident angle of ϑ_0 and a refracted angle of ϑ_1, will have the following reflection coefficients determined by the boundary conditions of the parallel to the interface **E** and **H** components:

$$\begin{aligned} r_s &= \frac{n_0 \cos\vartheta_0 - n_1 \cos\vartheta_1}{n_0 \cos\vartheta_0 + n_1 \cos\vartheta_1} \qquad \text{(TE, s-polarization)} \\ r_p &= \frac{n_1 \cos\vartheta_0 - n_0 \cos\vartheta_1}{n_1 \cos\vartheta_0 + n_0 \cos\vartheta_1} \qquad \text{(TM, p-polarization)} \end{aligned} \tag{4.1}$$

We call plane of incidence the plane defined by the two propagation constant vectors $\vec{k_i}$ and $\vec{k_r}$. If the electric field is perpendicular to the plane of incidence then the

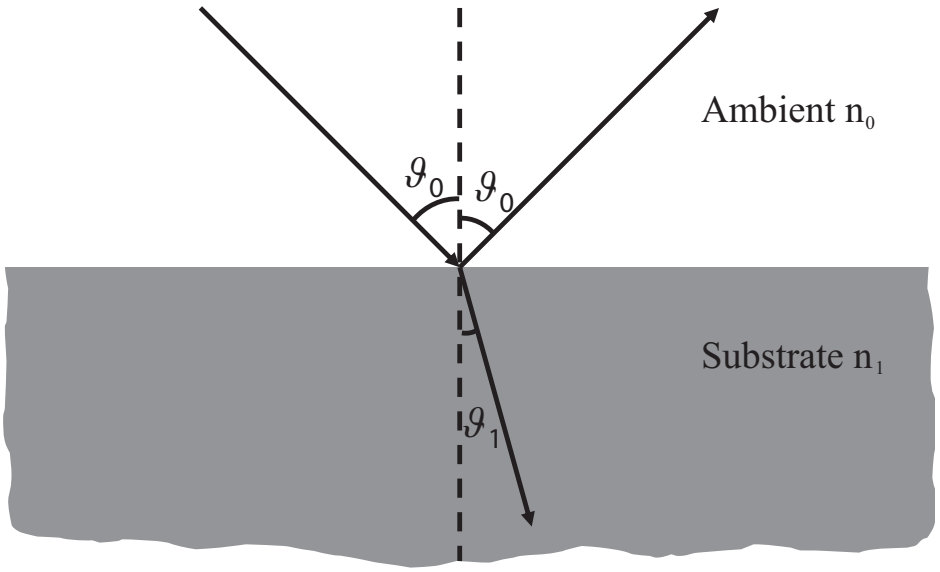

Figure 4.1: Fresnel reflection of an incident plane wave at the interface of two media

polarization is called TE (or s from the German *senkrecht* which means perpendicular). On the other hand if the electric field is parallel to the plane of incidence then the polarization is TM (or p polarization).

4.1.2 Snell's law

Snell's law is summarized in the following equation:

$$n_0 \sin \vartheta_0 = n_1 \sin \vartheta_1 \tag{4.2}$$

It can be very well derived by the Fermat's principle which states that light picks up the fastest path between two points. However that is a consequence of phase continuity along the boundary between the two materials. That statement is described

by the following equation:

$$k_i \sin \vartheta_0 = k_r \sin \vartheta_0 = k_t \sin \vartheta_1 \tag{4.3}$$

It states that the propagation constant component parallel to the interface has to be continuous. Snell's law as well as the law of reflection are direct consequences of that. In Eq.(4.3) k can be complex in the case of material absorption and ϑ can be imaginary in the case of evanescent fields.

4.1.3 Single layer reflectivity

As light penetrates through a multilayered material system, Eq.(4.1) is not enought to calculate the reflection coefficient at an interface. Since there are multiple internal reflections occuring at all interfaces that have to be accounted for. There are two ways to study the reflection of light in a multilayered material system. One is to consider a steady state of the incoming and outgoing electric field and study the boundary conditions at the interface, and the other is to study the progression of the electric field as it propagates through the material.

4.1.3.1 Steady state approach of single layer reflectivity

Let us assume that we have a single layer system as illustrated in figure 4.2. The incident electric field E_{0i} gets refracted to material 1 as E_{01} propagates down the film until it hits the second interface as E_{12}. Then part of it gets transmitted as E_t and part of it gets reflected as E_{21}. E_{21} becomes E_{10} by the time it reaches

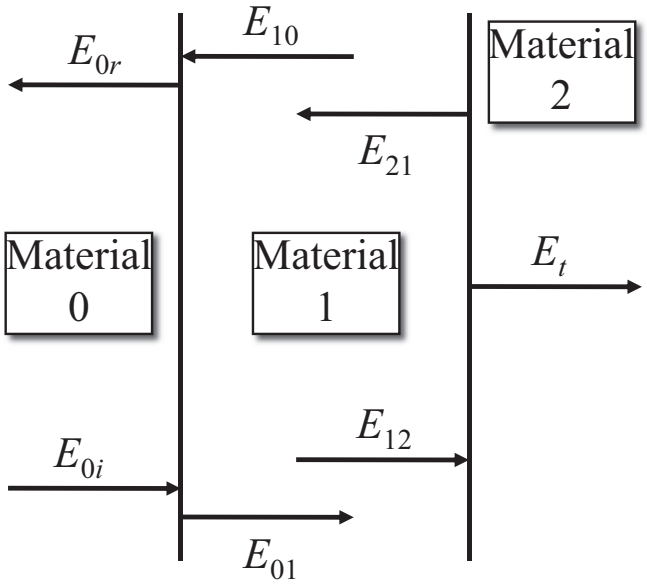

Figure 4.2: Steady state of the electric field in a single layer system

the first interface. Part of it gets through as E_{0r} and part of it gets reflected again as part of E_{01}, since E fields are on steady state. The study of the TE boundary conditions at the first interface, after consulting figure 4.5, yields the following set of equations:

$$\begin{aligned} E_{0r} + E_{0i} &= E_{10} + E_{01} = r_{12}e^{-i2\varphi}E_{01} + E_{01} \\ k_0E_{0r} - k_0E_{0i} &= k_1E_{10} - k_1E_{01} = k_1E_{01}(r_{12}e^{-i2\varphi} - 1) \end{aligned} \tag{4.4}$$

Apparently $E_{10} = r_{12}e^{-2i\varphi}E_{01}$ where $e^{-i\varphi}$ is due to the phase delay of the propagating wave through the film, therefore $\varphi = {}^{2\pi n_1 d_1 \cos\vartheta_1}/_{\lambda_0}$(where n_1 and d_1 are the index and thickness of material 1 and ϑ_1 is the angle of the plane wave in material 1 under oblique incidence. ϑ_1 is better illustrated in figure 4.3. As for r_{ab}, it is the reflection coefficient when light goes from material a to b. The k_i constants are the

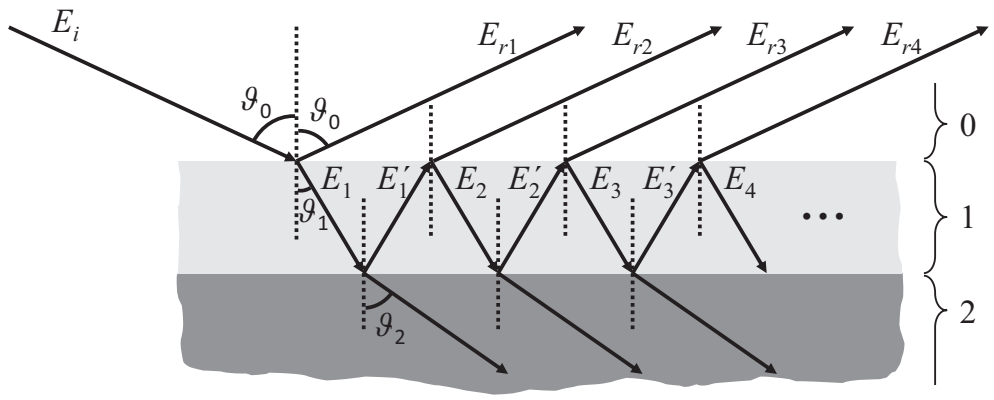

Figure 4.3: The electric field in a single layer system as it gets multiple reflections from the various interfaces

component of the propagation constant normal to the interface. By doing simple calculations and taking into account Eq.(4.1), and using $r_{ab} = -r_{ba}$ and $1 + r = t$, where t is the transmission coefficient, we end up with the following equation:

$$r_{s,p} = \frac{r_{01\,s,p} + r_{12\,s,p} e^{-i2\varphi}}{1 + r_{01\,s,p} r_{12\,s,p} e^{-i2\varphi}} \tag{4.5}$$

which works both for s and p polarization.

4.1.3.2 Series approach of single layer reflectivity and generalization to multilayered structures

Another way to calculate the film reflectivity would be to account each individual reflection occuring between the inner walls of the film. According to figure 4.3, if E_i is the incident electric field, then $E_1 = r_{01} E_i$. Also $E_1' = r_{12} e^{-i2\varphi} E_1$ and $E_{r1} = r_{01} E_i$, $E_{r2} = t_{10} E_1'$, $E_{r3} = t_{10} E_2'$, etc. For the total reflected field we have

$E_r = \sum_j E_{rj}$. For each reflection we have:

$$\begin{aligned} E_r &= r_{01}E_i + t_{10}(E'_1 + E'_2 + E'_3 + \cdots) \\ E'_1 &= r_{12}e^{-i2\varphi}E_1, \quad E'_2 = r_{12}e^{-i2\varphi}E_2, \ \cdots \\ E_2 &= r_{12}r_{10}e^{-i2\varphi}E_1, \quad E_3 = r_{12}r_{10}e^{-i2\varphi}E_2, \ \cdots \\ E_1 &= t_{01}E_i \end{aligned} \tag{4.6}$$

The above system gives a simple geometric series which when solved will give us equation (4.5).

Let us note that during this derivation nowhere was it assumed that material 2 is a bulk material. The r_{12} coefficient was just the reflection from the 1-2 interface and it could be as well the reflection coefficient of a complex multilayered system as illustrated in figure 4.4. Therefore if we call r_{1N} the reflection coefficient at the interface of material 1 and the rest of the structure we get the following generalized equation for the reflection coefficient:

$$r_{s,p} = \frac{r_{01\,s,p} + r_{1N\,s,p}e^{-i2\varphi}}{1 + r_{01\,s,p}r_{1N\,s,p}e^{-i2\varphi}} \tag{4.7}$$

This recursive equation allows us to calculate the reflection coefficient bottom up of complicated multilayered structures.

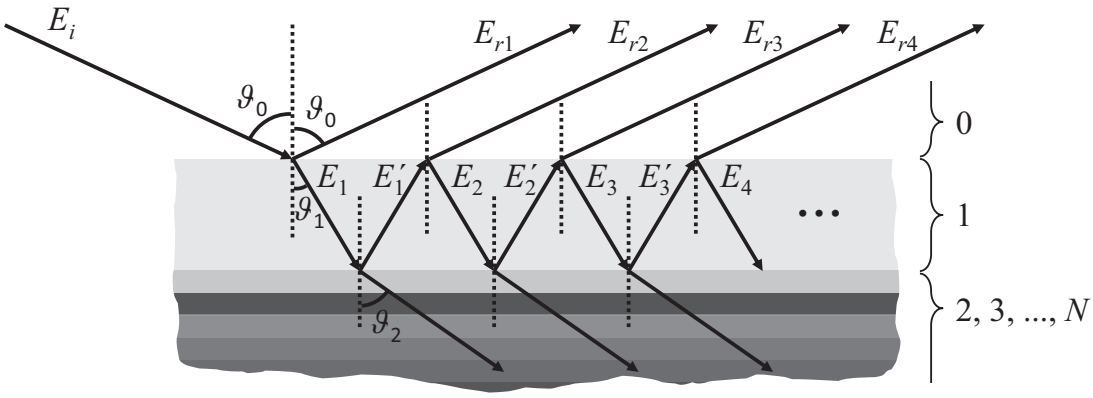

Figure 4.4: Reflected field from a multilayered structure

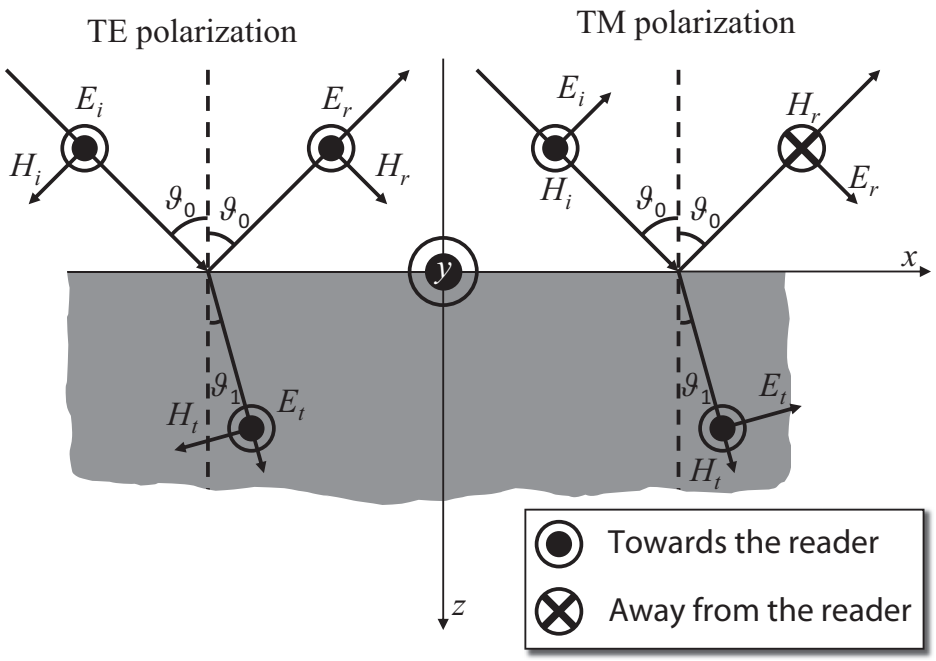

Figure 4.5: TE vs TM. (Typically the E field conventionally is assumed positive)

4.2 Reflection coefficient of a multilayer coating

Once we have decided on the laser and waveguide design the next step would be to design the AR coating. In this section we are going to describe the physics behind multiple layer coatings[90] by studying the transmission and reflection of each individual layer. Then we will focus on the results for single and double layer coatings.

4.2.1 Introduction of field matrix formulation

4.2.1.1 TE polarization

Consider the TE s-polarization case where the electric field is perpendicular to the plane of incidence. If E_i, E_r, E_t are the incident, reflected and transmitted electric field complex amplitudes[1] respectively, and $\vec{k_i}$, $\vec{k_r}$, $\vec{k_t}$ their propagation constants, then each component should be described by the following equations:

$$\begin{aligned} &E_i e^{-i\vec{k_i}\vec{r}+i\omega t} \\ &E_r e^{-i\vec{k_r}\vec{r}+i\omega t} \\ &E_t e^{-i\vec{k_t}\vec{r}+i\omega t} \end{aligned} \tag{4.8}$$

These equations are general even when there is a phase shift at the boundary. In that case all the phase information would be integrated in the constant up front. The reflection and transmission coefficients are given by:

[1] Amplitude A and phase φ of a complex number can be viewed as the magnitude and angle of a single complex number $\mathcal{A} = Ae^{i\varphi}$ which we call *complex amplitude*.

$$r = \frac{E_r}{E_i}$$
$$t = \frac{E_t}{E_i} \tag{4.9}$$

In the case of the reflected and the transmitted energy through the interface, which is given by the perpendicular component to the interface of the Poynting vector $\vec{E} \times \vec{H}$, we have a dependence on $\vec{k}$ which occurs due to the following equation describing the relation of the electric and magnetic field of a propagating plane electromagnetic wave:

$$H_{i,r,t} = \frac{k_{i,r,t}}{\mu\omega} E_{i,r,t} \tag{4.10}$$

where i, r, t stand for incident, reflected and transmitted field

Taking the transmittance as the ratio of the transmitted power to the incident power and the reflectance as the ratio of the reflected power to the incident power, we can write:

$$T = \frac{\mathrm{Re}(\vec{S_t}\hat{n})}{\mathrm{Re}(\vec{S_i}\hat{n})} = |t|^2 \frac{\mathrm{Re}(k_t)\cos(\phi_t)}{\mathrm{Re}(k_i)\cos(\phi_i)}$$
$$R = \frac{\mathrm{Re}(-\vec{S_r}\hat{n})}{\mathrm{Re}(\vec{S_i}\hat{n})} = |r|^2 \tag{4.11}$$

where $\hat{n}$ is the vector perpendicular to the interface

$\phi_{i,t}$ is the angle of incidence or transmission respectively

In order to obtain the T and R parameters, we need to determine r, t which will be obtained by calculating the electric fields from the boundary conditions. Assuming

we have a perfect dielectric, our boundary condition requires that all parallel components to the interface should be continuous, therefore $\vec{E}_{||}$ and $\vec{H}_{||}$ are continuous. According to figure 4.5, for transverse electric (TE) fields it is implied:

$$\begin{aligned} \vec{E}_{||} &= (E_+ + E_-)\hat{y} \\ \vec{H}_{||} &= \tfrac{1}{\omega\mu} k_z (E_- - E_+)\hat{x} \end{aligned} \tag{4.12}$$

where E_+, E_- are the incident and reflected electric fields

Note we substitute E_i and E_r with E_+ and E_- for generality since E_i and E_r refer only to the field at the first interface, while E_+ and E_- can refer to any interface of a multilayered structure. The linear system above can be represented as follows:

$$\begin{pmatrix} E_{||} \\ H_{||} \end{pmatrix} = Q_s \begin{pmatrix} E_+ \\ E_- \end{pmatrix} \tag{4.13}$$

$$\text{where} \quad Q_s = \begin{pmatrix} 1 & 1 \\ -\frac{k_z}{c\mu k_0} & \frac{k_z}{c\mu k_0} \end{pmatrix}$$

From the boundary conditions we get:

$$Q_{s0} \begin{pmatrix} E_i \\ E_r \end{pmatrix} = Q_{s1} \begin{pmatrix} E_t \\ 0 \end{pmatrix} \tag{4.14}$$

where E_+ is now E_i and E_- is now E_r

0 is the first medium (usually air)

1 is the second medium

Now eq.(4.14) can be written as:

$$\begin{pmatrix} E_i \\ E_r \end{pmatrix} = N \begin{pmatrix} E_t \\ 0 \end{pmatrix} \tag{4.15}$$

where $N = Q_{s0}^{-1} Q_{s1}$

From eq.(4.15) assuming $\mu = 1$ we obtain:

$$\begin{aligned} t_s &= \frac{E_t}{E_i} = \frac{1}{N_{11}} = \frac{2k_{z0}}{k_{z0}+k_{z1}} = \frac{2n_0 \cos\vartheta_0}{n_0 \cos\vartheta_0 + n_1 \cos\vartheta_1} \\ r_s &= \frac{E_r}{E_i} = \frac{N_{21}}{N_{11}} = \frac{k_{z0}-k_{z1}}{k_{z0}+k_{z1}} = \frac{n_0 \cos\vartheta_0 - n_1 \cos\vartheta_1}{n_0 \cos\vartheta_0 + n_1 \cos\vartheta_1} \end{aligned} \tag{4.16}$$

4.2.1.2 TM polarization

For the case of transverse magnetic p-polarization (TM) similarly according to figure (4.5) we would get:

$$\begin{aligned} \vec{H}_{||} &= (H_+ - H_-)\hat{y} \\ \vec{E}_{||} &= \frac{c^2\mu}{n^2\omega} k_z (H_- + H_+)\hat{x} \end{aligned} \tag{4.17}$$

where H_+, H_- are the incident and reflected auxiliary magnetic fields

The linear system (4.17) can be represented as follows:

$$\begin{pmatrix} E_{||} \\ H_{||} \end{pmatrix} = Q_p \begin{pmatrix} E_+ \\ H_- \end{pmatrix} \tag{4.18}$$

where $Q_p = \begin{pmatrix} \frac{c\mu k_Z}{n^2 k_0} & \frac{c\mu k_Z}{n^2 k_0} \\ 1 & -1 \end{pmatrix}$

From the boundary conditions we get:

$$Q_{p0} \begin{pmatrix} H_i \\ H_r \end{pmatrix} = Q_{p1} \begin{pmatrix} H_t \\ 0 \end{pmatrix} \tag{4.19}$$

where H_+ is now H_i and H_i is now H_r

0 is the first medium (usually air)

1 is the second medium

Now (4.19) can be written as:

$$\begin{pmatrix} H_i \\ H_r \end{pmatrix} = N' \begin{pmatrix} H_t \\ 0 \end{pmatrix} \tag{4.20}$$

where $N' = Q_{p0}^{-1} Q_{p1}$

From (4.20) assuming $\mu = 1$ we obtain:

$$\begin{aligned} t_p &= \frac{E_t}{E_i} = \frac{n_0 H_t}{n_1 H_i} = \frac{n_0}{n_1} \frac{1}{N'_{11}} = \frac{2n_0 n_1 k_{z0}}{n_1^2 k_{z0} + n_0^2 k_{z1}} = \frac{2n_0 \cos\vartheta_0}{n_1 \cos\vartheta_0 + n_0 \cos\vartheta_1} \\ r_p &= \frac{E_r}{E_i} = \frac{H_r}{H_i} = \frac{N'_{21}}{N'_{11}} = \frac{n_0^2 k_{z1} - n_1^2 k_{z0}}{n_1^2 k_{z0} + n_0^2 k_{z1}} = \frac{n_0 \cos\vartheta_1 - n_1 \cos\vartheta_0}{n_1 \cos\vartheta_0 + n_0 \cos\vartheta_1} \end{aligned} \tag{4.21}$$

Equations (4.16) and (4.21) are the Fresnel equations we discussed earlier in this

chapter. Notice the convenience of this matrix method. By using equations (4.13) and (4.18) we can express the incident and reflected field with its parallel to the interface components.

4.2.2 Matrix calculation for individual layers

4.2.2.1 TE polarization

Assuming now that we have multiple layer dielectric structure of layers $j = 1, 2, 3, \ldots$ then if we could find a matrix M_j such that:

$$\begin{pmatrix} E_{||}(0_j) \\ H_{||}(0_j) \end{pmatrix} = M_j \begin{pmatrix} E_{||}(d_j) \\ H_{||}(d_j) \end{pmatrix} \tag{4.22}$$

which relates the parallel field on one side of the layer to the other side (d_j = thickness of j^{th} film, 0_j = origin of the j^{th} film), then the left hand side of (4.22) for the $(j+1)^{th}$ film would be equal to the matrix at the right hand side of (4.22) for the j^{th} film:

$$\begin{pmatrix} E_{||}(0_{j+1}) \\ \overline{H_{||}(0_{j+1})} \end{pmatrix} = \begin{pmatrix} E_{||}(d_j) \\ \overline{H_{||}(d_j)} \end{pmatrix} \tag{4.23}$$

These two equations comprise an iterative sequence which can link us from the first layer to the last by just multiplying all M_j matrices. Then by using equation (4.13) or (4.18) we can go back from the parallel components of the field to the actual field components of $\vec{E}$ and $\vec{H}$. Now let us determine the actual value of the matrix M.

Assuming that inside each layer the wave propagates along both z directions, the parallel components of both E and H would take the following form:

$$\begin{aligned} E_{||}(x,z,t) &= \left[A\sin(k_z z) + B\cos(k_z z)\right] e^{-ik_x x + i\omega t} \\ H_{||}(x,z,t) &= \left[C\sin(k_z z) + D\cos(k_z z)\right] e^{-ik_x x + i\omega t} \end{aligned} \tag{4.24}$$

From Maxwell's equations we get:

$$\nabla \times \mathbf{E} = -\mu \frac{\partial}{\partial t}\mathbf{H} \Rightarrow -\mathbf{i}\frac{\partial E_{||}}{\partial z} + \mathbf{k}\frac{\partial E_{||}}{\partial x} = -i\mu\omega\mathbf{H} = -i\mu\omega(\mathbf{i}H_{||} + \mathbf{k}H_{\perp}) \tag{4.25}$$

By comparing the **i** components only, we get:

$$\frac{\partial E_{||}}{\partial z} = i\mu\omega H_{||} \tag{4.26}$$

Using the first part of (4.24) in (4.26) we get:

$$\left.\frac{\partial E_{||}}{\partial z}\right|_{z=0} = Ak_z = i\mu\omega H_{||}(0) \Rightarrow A = \frac{ic\mu k_0}{k_z} H_{||}(0) \tag{4.27}$$

By differentiating (4.26) and using the second part of (4.24) we get the expression for C:

$$\frac{\partial^2 E_{||}}{\partial z^2} = i\mu\omega\frac{\partial H_{||}}{\partial z} \Rightarrow -k_z^2 E_{||}(0) = i\mu\omega k_z C \Rightarrow C = \frac{ik_z}{c\mu k_0} E_{||}(0) \tag{4.28}$$

Quite obviously B and D are given from the following equations:

$$\begin{aligned} B &= E_{||}(0) \\ D &= H_{||}(0) \end{aligned} \tag{4.29}$$

Using the derived parameters in eqs.(4.34-4.36), equation 4.24 can be conveniently expresssed into the following matrix formulation:

$$\begin{pmatrix} E_{||}(z) \\ H_{||}(z) \end{pmatrix} = \begin{pmatrix} \cos(k_z z) & \frac{ic\mu k_0}{k_z}\sin(k_z z) \\ \frac{ik_z}{c\mu k_0}\sin(k_z z) & \cos(k_z z) \end{pmatrix} \begin{pmatrix} E_{||}(0) \\ H_{||}(0) \end{pmatrix} = M^{-1} \begin{pmatrix} E_{||}(0) \\ H_{||}(0) \end{pmatrix} \tag{4.30}$$

Equation (4.30) is almost in the form (4.22). By simply inverting the previous matrix we derive the M matrix for TE polarization:

$$M = \begin{pmatrix} \cos(k_z z) & -\frac{ic\mu k_0}{k_z}\sin(k_z z) \\ -\frac{ik_z}{c\mu k_0}\sin(k_z z) & \cos(k_z z) \end{pmatrix} \tag{4.31}$$

4.2.2.2 TM polarization

Similarly for TM polarization we have:

$$\nabla \times \mathbf{H} = -\varepsilon \frac{\partial}{\partial t}\mathbf{E} \Rightarrow -\mathbf{i}\frac{\partial H_{||}}{\partial z} + \mathbf{k}\frac{\partial H_{||}}{\partial x} = i\varepsilon\omega\mathbf{E} = -i\varepsilon\omega(\mathbf{i}E_{||} + \mathbf{k}E_{\perp}) \tag{4.32}$$

By comparing the **i** components only we get:

$$-\frac{\partial H_{||}}{\partial z} = i\varepsilon\omega E_{||} \tag{4.33}$$

Using the first part of (4.24) in (4.33) we get:

$$\left.\frac{\partial H_{||}}{\partial z}\right|_{z=0} = Ck_z = -i\varepsilon\omega E_{||}(0) \Rightarrow C = \frac{in^2k_0}{c\mu k_z}E_{||}(0) \tag{4.34}$$

By differentiating (4.33) and using the second part of (4.24) we get the exprerssion for C:

$$\frac{\partial^2 H_{||}}{\partial z^2} = i\varepsilon\omega\frac{\partial E_{||}}{\partial z} \Rightarrow k_z^2 H_{||}(0) = i\varepsilon\omega k_z A \Rightarrow A = -\frac{ic\mu k_z}{n^2k_0}H_{||}(0) \tag{4.35}$$

Quite obviously B and D are given from the following equations:

$$\begin{aligned} B &= E_{||}(0) \\ D &= H_{||}(0) \end{aligned} \tag{4.36}$$

Using the derived parameters in equations (4.34-4.36), equation (4.24) can be conveniently expressed into the following matrix formulation:

$$\begin{pmatrix} E_{||}(z) \\ H_{||}(z) \end{pmatrix} = \begin{pmatrix} \cos(k_z z) & -\frac{ic\mu k_z}{n^2 k_0}\sin(k_z z) \\ -\frac{in^2 k_0}{c\mu k_z}\sin(k_z z) & \cos(k_z z) \end{pmatrix} \begin{pmatrix} E_{||}(0) \\ H_{||}(0) \end{pmatrix} = M^{-1} \begin{pmatrix} E_{||}(0) \\ H_{||}(0) \end{pmatrix} \tag{4.37}$$

Equation (4.37) is almost in the form (4.22). By simply inverting the previous matrix we derive the M matrix for TM polarization:

$$M = \begin{pmatrix} \cos(k_z z) & \frac{ic\mu k_z}{n^2 k_0}\sin(k_z z) \\ \frac{in^2 k_0}{c\mu k_z}\sin(k_z z) & \cos(k_z z) \end{pmatrix} \tag{4.38}$$

4.2.3 Synthesizing the complete reflection matrix of a multilayered system

Having calculated M_j for a multilayer system and Q matrices, we can link the incident and reflected fields E_i, E_r (TE) or H_i, H_r (TM) to the transmitted ones E_t or H_t. In the TE case for example we have:

$$\begin{pmatrix} E_t \\ 0 \end{pmatrix} = Q_s^{-1} M_j^{-1} M_{j-1}^{-1} M_{j-2}^{-1} \cdots M_2^{-1} M_1^{-1} Q_a \begin{pmatrix} E_i \\ E_r \end{pmatrix} \tag{4.39}$$

or

$$\begin{pmatrix} E_i \\ E_r \end{pmatrix} = Q_a^{-1} M_1 M_2 \cdots M_{j-2} M_{j-1} M_j Q_s \begin{pmatrix} E_t \\ 0 \end{pmatrix} = N \begin{pmatrix} E_t \\ 0 \end{pmatrix} \tag{4.40}$$

where a stands for ambient

s stands for substrate

j is the total number of layers

Note that we can simply multiply each matrix M_j in order to obtain the fields since at each boundary the perpendicular components are equal. By defining matrix N as follows:

$$N = Q_a^{-1} M Q_s = \begin{pmatrix} N_{11} & N_{12} \\ N_{21} & N_{22} \end{pmatrix} \tag{4.41}$$

where $M = \prod_{i=1}^{j} M_i$

we can calculate the reflection and transmission coefficients given by (4.9) using the following equations:

$$\begin{aligned} t_s &= \frac{1}{N_{11}} = \frac{2k_{za}}{k_{za}M_{11}+k_{zs}M_{22}-\frac{k_{za}k_{zs}}{c\mu k_0}M_{12}-c\mu k_0 M_{21}} \\ r_s &= \frac{N_{21}}{N_{11}} = \frac{k_{za}M_{11}-k_{zs}M_{22}-\frac{k_{za}k_{zs}}{c\mu k_0}M_{12}+c\mu k_0 M_{21}}{k_{za}M_{11}+k_{zs}M_{22}-\frac{k_{za}k_{zs}}{c\mu k_0}M_{12}-c\mu k_0 M_{21}} \end{aligned} \quad \text{(TE)}$$

$$\begin{aligned} t_p &= \frac{n_a}{n_s}\frac{1}{N_{11}} = \frac{2n_a n_s k_{za}}{n_a^2 k_{zs}M_{11}+n_s^2 k_{za}M_{22}+\frac{n_a^2 n_s^2 k_0}{c\mu}M_{12}+\frac{c\mu k_{za}k_{zs}}{k_0}M_{21}} \\ r_p &= \frac{N_{21}}{N_{11}} = \frac{n_a^2 k_{zs}M_{11}-n_s^2 k_{za}M_{22}+\frac{n_a^2 n_s^2 k_0}{c\mu}M_{12}-\frac{c\mu k_{za}k_{zs}}{k_0}M_{21}}{n_a^2 k_{zs}M_{11}+n_s^2 k_{za}M_{22}+\frac{n_a^2 n_s^2 k_0}{c\mu}M_{12}+\frac{c\mu k_{za}k_{zs}}{k_0}M_{21}} \end{aligned} \quad \text{(TM)}$$

(4.42)

We notice that all resulting equations have a k_z over nk_0 ratio which equals $\cos(\gamma)$ where γ is the angle of $\mathbf{k}$ with respect to the perpendicular to the interface. By substituting $q_j = -n_j \cos(\gamma_j)/(c\mu)$ for TE and $q_j = n_j/[\cos(\gamma_j) \cdot (c\mu)]$ for TM we

TE	TM
$q_j = -\frac{1}{c\mu_j} n_j \cos(\gamma_j)$	$q_j = \frac{1}{c\mu_j} \frac{n_j}{\cos(\gamma_j)}$
$Q_s = \begin{pmatrix} 1 & 1 \\ q_j & -q_j \end{pmatrix}$	$Q_p = \begin{pmatrix} 1/q_j & 1/q_j \\ 1 & -1 \end{pmatrix}$
$M_j = \begin{pmatrix} \cos(\varphi_j) & (i/q_j)\sin(\varphi_j) \\ iq_j \sin(\varphi_j) & \cos(\varphi_j) \end{pmatrix}$	

Table 4.1: All Q and M matrices using the q normalization factors for both TE and TM polarizations

get the following equation for the M_j for both TE and TM cases:

$$M_j = \begin{pmatrix} \cos(\varphi_j) & \frac{i}{q_j}\sin(\varphi_j) \\ iq_j \sin(\varphi_j) & \cos(\varphi_j) \end{pmatrix} \tag{4.43}$$

where $\varphi_j = k_z d_j$ and d_j is the thickness of the j^{th} layer

Table 4.1 summarizes all Q and M matrices using the q normalization factor. A Matlab program calculating the rerflection and the transmission coefficient of a multilayered coating is presented in appendix A.

4.2.4 Notable cases for dielectric coatings

We will now study the two most important cases which we will mostly deal with when we design our laser coatings. Single layer coatings which provide an easy solution for coatings in applications that do not have stringent performance require-

ments in terms of reflectivity and bandwidth tailoring, and double layer coatings that give us enough degrees of freedom to achieve aforementioned performance with more flexibility in material selection.

4.2.4.1 Single layer coating

First we will discuss single layer coatings. Using the normalized parameters for TE polarization, we obtain for the reflectivity:

$$r = \frac{q_a M_{11} - q_s M_{22} + q_a q_s M_{12} - M_{21}}{q_a M_{11} + q_s M_{22} + q_a q_s M_{12} + M_{12}} = \frac{(q_a - q_s)\cos(\varphi_1) + i\left(\frac{q_a q_s}{q_1} - q_1\right)\sin(\varphi_1)}{(q_a + q_s)\cos(\varphi_1) + i\left(\frac{q_a q_s}{q_1} + q_1\right)\sin(\varphi_1)} \tag{4.44}$$

where $j = 1$ since we have a single layer

Equation (4.44) indicates, that a small reflectivity can be achieved if $\cos(\varphi_1) = 0$ and $q_a q_s/q_1 - q_1$ is as small as possible. Therefore by adjusting the index and the thickness of the film we can control the values of φ_1 and q_1 in order to obtain the desired reflectivity. Notice that when we are at normal incidence, $q_j = -n_j \cos(\gamma_j)/(c\mu_j)$, so the minimum reflectivity condition becomes:

$$\frac{n_a n_s}{n_1} - n_1 = 0 \Rightarrow n_1 = \sqrt{n_a n_s} \tag{4.45}$$

So the two conclusions for a single layer AR coating are that for optimum performance, the index of the deposited layer must be the square root of the product of the surrounding indices and the thickness of the layer should be a quarter wavelength

thick so that $\cos(\varphi_1) = 0$ (by quarter wavelength thick we refer to the z component of the wavevector).

4.2.4.2 Double layer coating

For the case of a double layer coating, in the TE case, we calculate each matrix component Q_a, Q_s, M_1, M_2 and derive r which is given in this case by the following equation:

$$r = \frac{(q_a q_1 q_2 - q_s q_1 q_2)\cos(\varphi_1)\cos(\varphi_2) - (q_a q_2^2 - q_s q_1^2)\sin(\varphi_1)\sin(\varphi_2) + \cdots}{(q_a q_1 q_2 + q_s q_1 q_2)\cos(\varphi_1)\cos(\varphi_2) - (q_a q_2^2 + q_s q_1^2)\sin(\varphi_1)\sin(\varphi_2) + \cdots}$$

$$\frac{\cdots + i[(q_a q_s q_1 - q_1 q_2^2)\cos(\varphi_1)\sin(\varphi_2) + (q_a q_s q_2 - q_1^2 q_2)\sin(\varphi_1)\cos(\varphi_2)]}{\cdots + i[(q_a q_s q_1 + q_1 q_2^2)\cos(\varphi_1)\sin(\varphi_2) + (q_a q_s q_2 + q_1^2 q_2)\sin(\varphi_1)\cos(\varphi_2)]} \tag{4.46}$$

This nice equation becomes zero when both the real and imaginary values of the numerator become zero. Therefore for a double layer coating we have:

$$\left.\begin{aligned}(q_a q_1 q_2 - q_s q_1 q_2)\cos(\varphi_1)\cos(\varphi_2) - (q_a q_2^2 - q_s q_1^2)\sin(\varphi_1)\sin(\varphi_2) = 0 \\ (q_a q_s q_1 - q_1 q_2^2)\cos(\varphi_1)\sin(\varphi_2) + (q_a q_s q_2 - q_1^2 q_2)\sin(\varphi_1)\cos(\varphi_2) = 0\end{aligned}\right\}$$

$$\left.\begin{aligned}(q_a q_1 q_2 - q_s q_1 q_2) - (q_a q_2^2 - q_s q_1^2)\tan(\varphi_1)\tan(\varphi_2) = 0 \\ (q_a q_s q_1 - q_1 q_2^2)\tan(\varphi_2) + (q_a q_s q_2 - q_1^2 q_2)\tan(\varphi_1) = 0\end{aligned}\right\} \tag{4.47}$$

For normal incidence and for an ambient index of one we get:

$$\left.\begin{aligned}(n_1n_2 - n_sn_1n_2) - (n_2^2 - n_sn_1^2)\tan(\varphi_1)\tan(\varphi_2) = 0\\ (n_sn_1 - n_1n_2^2)\tan(\varphi_2) + (n_sn_2 - n_1^2n_2)\tan(\varphi_1) = 0\end{aligned}\right\}$$

$$\left.\begin{aligned}\tan^2(\varphi_1) = \tfrac{(n_s-1)(n_2^2-n_s)n_1^2}{(n_1^2n_s-n_2^2)(n_s-n_1^2)}\\ \tan^2(\varphi_2) = \tfrac{(n_s-1)(n_s-n_1^2)n_2^2}{(n_1^2n_s-n_2^2)(n_2^2-n_s)}\end{aligned}\right\} \tag{4.48}$$

In this case, given the ambient environment and the substrate, the parameters we control are φ_1, φ_2, n_1, n_2, 1 for the outer layer and 2 for the inner layer. We have much more flexibility in terms of materials compared to the single layer case. For example in order to achieve zero reflectance in the single layer case, we need to have an exact coating index determined by (4.45) which is not always possible. However in the double layer coatings, and for given set of coating materials, what will ultimately determine the reflectivity is the thickness of each material. As long as our φ_1 and φ_2 satisfy (4.48) the reflectivity is going to be zero. By having a quick look at (4.48) we notice that in order to have a real solution for the indices, the terms $(n_s - n_1^2)$, $(n_1^2n_s - n_2^2)$ and $(n_2^2 - n_s)$ should either be all positive, or only one of those terms should be positive in order for the right side of (4.48) to be positive as shown in table 4.2. Each case in table 4.2 is shown in figure 4.6, except case $(+--)$ which is never possible. Figure 4.6 gives a very good guide on material selection for zero reflectivity double layer coatings[91] as long as we have lax bandwidth specifications. In case you are having hard time believing this, the inset of figure 4.6 shows a colormap of the simulated minimum reflectivity of coatings at various indices.

Zero reflectivity regimes

(+ + +)	$n_s \geq n_1^2$	$n_1^2 n_s \geq n_2^2$	$n_s \leq n_2^2$
(- + -)	$n_s \leq n_1^2$	$n_1^2 n_s \geq n_2^2$	$n_s \geq n_2^2$
(- - +)	$n_s \leq n_1^2$	$n_1^2 n_s \leq n_2^2$	$n_s \leq n_2^2$
(+ - -)	$n_s \geq n_1^2$	$n_1^2 n_s \leq n_2^2$	$n_s \geq n_2^2$

Table 4.2: Indices that provide zero reflectivity double layer coatings (Assuming $n_0 = 1$)

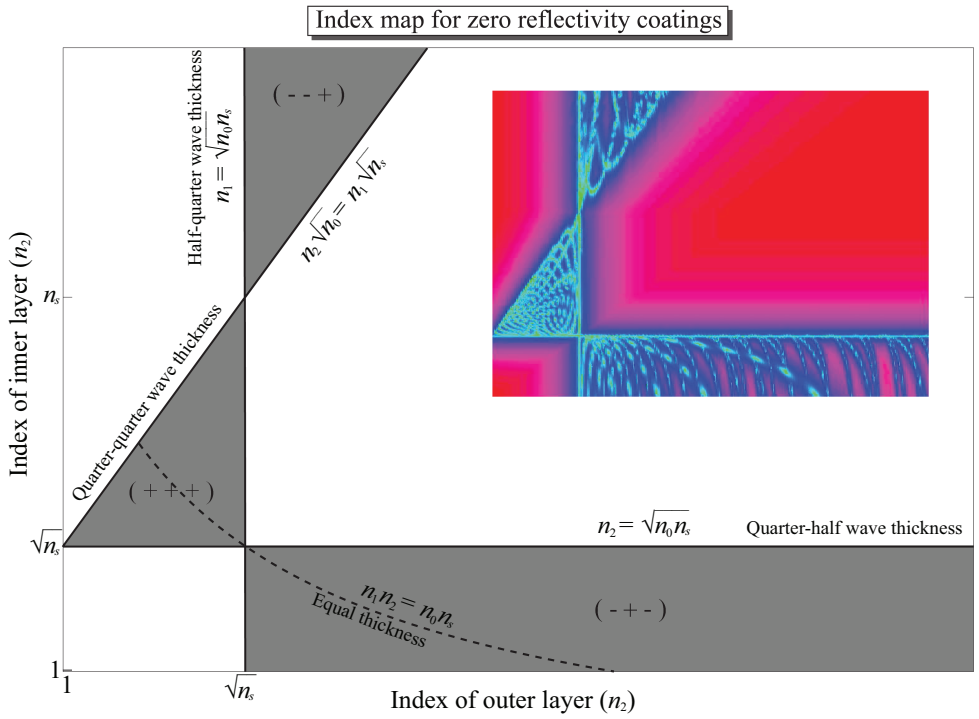

Figure 4.6: Index map for zero reflectivity double layer coatings (Assuming $n_0 = 1$)

4.2.4.3 Important double layer coating regimes

There are four important cases resulting from equation (4.48):

- $\tan^2(\varphi_1) = \tan^2(\varphi_2)$
- $\varphi_1 = \varphi_2 = (2m-1)\frac{\pi}{2}, \qquad m = 1,\, 2,\, 3,\, \ldots$
- $\tan^2(\varphi_1) = 0$
- $\tan^2(\varphi_2) = 0$

The first two cases are the most important. The first one corresponds to coatings of equal optical thickness. The second condition corresponds to the case of double quarter wave coating, which is the limit of the first case at infinity. The third and fourth case refer correspondingly to the half-quarter and quarter-half wave case. The last two cases are somewhat degenerate cases to single layer coating. Therefore our main focus lies on the first two cases. Analyzing equation (4.48), taking into account $n_0 \neq 1$, we get the following corrersponding index conditions:

- $n_1 n_2 = n_0 n_s$ (Equal optical thickness) $(n_1 d_1 = n_2 d_2)$
- $n_1^2 n_s = n_2^2 n_0$ (Double quarter wave thickness) $(n_1 d_1 = n_2 d_2 = \lambda_0/4)$
- $n_2^2 = n_0 n_s$ (Half-quarter wave thickness) $(n_1 d_1 = \lambda_0/2 \; ; \; n_2 d_2 = \lambda_0/4)$
- $n_1^2 = n_0 n_s$ (Quarter-half wave thickness) $(n_1 d_1 = \lambda_0/4 \; ; \; n_2 d_2 = \lambda_0/2)$

Those extreme cases are shown plotted in figure 4.6, which define the boundaries of the zero reflectivity regions.

Figure 4.7 (top)		Figure 4.7 (bottom)		Figure 4.8 (top)		Figure 4.8 (bottom)	
n_1	n_2	n_1	n_2	n_1	n_2	n_1	n_2
1	2	1.414	2.829	1.414	2.829	1.414	2.128
1.25	2.5	1.6	3.2	1.6	2.5	1.6	2.5
1.414	2.829	2	4	2	2	1.7645	2.829
		3	6	3	3/4		
				4	1		

Table 4.3: Summary of indices used in figure (4.7) and (4.8).

4.2.4.4 Bandwidth tailoring of double layered coatings

Apparently there are many materials that satisfy those requirements. The plot in figure (4.6) shows the indices that would produce zero reflectivity coatings. This however does not give us any information on the coating bandwidth. Figures (4.7) and (4.8) show how the coating's spectrum changes as the inner and outer layer's indices are changed. Figure (4.7), shows the reflectivity spectrum change for quarter-quarter wave thick layers. The arrows' direction in the figure shows the corresponding order of the plotted spectra. Each dot in the index map (inset) refers to the corresponding plot at the main part of the figure. In figure (4.8) the plots show the reflectivity spectrum change for equal optical thickness coatings (top plot), and for a more general case of a coating that do not satisfy any of the major cases on page 94. The indices used for the simulations are summarized in table 4.3.

The first important conclusion we make is that quarter-quarter wave coatings support broader low rerflectivity spectra when the material indices are close to the condition for equal optical thickness. The second important conclusion is that along the "equal optical thickness"[2] index line, starting from the quarter-quarter

[2]The line that follows $n_1 n_2 = n_0 n_s$

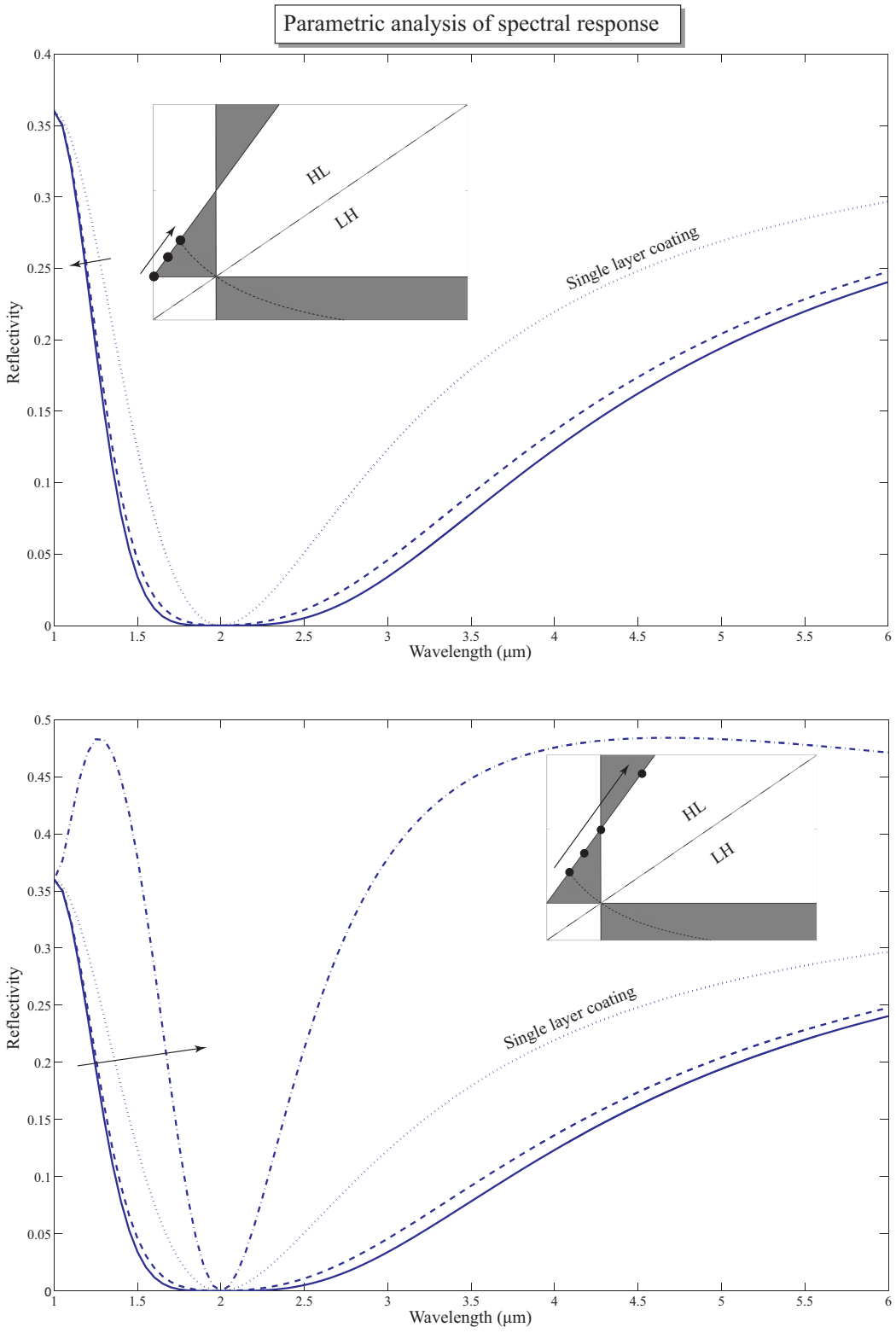

Figure 4.7: Parametric analysis of spectral response for quarter-quarter wave coatings.

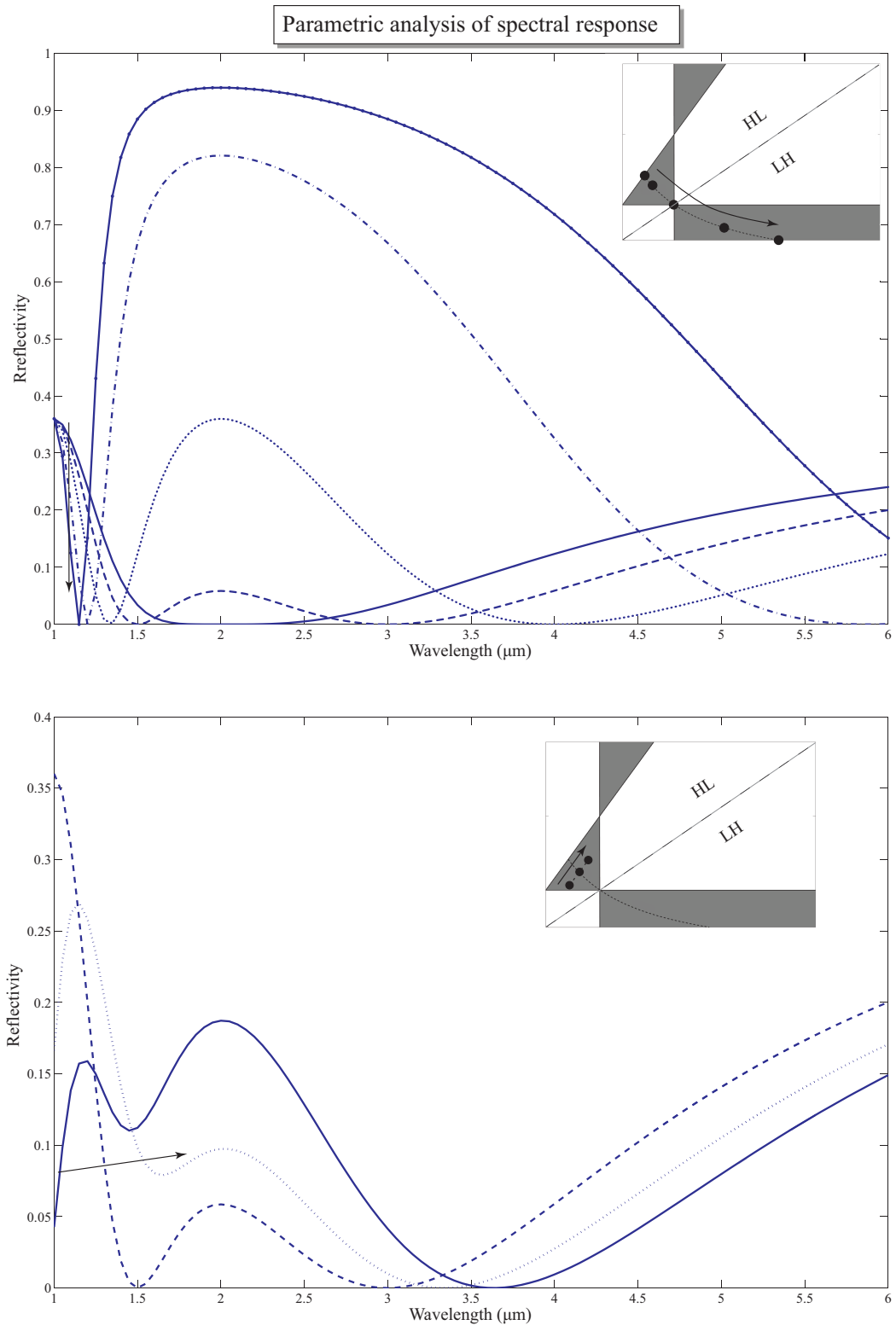

Figure 4.8: Parametric analysis of spectral response for equal optical thickness (up), and for general cases that don't satisfy any of the conditions in page 94 (down).

case, the spectrum starts to separate the single double-zero point into two discrete zeros. That is why double layer coatings are also called W coatings due to their shape. Single layer coatings which are shown as the degenerate cases, are plotted with dotted lines in figure (4.7) an are consequently called V-coatings. W coatings allow more flexibility in designing broad coatings. From figure (4.8) it is also obvious that having a broadband coating rersults into having a higher average rerflectivity in our range of interest. The average reflectivity is quantified by a factor called the merit function which we will discuss in the next section. Diverging from the "equal optical thickness line" we maintain bandwidth but we are starting to lose in reflectivity. More specifically we are losing the double zero characteristic, nevertheless still maintaining a zero reflectivity coating. In conclusion for a broad double layer coating we should be targeting materials that are in the range of the intersection of the "quarter-quarter"[3] line with the "equal optical thickness line". The point of intersection is described by the following equations:

$$\left.\begin{aligned} n_1 n_2 &= n_0 n_s \\ n_2\sqrt{n_0} &= n_1\sqrt{n_s} \end{aligned}\right\} \quad \begin{aligned} n_1 &= n_0^{3/4} n_s^{1/4} \\ n_2 &= n_0^{1/4} n_s^{3/4} \end{aligned} \tag{4.49}$$

Comparing figure (4.6) with figures (4.7) and (4.8), we see that it is typically more effective to use HL[4] (high-low) coatings since it provides lower average reflectivity coatings on the range of interest.

Some popular dielectrics for optical coating are included in table 4.4. We need

[3]The line that follows $n_2\sqrt{n_0} = n_1\sqrt{n_s}$

[4]refers to the comparative index of the inner and outer layer. In this case high inner index and low outer index.

Material	Index@1.3μm	Index@3.4μm
Al_2O_3	1.74	1.69
BaF_2	1.47	1.46
CaF_2	1.43	1.42
CeO_2	1.72	1.69
Ge	4.35	4.00
MgF_2	1.37	1.36
Si	3.54	3.42
SiO	1.88	1.81
SiO_2	1.53	1.48
Ta_2O_5	1.98	1.97
TiO_2	2.20	
Y_2O_3	1.85	1.70
ZnS	2.28	2.25
ZnSe	2.47	2.44
ZrO_2	2.12	2.07

Table 4.4: Evaporation material refractive indices.

to keep in mind that the actual index of the evaporated material depends heavily on the deposition method and conditions and might vary from the tabulated values. Table 4.4 provides a good guide for material selection, but when it comes down to designing a high quality coating we need to know precisely, to about at least two decimal points, the index of the material that we are going to use. Therefore pre-evaporation of index calibration samples is strongly recommended.

Let us consider as an example the case where we grow a MgF_2 and a Ta_2O_5 double layer on glass in the near IR wavelength. Then for the e-beam grown films the corresponding indices would be 1.37, 1.98 and 1.53. No matter which material is grown first, with indices n_1 or n_2, the terms $(n_s - n_1^2)$ and $(n_2^2 - n_s)$ always have opposite signs. Therefore for a good AR coating the term $(n_1^2 n_s - n_2^2)$ must be negative, which means that n_2 has to be 1.96 hence Ta_2O_5 must be grown first. This will take us in the $(--+)$ regime of figure 4.6 and is not necessarily the best choice, but in the case of a glass substrate it would be hard to find a material with

an index smaller than $\sqrt{1.53}$ in order to stay in the $(+++)$ regime, as we have discussed on page 92.

4.2.5 Criterion for broad bandwidth reflectivity coatings

The reflectivity of a facet as we defined it, is valid only at one wavelength. In the case of lasers, LED's and other light emitting devices with broad spectrum we want to use a measure of the coating reflectivity that accounts for the desired reflectivity spectrum. We therefore introduce a merit function as follows:

$$F(X) = \int_{\lambda_{start}}^{\lambda_{end}} [R(X,\lambda) - R_{target}(\lambda)]^2 d\lambda \tag{4.50}$$

where X is the collection of coating variables like the thicknesses and the refractive indices of all different coating layers.

λ is the wavelength, $\lambda_{start}, \lambda_{end}$ define the wavelength range of interest

R is the coating reflectivity

R_{target} is the desired coating reflectivity

Given that our goal is to produce an anti reflection (AR) coating we can assume that $R_{target}(\lambda) = 0$ in the wavelength range of interest λ_{start} to λ_{end}. Therefore:

$$F(X) = \int_{\lambda_{start}}^{\lambda_{end}} R^2(X,\lambda) d\lambda \tag{4.51}$$

The second purpose of the merit function F, is to use it as a criterion for coating design. An analytic approach exists for single and double layer coatings, but

in case of multilayer coatings, we have to resort to numerical means for designing a coating. A good AR coating would give a minimum merit function F by varying the X parameters. For example figure 4.9 shows the contour plot of the merit function of a GaSb interband cascade laser (ICL) coating centered at 3.4 μm with 100 nm bandwidth, an effective index of 3.457 and a mode size of 1.95 μm. As we will see in the following section, the mode size has to be taken into account and can significantly affect the coating design. As we can see from figure 4.9, in order to get a low reflectivity coating with $R \leq 10^{-4}$, we need to grow a very precise film with $\leq 10\, nm$ tolerance for the ZnS inner layer thickness and $\leq 20\, nm$ tolerance for the outer SiO_2 layer thickness and for that we need to use an *in-situ* monitoring technique for estimating the film thickness.

4.2.6 Plane wave decomposition analysis

In all of our study to this point it was implied that the incident wave on the multilayered interface was a plane wave. How far is that from reality? For many coating applications that assumption is sufficient, however when we deal with semiconductor lasers, semiconductor optical amplifiers (SOAs) and other components that produce a tight beam, diffraction is a major issue that has to be accounted for. The beam produced in such semiconductor devices, has a typical size of order λ (output wavelength). According to Gaussian optics such a beam will diverge according to the following equation:

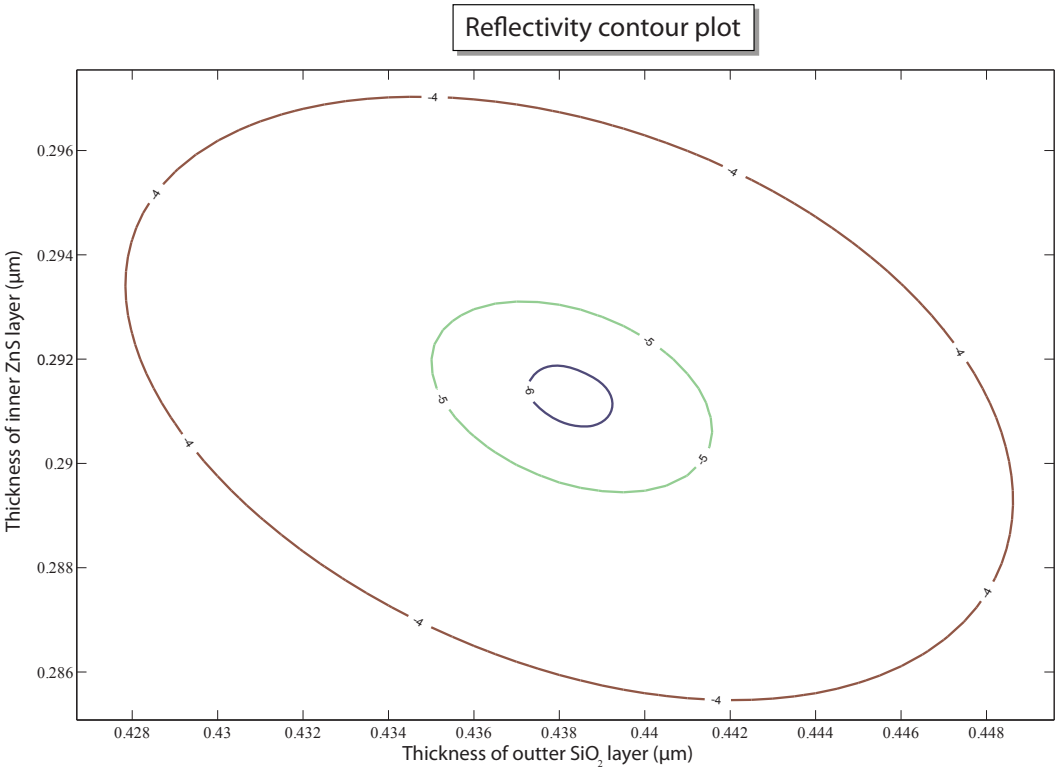

Figure 4.9: Contour plot of the merit function for a GaSb interband cascade laser coating

$$\vartheta_0 = \frac{2}{\pi}\frac{\lambda}{2W_0} \tag{4.52}$$

where $2W_0$ is the spot size of the beam at the interface

λ is the wavelength

ϑ_0 is the divergence cone half-angle

Let us consider the structure depicted in figure 4.10. This is a typical structure for an interband cascade laser. In red we have the index profile perpendicular to the epi-plane. On either side of our active region we have the lower cladding region on the left and the upper cladding region on the right. The two high index regions are the upper and lower separate confinement regions (SCH), while at the center we have the active region. The active region has a $\delta n = 0.05$ with respect to the cladding region. This would lead to a weakly confined mode, which is a problem for the following two reasons:

- The mode cannot extend below the lower cladding layer because the high index ($n = 3.8$) of the GaSb substrate (not depicted) would attract the mode and couple part of the power to leaky substrate modes.

- A weakly confined mode would result in higher loss at the metal contact due to the contact's high electrical conductivity.

A tightly confined mode instead is desirable that would give a large confinement factor Γ which is important for better device performance as we saw earlier. The depicted mode, according to equation (4.52), will have a spread of $\vartheta_0 = 47°$ in free

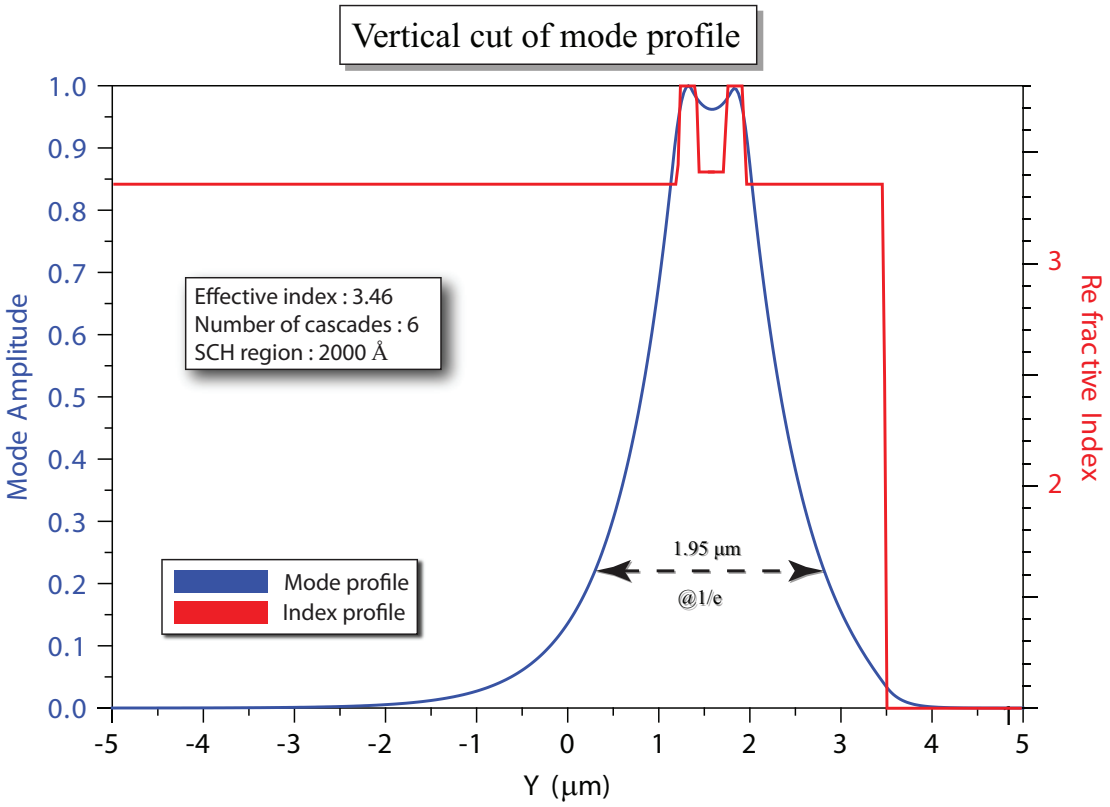

Figure 4.10: Mode profile of a 6 cascade separate confinement region (SCH) ICL.

space and $\vartheta_0 = 18°$ inside the semiconductor laser which has a $n_{eff} = 3.46$.

In order to calculate the facet reflectivity of a tightly confined mode accurately, we are going to have to break down the mode into a sum of many different plane wave components[92, 93, 94] as is illustrated in figure 4.12. At the top of that figure we show the fundamental mode incident on the laser facet, while at the bottom we show how each incident plane wave contributes a different spacial frequency along the interface. Each of these frequencies is going to be our basis for the Fourier analysis of the mode. As we expect a plane wave at normal incidence would create a $k_x = 0$, which would give us a δ function in Fourier space centered at our wavelength of interest. However as we are narrowing down the mode size, we are broadening

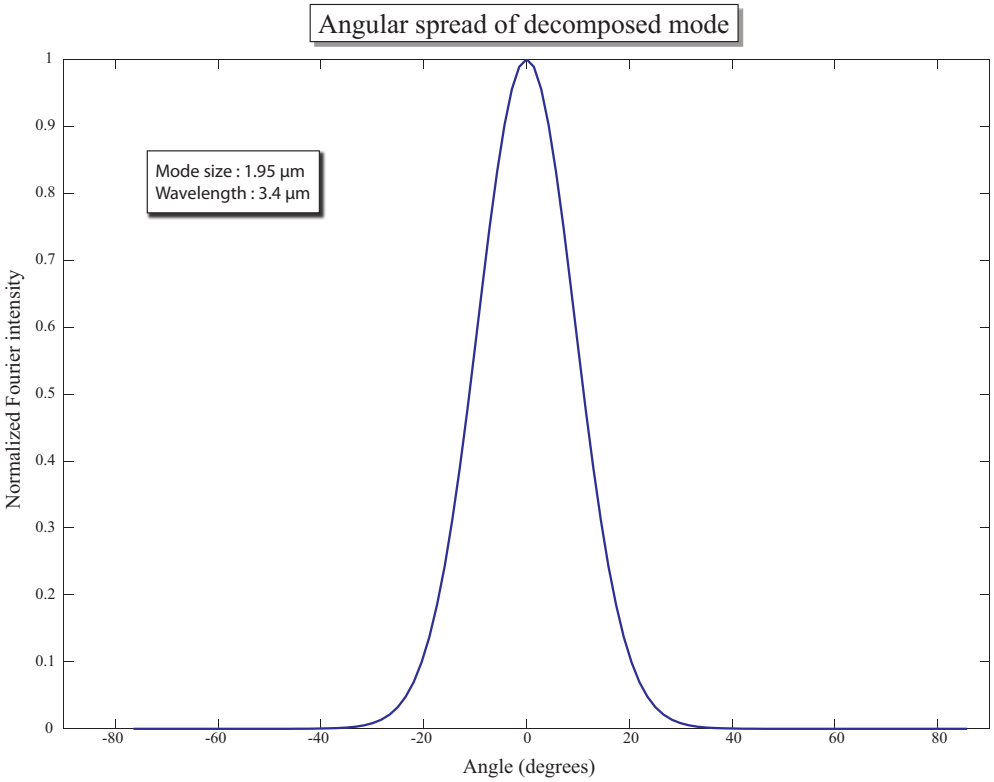

Figure 4.11: Angular spread of the fundamental mode

the spectrum along the interface. Assuming that the wavelength λ is constant, the k vector would also have a constant amplitude regardless of its direction. A unique pair of (k_x, k_z) values belong to each incident plane wave such that:

$$\tan \vartheta = \frac{k_x}{k_z} \tag{4.53}$$

Knowing k_x and λ will provide k_z:

$$k_z^2 = n_{eff}^2 k_0^2 - k_x^2 \tag{4.54}$$

where k_0 is the free space wavevector.

The n_{eff} is the effective index of the mode (or $n_{substrate}$ in case we do not have a waveguide). The Fourier analysis of the mode will therefore give us the

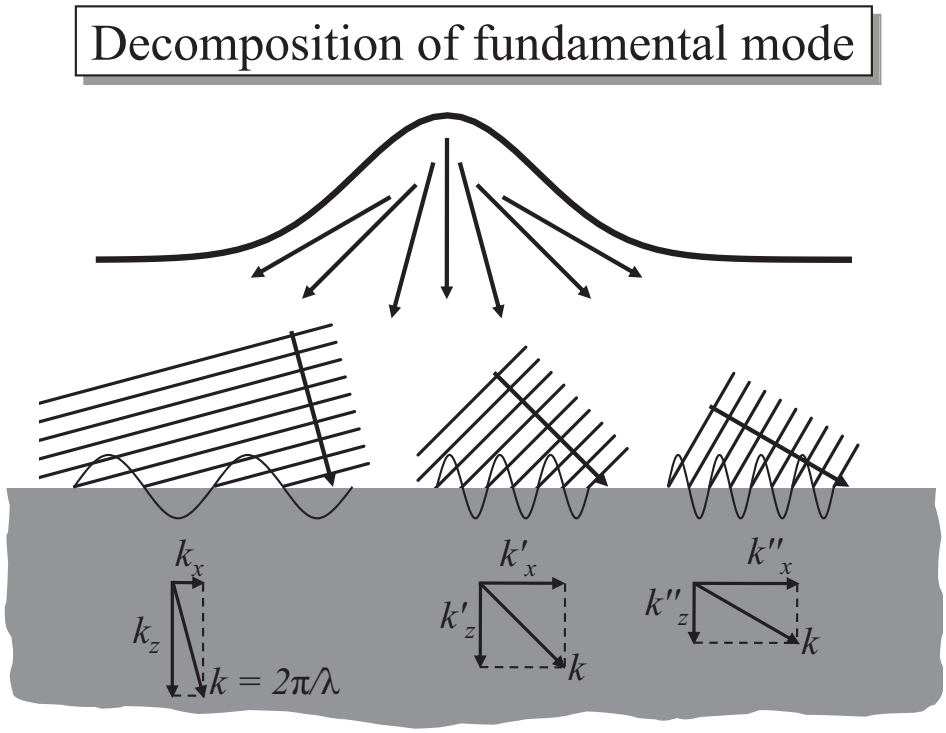

Figure 4.12: Modal decomposition in plane waves.

angular decomposition of the mode which is shown in figure 4.11. As we expect the $1/e$ point of the field amplitude profile matches the number we get from equation 4.52. It is very important to note that although in this case the major part of the mode is contained within a full angle of 36°, that is not always the case. For example in the case of fewer cascades in the active region or of lasers emitting at longer wavelength, we could potentially broaden the mode spectrum beyond $k_x = n_{eff}{}^{2\pi}/\lambda = n_{eff}k_0$. According to (4.53), this will yield components at imaginary angles. Those components represent their evanescent counterparts and do not affect any of our equations which hold even with complex arguments.

4.2.7 Decomposed mode reflectivity

In the previous section we covered how we can decompose a mode into a sum of many different plane wave components using Fourier analysis. Here we are going to use that in order to calculate the modal reflectivity.

4.2.7.1 Effective index approximation

Consider $E_i(x)$ as the electric field along the interface, as shown in figure 4.14a. In this case we will treat the waveguide, so both the active and cladding regions can be considered as a bulk region with index n_{eff}, which is calculated by solving for the waveguide mode. Its angular dependence will be described in terms of $k_x$by the following formula:

$$\mathcal{F}\{E_i\} = \int_{-\infty}^{\infty} E_i(x) e^{-ik_x x} dx \tag{4.55}$$

k_x defines the angle of incidence according to (4.53). Using equation (4.42) and table 4.1 we can calculate the reflection coefficient $r(k_x)$ of a plane wave at any angle or for any wavevector k_x. The reflected spectrum is given by $r(k_x)\mathcal{F}\{E_i\}$. In order to calculate the reflected mode we need to do an inverse Fourier transform:

$$E_r(x) = \frac{1}{2\pi} \int_{-\infty}^{\infty} r(k_x)\mathcal{F}\{E_i\} e^{ik_x x} dk_x \tag{4.56}$$

For the total facet reflectivity, we have to account for the waveguide. Not all reflected light will couple back to the waveguide, therefore we have to perform an overlap integration of the E_i and E_r as shown right below:

$$R = \frac{\int E_i^*(x) E_r(x) dx}{\int |E_i(x)|^2 dx} \Rightarrow R = \frac{\iiint E_i^*(x) r(k_x) E_i(x') e^{-ik_x(x'-x)} dx dx' dk_x}{2\pi \int |E_i(x)|^2 dx} \tag{4.57}$$

R will ultimately give us the reflectivity value we are interested in, which shows the amount of power being coupled back to the laser after reflecting back from a multilayered coated facet, accounting for the beam diffraction.

4.2.7.2 Angled facet reflectivity

All the equations above could also be used for light incident at an angle as well as for angled facet lasers[95, 96]. As shown in the figure on the right, the phase fronts of a wave E_i incident at an angle, can also be represented by a wave $E_i e^{ik_x x}$ at normal incidence. By substituting E_i in (4.57) we get

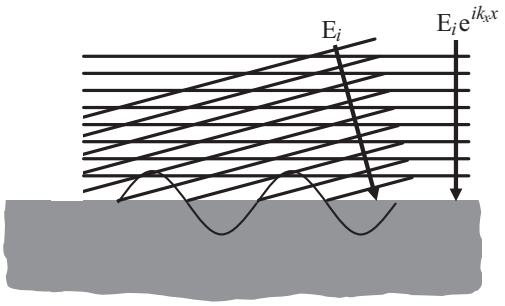

Figure 4.13: Angled incidence of light.

$$R = \frac{\iiint E_i^*(x) r(k_x) E_i(x') e^{ik'_x(x'-x) - ik_x(x'-x)} dx dx' dk_x}{2\pi \int |E_i(x)|^2 dx} \tag{4.58}$$

where k'_x determines the angle of incidence

4.2.7.3 Mode breakdown in regions with different index of refraction

This approach[97] is very similar to the effective index approximation, but instead we calculate the facet reflectivity by breaking down the calculation into two separate sums. One for each of the regions depicted in 4.14b. For the mode in

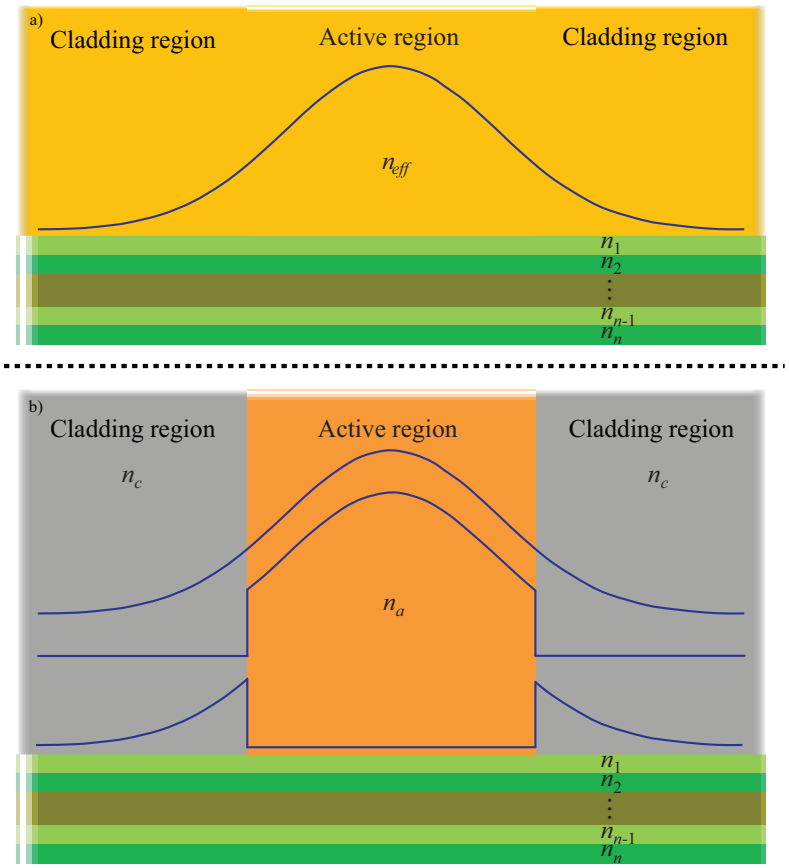

Figure 4.14: Comparison of the (a) effective index approximation and (b) mode breakdown into cladding and active region.

the cladding region we will calculate the reflection coefficient r using n_c as the bulk index and for the active region mode we will calculate r using n_a as the bulk index. Using equation (4.57), the total reflectivity is given by the following equation:

$$R = \frac{1}{2\pi \int |E_i(x)|^2 dx} \int E_i^*(x) \Big(\iint_{x',clad} r_c(k_x) E_{ic}(x') e^{-ik_x(x'-x)} dx dx' dk_x + \\ + \iint_{x',active} r_a(k_x) E_{ia}(x') e^{-ik_x(x'-x)} dx dx' dk_x \Big) \tag{4.59}$$

where r_c, r_a are the reflection coefficients at various angles for the cladding and the active region

E_{ic}, E_{ia} are the electric fields in the cladding and active regions as shown in figure 3.14b

This approach is more accurate than the effective index approach in section (4.2.7.1), since it calculates the reflection of each region based on their actual indices, however there are two main disadvantages that make this approach more calculation intensive. First we have to compute the Fourier transform of two functions E_{ic} and E_{ia} instead of one. But most importantly, because both functions have very sharp features at the cladding-active interface as shown in 4.14b, where the field jumps to zero, the angular decomposition of each field component extends to a very wide range of k_x values, requiring us to not only use higher spatial resolution in our simulation, but also to integrate over a larger span of values in order to calculate E_r given by eq.(4.56). The two methods give similar results. Therefore in order to improve the speed of our simulation, we use the effective index approach and integrate only over a narrow value range of k_x which includes our k_x spectral decomposition.

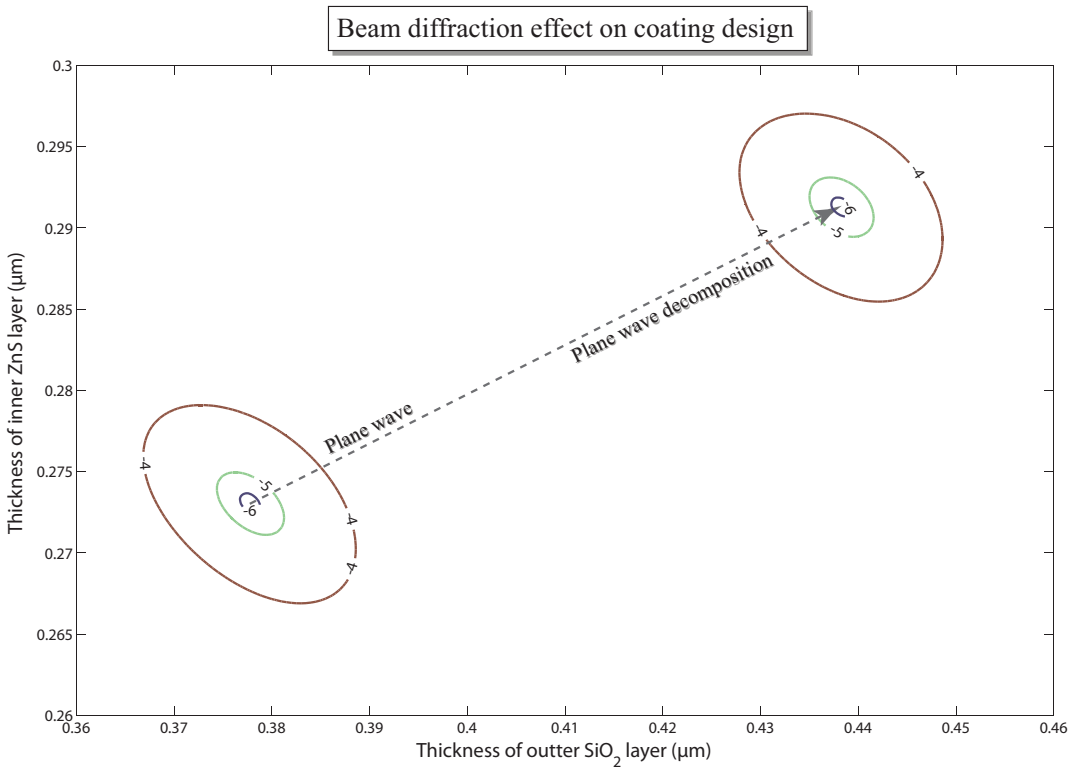

Figure 4.15: Comparison of the plane wave with the decomposed mode merit function contour

4.2.8 Simulation results

Just to get an idea on how much beam diffraction affects our results, based on Fresnel's equation (4.1), the bare facet of a 6 cascade laser with an effective index of refraction $n_{eff} = 3.46$, would give us $R = 30.39\%$. In reality the mode shown in figure 4.10 would have $R = 38.39\%$ which gives a significant 8 percentage points error. Figure 4.9 shows the contour of the merit function of the device just mentioned based on a $100\,nm$ bandwidth centered at $3.4\,\mu m$. How different is that plot from the simplified plane wave case? A quick glance at Figure 4.15 will answer that question. We observe a significant change in the coating design by about $20\,nm$ for the inner layer and more than $60\,nm$ for the outer layer. The requirement for a

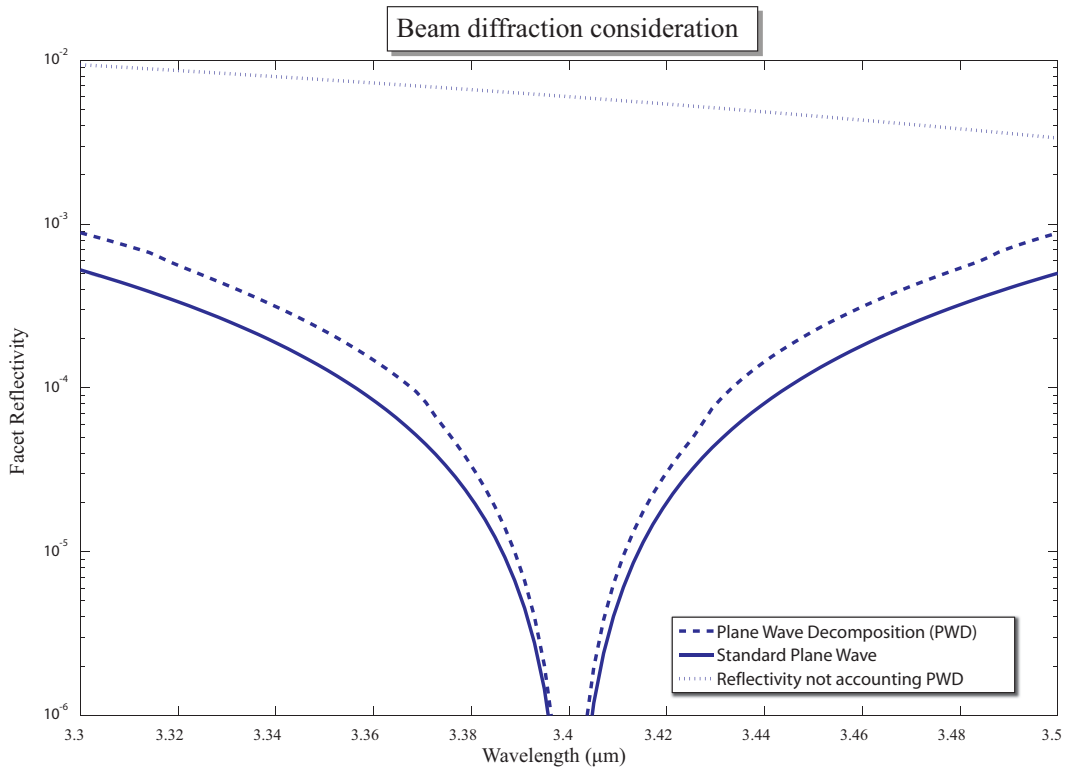

Figure 4.16: Comparison plot of the (dashed) modal reflectivity, (solid) plane wave reflectivity, (dotted) not accounting for plane wave decomposition.

low reflectivity coating used in an external cavity configuration is $R < 10^{-4}$. Based on that contour plot, the traditional plane wave approach does not even get us close. How far it would actually get us is shown in figure 4.16 . The solid line shows the spectrum of a coating designed for a plane wave at $3.4\,\mu m$. The dashed line shows the spectrum of a coating designed for a $1.95\,\mu m$ mode at the same wavelength. As we would have expected, the plane wave has lower reflectivity than a diffracting mode. It is important to emphasize that those two plots are products of different coating designs and that is why they both work. If we had not accounted for the beam diffraction and for example used the coating solution located on the lower left side of figure 4.15 for the $1.95\,\mu m$ wide beam, then we would get the dotted spectral

line, shown at the top of the figure, which would give us $R \sim 5 \cdot 10^{-3}$. That leads to a much higher reflectivity than the one desired for an application like an external cavity laser.

4.3 Fabrication of IC-AR coatings

After having studied the fundamental theory behind the design of low reflectivity AR coatings and having created the tools that enable us to do that accurately and quickly, we have reached the point were we need to try out our designs and test their viability. In summary, the process flow that we follow can be represented by the following steps:

- Mode calculation and n_{eff} determination for devices of various width, cascade number, epi structure.
- Calculation and design of an AR coating with specific performance characteristics like wavelength of operation and bandwidth at a nominal reflectivity.
- n_{eff} and the coating bandwidth will determine the type of materials we are looking for our coating (see fig.4.6).
- Using table 4.4, as well as other resources, we identify candidate materials for e-beam evaporation
- Test of the evaporation process and film quality on test substrates.
- Index measurement of evaporated films using *in-situ* ellipsometry

- Decide on one material system and proceed with AR coating evaporation on actual device using reflectometry.

- Characterization of the IC laser device

The first four process steps are done sitting in front of a computer. The last four require experimental effort.

As we saw in the previous section a typical number for n_{eff} is 3.457. Our starting point for materials is dictated by (4.49). Therefore the ideal material system would be (HL)= 2.53/1.36. A first glance will show that ZnSe/MgF_2matches very well the index criterion. However calibration growth runs on MgF_2 showed that without the use of ion assisted deposition, which is a method to grow high packing density films by ion bombardment during the growth, the films are porous having a tendency to absorb humidity once outside the chamber. This leads to a change in the nominal refractive index of the material, but most importantly the film has transient properties which have a devastating effect in the lifetime and reliability of the coating. The next group of potential candidates for the second material are SiO_2, CaF_2 and BaF_2 with indices 1.48, 1.42, 1.46 correspondingly. CaF_2 and BaF_2 show similar behavior to MgF_2, therefore we decided to go ahead with SiO_2 because it is a material we have worked with in the past, but also SiO_2 offers the possibility of densifying the film by performing growth in an atmosphere of O_2 by either evaporating in low vacuum ($\sim 10^{-4} - 10^{-5}$), or evacuating down to $< 10^{-6}$ and evaporating in a partial pressure of $O_2 \sim 10^{-5}$ maintained through the use of a gas flow controller. Once again according to (4.49), after having decided that the

low index material we are going to be using is SiO_2, the high index material should have $n = 2.33$. ZnS is our material of choice. Regarding the porosity of the inner material, we have less of a concern since that layer will be passivated by the outer SiO_2 layer. Although ZnS is a soft material and does not produce scratch resistant coatings, it is very easy to evaporate.

4.3.1 E-beam evaporation facility

Figure 4.17 shows a diagram of the e-beam system we used for our AR coatings. It is a conventional e-beam system comprised of an e-gun that accelerates thermionic electrons under high voltage onto our target material sitting inside a crucible. After preconditioning of the melted material we are ready to start evaporating as soon as we open the shutter. Preconditioning is an essential step if we want to avoid fluctuations in the evaporation rate and spitting, which occurs due to violent outgassing of the material, that will reduce the quality of our film. The evaporated material starts forming a thin film, like boiling water on a lid, on the test sample or the laser device of interest sitting opposite to the target material. The chamber is evacuated using a turbomolecular pump backed by a rotary mechanical pump. The chamber is equipped with a crystal monitor for approximate thickness measurement, and has an inlet for gas flow control. A heating element on the back of our sample can increase the temperature of the sample for improved deposition conditions. The most prominent feature of this system however is an *in-situ* ellipsometer/reflectometer that allows us to grow thin films with very high

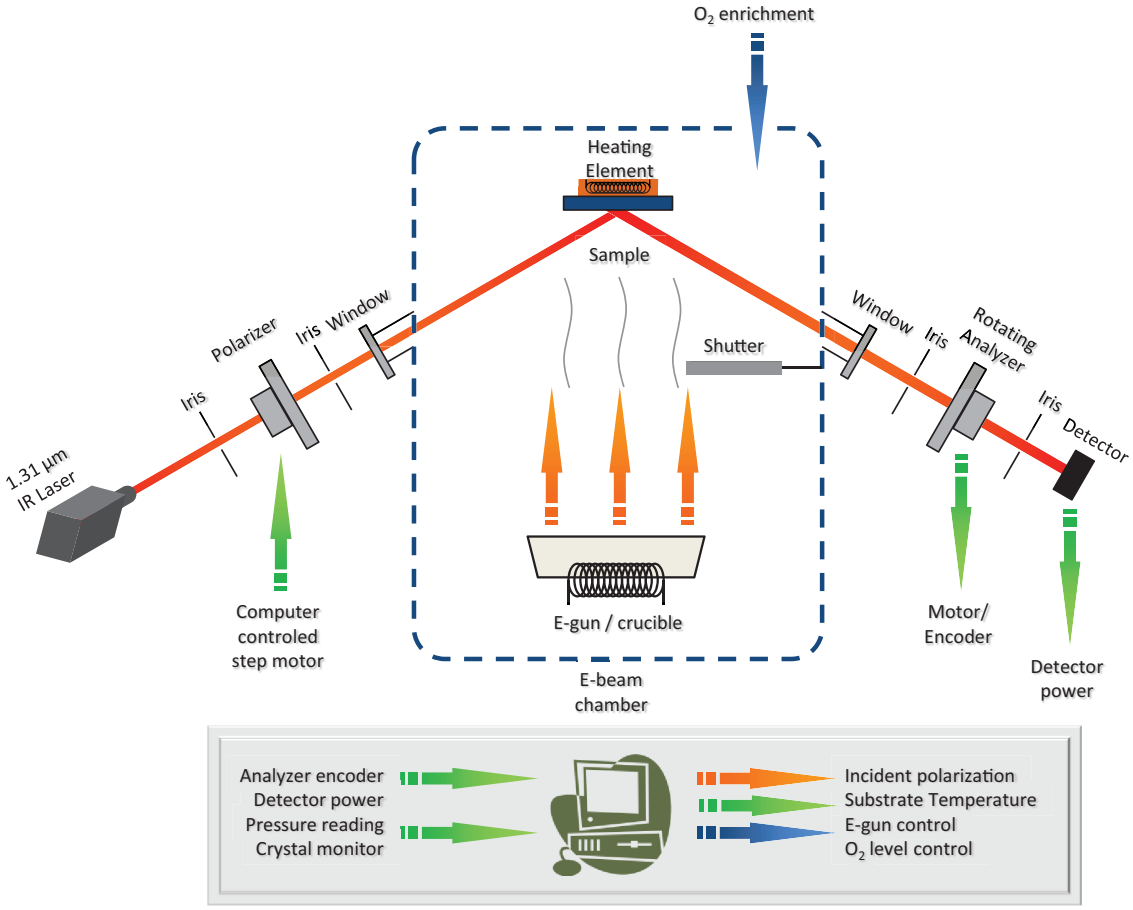

Figure 4.17: E-beam evaporation facility equipped with and *in-situ* ellipsometer/reflectometer.

accuracy. As shown in figure 4.9 a coating of $R < 10^{-4}$ requires films grown with $< 10\,nm$ accuracy. That cannot be achieved by using a crystal monitor alone. All these deposition controls as well as the ellipsometry/reflectometry parameters are monitored through a computer system.

4.3.2 Ellipsometry

Ellipsometry is one of the most accurate ways to determine the thickness and the index of a thin film. A rotating analyzer ellipsometric setup in principle is very similar to the ellipsometer shown in figure 4.17 and includes only the components that cross the light's path.

In detail it comprises of a non or circularly polarized collimated light source, a motorized polarizer, a mount where our film sample is placed, a rotating analyzer (analyzer = polarizer) and a detector. The purpose of the irises is to maintain the axis of the light. Every time a new sample is mounted on the sample holder, we perform an alignment step in order to align the optical axis of the reflected light with the irises. The wavelength of light we use on our e-beam system is 1.31 μm, however our tabletop ellipsometer is a multiwavelength ellipsometer. Please note that the wavelength we use during the ellipsometric measurement has nothing to do with the wavelength of operation of our laser. The wavelength of operation of the ellipsometer determines the material properties at that wavelength only. The film thickness is not a material property and therefore its value is unaffected by the type of light source we use. The index however might change based on material dispersion. Therefore it is advisable to operate the ellipsometer near the wavelength of interest. Multiwavelength ellipsometers offer the flexibility to determine the material index over a wide spectral range. Typically gas lamps (eg.Xenon) with discreet spectral lines can be used. By fitting the index spectrum, that we measure with the ellipsometer, with the Cauchy formula:

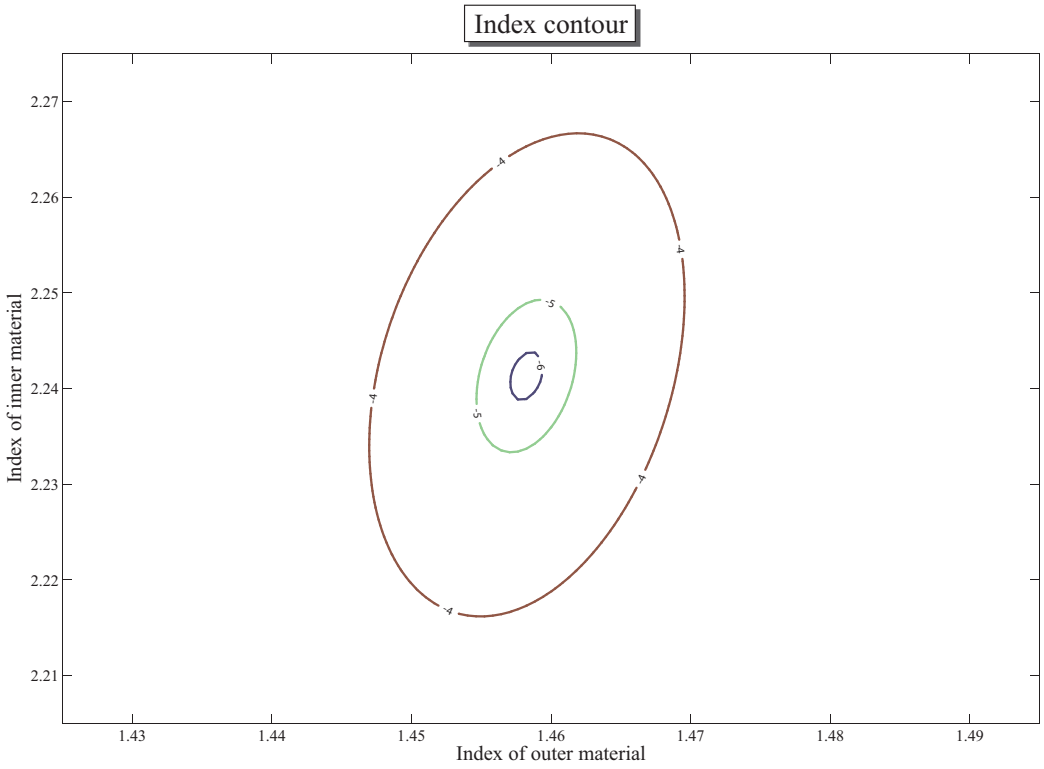

Figure 4.18: Index contour illustrating the grown material index tolerance

$$n(\lambda) = A + \frac{B}{\lambda^2} + \frac{C}{\lambda^4} + \cdots \tag{4.60}$$

or the Sellmeier equation which models more accurately the refractive index:

$$n^2(\lambda) = 1 + \frac{B_1\lambda^2}{\lambda^2 - C_1} + \frac{B_2\lambda^2}{\lambda^2 - C_2} + \frac{B_3\lambda^2}{\lambda^2 - C_3} \tag{4.61}$$

we can obtain index values at our wavelength of interest. Recently, since there has been increased interest in the mid-IR and far-IR, commercial ellipsometers have been developed operating in that wavelength range. Since we did not have access to mid-IR ellipsometers, we performed our index measurement with a multiwavelength ellipsometer operating in the visible range. According to the Cauchy equation (4.60)

and as long as the material of interest does not have any absorption resonance peaks, which is not quite true for SiO_2 in the $3.4\mu m$ range, the ratio $|^{dn}/_{d\lambda}|$ becomes smaller at longer wavelengths. Therefore we can more accurately extrapolate in the mid-IR since there is less dispersion. Figure 4.18 shows how much tolerance we have in the refractive index of our grown material assuming the coating thickness is precisely grown. Index precision of < 0.05 for the inner layer and < 0.02 for the outer layer is necessary. Those lax requirements become more stringent at shorter wavelength of operation. At mid-IR due to the long wavelength we benefit in terms of large film tolerances, but we suffer from thick coating films that are more susceptible to stress, manifesting in film delamination. Using our ellipsometer we have been able to obtain the index of ZnS at $3.4\,\mu m$ with a 0.02 error and SiO_2 with < 0.001 error. The refractive index spectrum of both ZnS and SiO_2 is illustrated in figure 4.19. It is obvious that material dispersion has a smaller effect in the mid-IR. For more information on the theory of ellipsometry please refer to appendix C.

4.3.3 Film growth based on reflectometry

After calibrating the polarizer and analyzer azimuths, its time to grow the coating film. For monitoring the growth of the film we have chosen to use a reflectometric approach instead due to its simplicity. According to this method we monitor the reflected light intensity of either the s or the p polarization without the use of a rotating analyzer. Since our incident polarization is perfectly TE(s) or TM(p) and our e-beam grown films are considered to exhibit little or no bire-

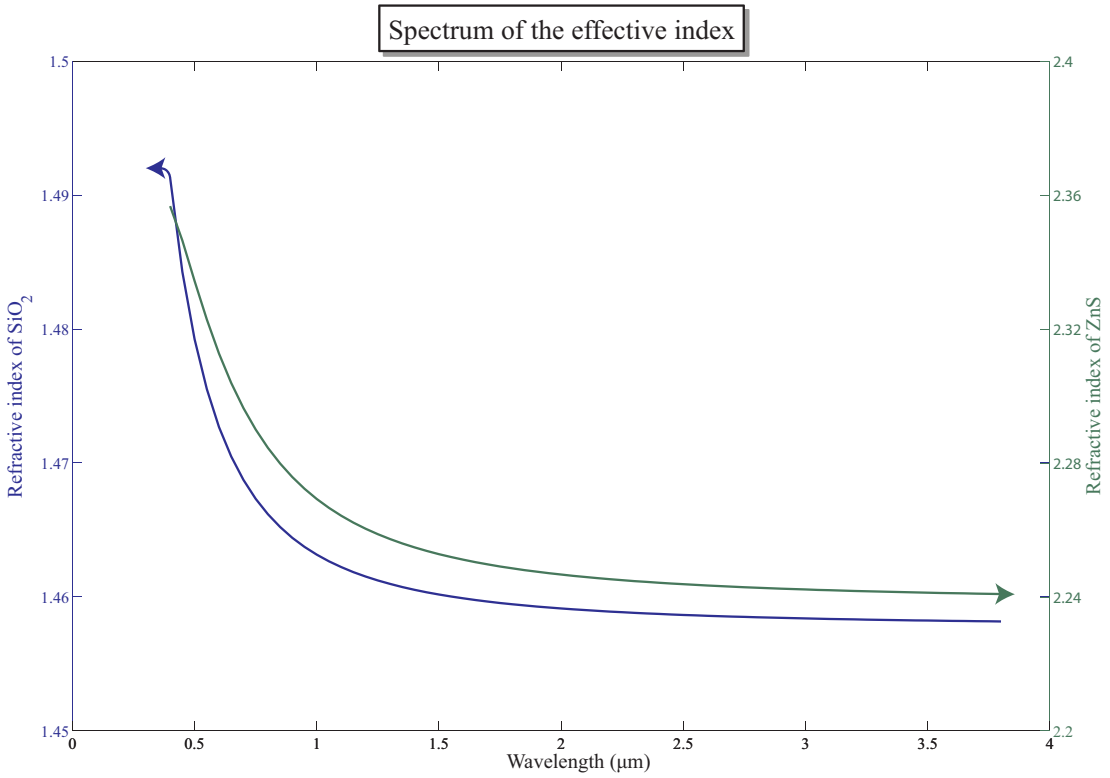

Figure 4.19: Refractive index spectrum of ZnS and SiO_2.

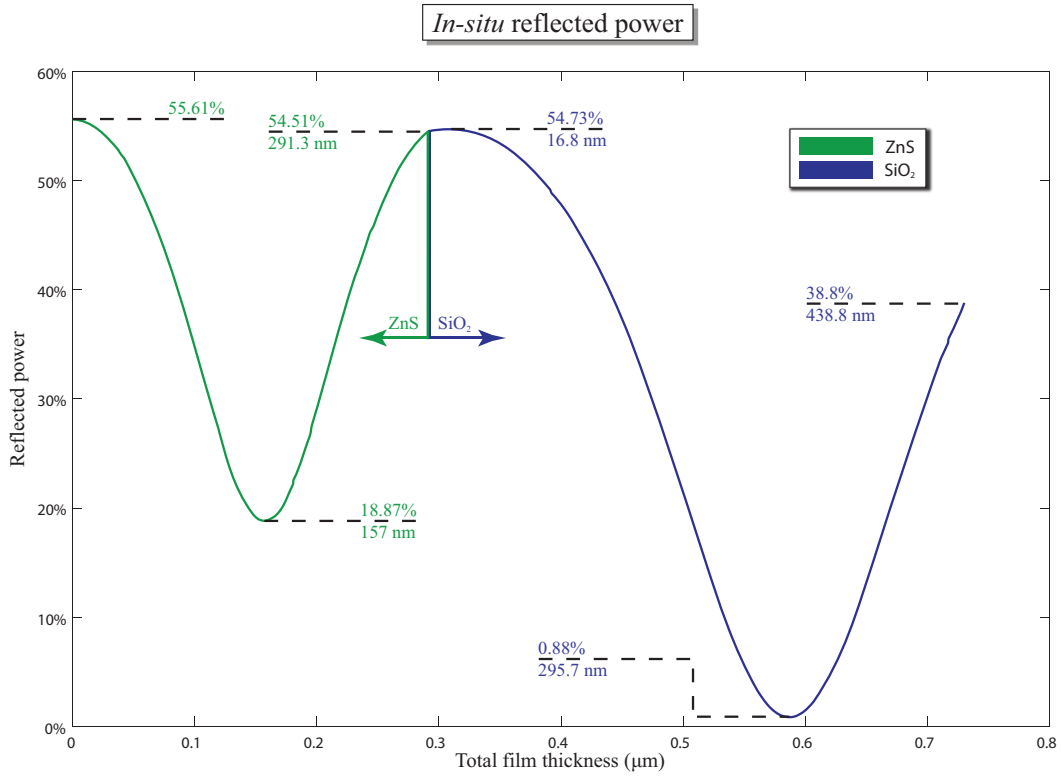

Figure 4.20: Reflected power dependence on film thickness.

fringence, the reflected light maintains its linear polarization. Therefore assuming we have already determined the coating material indices, equation (4.42) can provide a relation between the grown film thickness and reflected power. Figure 4.20 illustrates that relation. During the evaporation process we constantly monitor the reflected power. As soon as it reaches the desired number, in our case 54.51%, it is time to change the target material from ZnS to SiO_2. We resume the evaporation process until we finally reach our goal of 38.8%. One important thing to note, is that this method provides very good thickness precision when the power slope is high. We can see that especially for the SiO_2 cycle that works out very well. In case the process interruption needs to happen on a local extremum we can change the monitor wavelength if necessary.

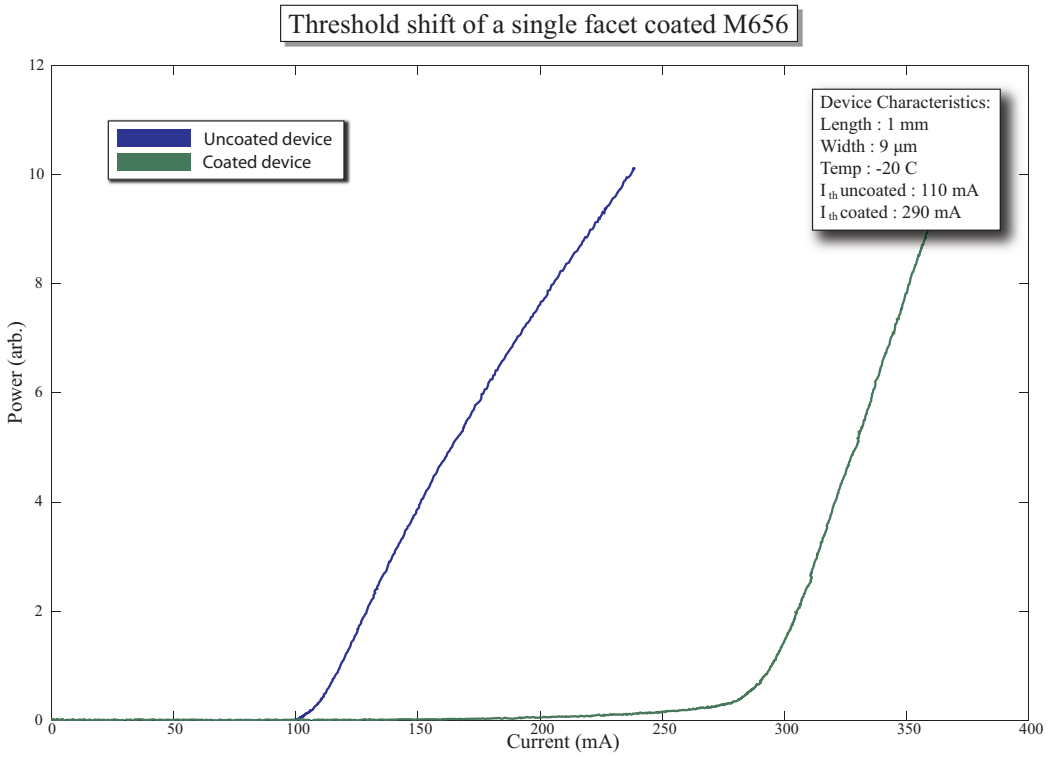

Figure 4.21: IL measurement comparison of a coated and an uncoated laser device.

Once the laser device is out of the chamber it is ready to be tested. The first manifestation of low reflectivity coating is in the operating threshold shift. Figure 4.21 shows the IL measurement of an IC laser before and after dielectric coating deposition. This shift is a measure of the coating quality. As we saw in chapter 2 in eq.(2.25):

$$J_{th} = J_T + c\frac{\ln\left(\frac{1}{R_1 R_2}\right)}{L} \tag{4.62}$$

where J_T is much larger than the transparency current density according to the assumption we made right after eq.(2.25). From length dependence measurements we have extracted the parameter $J_T \approx 500\text{A/cm}^2$. If $J_{th,c}$, $J_{th,un}$,$R_{2,c}$, $R_{2,un}$ are the threshold current densities and facet reflectivity for the coated and uncoated facet,

assuming that R_1 stays the same we obtain:

$$\frac{J_{th,c} - J_T}{J_{th,un} - J_T} = \frac{\ln\left(\frac{1}{R_1 R_{2,c}}\right)}{\ln\left(\frac{1}{R_1 R_{2,un}}\right)} \tag{4.63}$$

Using the parameters at the figure inset and a bare facet reflectivity $R_1 = 30\%$, we obtain a coating reflectivity of:

$$R_{2,c} = 3.4 \cdot 10^{-5} \tag{4.64}$$

This result is very encouraging and allows us to proceed to the next step of our work which is to build an external cavity laser.

Chapter 5

Interband cascade external cavity lasers

5.1 Introduction

In the past two chapters we analyzed in detail the fabrication process for making interband cascade lasers which are then AR coated to suppress the Fabry Perot modes of the chip cavity. In order to achieve tunability we need to introduce a wavelength selective element in the optical cavity. An external diffraction grating can be used to provide the wavelength selection and to extend the laser cavity outside of the gain medium defined by the laser chip. In order for a chip mounted in an external cavity to lase, it has to overcome the cavity losses. The wavelength with minimal cavity losses will define the output wavelength of the laser. In this chapter we are first going to present the fundamental grating theory and then discuss the principles of operation of an external cavity laser.

5.2 Diffraction gratings

5.2.1 Slits, gratings, blazing

A diffraction grating[98] can be described as an ordered collection of single slits. In a similar fashion a single slit can be divided into a large amount of sub-slits. A slit divided into sub-slits is illustrated in figure 5.1.a. Each arrow in the figure illustrates the electric field for each corresponding sub-slit. Assuming that a plane wave is coming out of the slit, each sub-slit would be represented by an electric field phasor, all of which are in phase along the slit. If we consider that point A is far, so that R $>>$ 0 and $\phi \rightarrow 0$, R can be assumed the same for every sub-slit and therefore the resulting electric field in A, given by the vectorial sum of the field phasors, is now the same as the scalar sum, as shown on the right side of figure 5.1.a, since A is laying on the perpendicular bisector of the slit. Figure 5.1.b is simply a rotation of figure 5.1.a. The idea here is to show how the electric field changes with varying angle when we have a plane wave emerging from the slit. This could happen by either back illuminating the slit or illuminating from the front from point A. From the figure we see that depending on the angles, with respect to the slit, of points B and C we can determine the curvature of the arc defined by the field phasors. The constituent phasors for A, B, and C are the phasors along the a, b and c wavefronts correspondingly. The vector sum $\vec{E}_0$ will define the electric field. In the special case where the phasors go on a half-circle, the phase difference between one edge of the slit and the other edge is π.

Figure 5.1 shows the effect of a slit on the electric field. As we know this effect

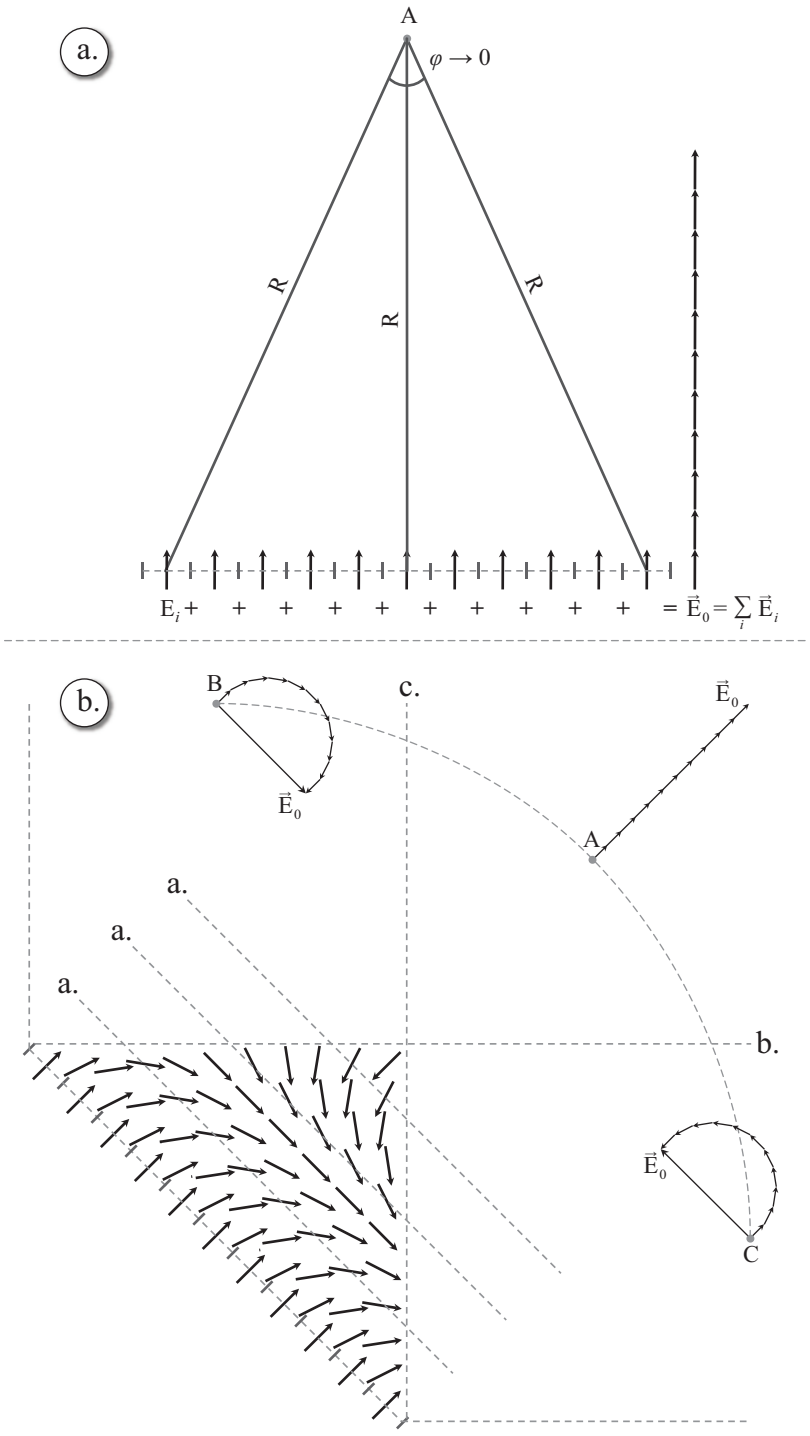

Figure 5.1: Single slit. Electric field on the bisector (a). Electric field at an angle (b).

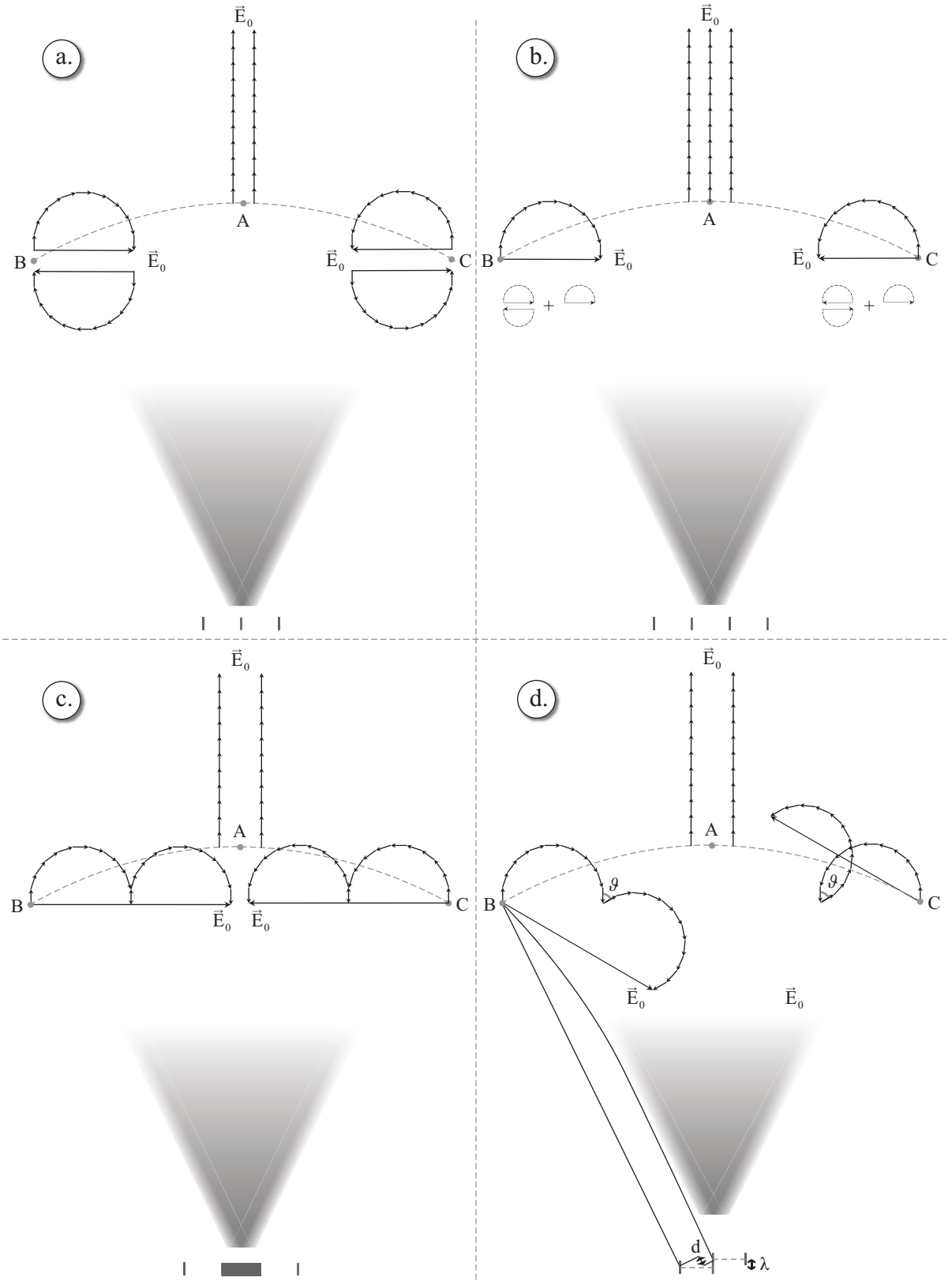

Figure 5.2: Important cases of stacked slits (Grating).

is called diffraction. What happens if we stack multiple slits one next to the other? Figure 5.2 illustrates four important cases. First 5.2.a shows what happens when we put two slits one next to the other. As we can see from the figure the electric field is enhanced constructively at point A, however as we are moving away from A the field is starting to weaken until each slit destructively cancels itself at point B and C. The more slits we add the stronger the field is at A, while the field at B and C remains infinitesimally small because all slits cancel each other as shown in 5.2.b. This case is a degenerate case, also known as a mirror or a big hole. When we have a large number of slits all we get is light at point A, thus all diffraction effects are wiped out.

In order to promote the diffracted orders we introduce a phase lag between slits. One way to do this is by blocking every second slit as illustrated in 5.2.c. As we can see in the phasor diagram this phase lag can be adjusted so that each slit constructively interferes with its neighbors so that we get pronounced diffracted orders. However those orders have less intensity than the zeroth order at point A, due to the curvature of the vectorial sum. Another issue is that due to the fact that we block half the slits, we lose light.

One way to promote the diffracted orders without losing light is by causing the appropriate phase delay by placing the slits in a staircase fashion as shown in figure 5.2.d. In the case illustrated the slit step is λ. This configuration provides an even more pronounced diffracted order, not only because every slit is now radiating light, but also because only one wavelength λ can reach A in phase without being destructively canceled by other slits. This configuration offers wavelength selectiv-

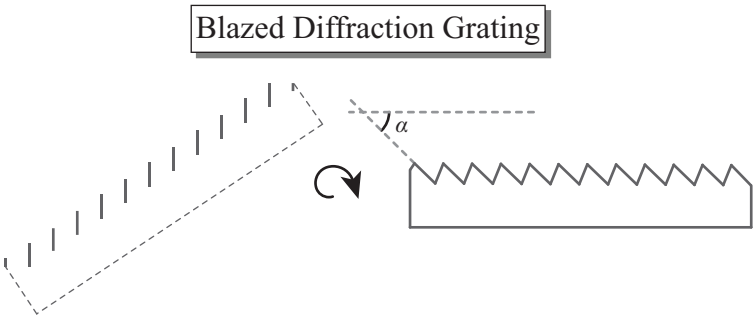

Figure 5.3: Blazed grating diagram.

ity depending on the step size of the staircase and maximum efficiency since our diffracted order is now a scalar sum of the electric field. The angle ϑ relates to the path difference d illustrated in the figure, and it is the phase difference between the first phasors of each slit. So in summary each phasor arc curvature depends on the relative angle of each slit, and the phase difference of each first phasor depends on the phase difference of each first sub-slit at the direction of interest.

Although we are not very familiar with the grating configuration as it was presented in figure 5.2.d, we soon realize that if we tilt the staircase grating as shown in figure 5.3, we obtain the familiar blazed diffraction grating. The purpose of this brief introduction to diffraction gratings was to appreciate the blazing effect of a diffraction grating. The angle α is called blaze angle and in combination with the grating pitch (period), determines the diffraction characteristics of the grating. The pitch is the most critical parameter for a grating and it governs the diffraction angle for a given wavelength. As we discussed earlier depending on our observation angle, the corresponding phasors along each slit will have a linear variation in phase, the vectorial sum of which is represented by an arc as introduced in figures 5.1 and 5.2.

The arc curvature can be compensated by rotating each slit (blazing) appropriately, so that the field is in phase in the direction of interest and therefore the phasor arc becomes a straight line. This condition will yield the highest electric field, therefore depending on the application we can design the grating in order to achieve maximum efficiency at the angle and wavelength of preference.

For example in the case of a retroreflecting wave λ, incident on the grating with pitch D and blaze angle α, the maximum efficiency will be achieved at an angle φ given by:

$$2D \sin \varphi = \lambda \tag{5.1}$$

where $\varphi = \alpha$. This occurs when incident light is normal to each slit, so that all phasors align, but at an angle a with respect to the grating. This grating configuration is named Littrow configuration after its inventor and its an important specification parameter defining the blaze wavelength of a grating. We need to point out that in this case, the separation of the slits along the axis perpendicular to the slit is $\lambda/2$, not λ as shown in figure 5.2.d. The reason for that is because during our grating study we assumed that light is coherently generated on the slit surface, so all light is in phase. On the other hand, when light is incident on the grating any potential phase delays among the slits has to be accounted for. That is why in this case we get constructive interference only when the separation is $\lambda/2$, so that light travels a distance λ when it goes on a full round trip rather than a one way trip.

5.2.2 Grating resolution, resolving power

Resolution and resolving power are two terms that are used to describe the ability to distinguish between adjacent components in a spectrum. The resolution of a grating is the smallest change of wavelength that we can resolve while the resolving power is the ratio between the wavelength resolution and the wavelength of interest. Looking back at figure 5.2.a, we see that for two slits , in order to resolve light at point A, we need to estimate at which angle corresponding to $\Delta\lambda$ the electric field goes to zero. Apparently that point is B which corresponds to $\lambda/2$ since the phasors are in a semicircle. Therefore $\Delta\lambda = \lambda/2$. For $N = 3$, the electric field would go to zero at 2/3 of the angle of point B, as shown in 5.2.b, so $\Delta\lambda = \lambda/3$. For N number of slits, the resolving angle drops proportionally, therefore $\Delta\lambda = \lambda/N$. $\lambda/\Delta\lambda$ is called the resolving power R of the grating and it is equal to:

$$R = \frac{\lambda}{\Delta\lambda} = N \tag{5.2}$$

In other words, the bigger the grating, the better. Of course grating size does not matter if we only illuminate a part of the grating. The resolving power is a very important parameter in high resolution spectrometry.

5.3 External cavity configurations

5.3.1 Littrow vs Littman

Now we are going to talk about building an external cavity configuration for our ICL. There are two main types of external cavity configurations: the Littrow[99,

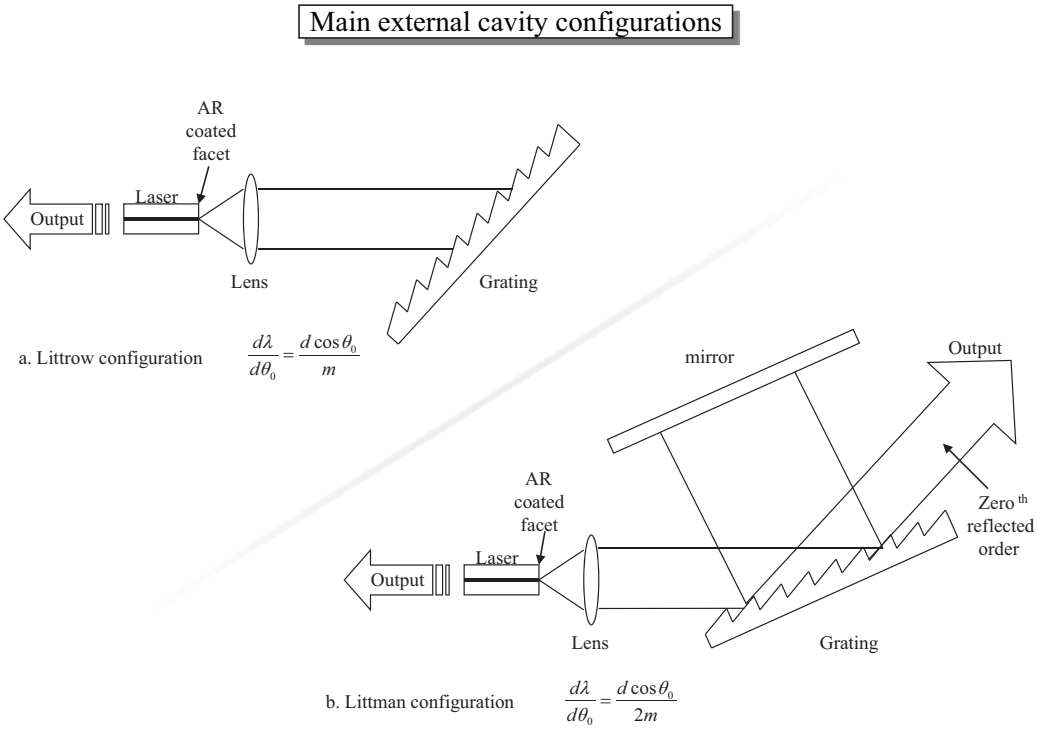

Figure 5.4: External cavity types. (a) Littrow. (b) Littman.

100, 101] configuration where a grating is retroreflecting light coming out of an AR coated laser facet, as shown in figure 5.4.a., and the Littman[102, 103] configuration where the grating is fixed at grazing incidence and the light is being retroreflected using a mirror across from the grating, allowing a double passing of the light on the grating, as shown in figure 5.4.b. Tuning for the Littrow configuration is done by rotating the grating, while for the Littman configuration tuning is achieved by rotating the mirror. After a simple grating analysis, we can derive the characteristic dispersion equations for both the Littrow and the Littman configurations[104, 105]:

$$\frac{d\lambda}{d\theta_0} = \frac{d\cos\theta_0}{m} \qquad \text{(Littrow)} \tag{5.3}$$

$$\frac{d\lambda}{d\theta_0} = \frac{d\cos\theta_0}{2m} \qquad \text{(Littman)} \tag{5.4}$$

where λ is the wavelength of interest

d is the grating pitch

m is the grating order of interest (typically 1st order)

θ_0 is the angle of incidence on the grating

There are some advantages to the Littman configuration. First, according to the equations above, for the same angular spread $d\theta_0$, $d\lambda$ is half for the Littman configuration. Why is this important? $d\lambda$ will determine the finesse of our cavity. It arises from the angular spread $d\theta_0$ of the collimated beam due to diffraction, even though the spot size is at the mm scale. Using simple Gaussian optics we derive that the diffraction angle of a collimated beam is:

$$\Delta\theta = 2\frac{w}{f} \tag{5.5}$$

where $\Delta\theta$ is the full diffraction angle of the collimated beam

w is the beam waist (mode radius at the laser facet)

f is the focal distance of the objective lens

By substituting eq.(5.5) into eqs.(5.3) and (5.4), we obtain the following equations describing the wavelength spread that couples back to the chip:

$$\Delta\lambda = \frac{2dw\cos\theta_0}{mf} \qquad \text{(Littrow)} \tag{5.6}$$

$$\Delta\lambda = \frac{dw\cos\theta_0}{mf} \qquad \text{(Littman)} \tag{5.7}$$

However in order to have such $\Delta\lambda$, it needs to be resolved according to the grating equation (5.2). This is where the second advantage of the Littman configuration

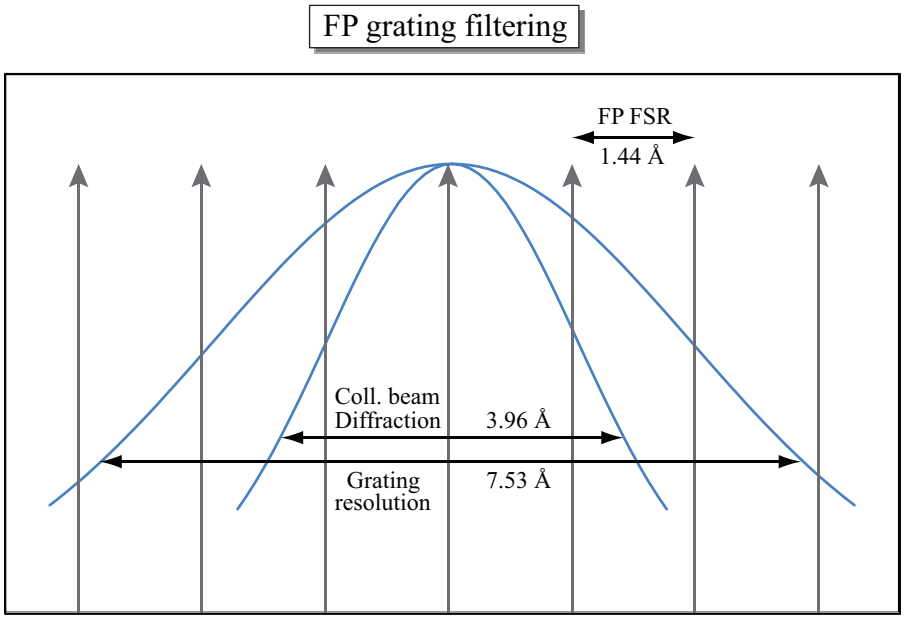

Figure 5.5: Filtering of the FP modes on a Littrow IC ECDL.

comes into play. As mentioned earlier, this configuration allows grating illumination at grazing incidence (∼85 °). That means that we can have a large number of grating lines illuminated and have very high spectral resolution. $\Delta\lambda$ can also be reduced by having a larger collimated beam. Improvements on the Littman configuration have been proposed like introducing a double grating arrangement which further reduces the bandwidth of the grating-mirror arrangement shown in figure 5.4.b[106]. The third main advantage of the Littman approach is that we can HR coat the back facet of the device and acquire the output beam from the reflection mode of the grating. That could also be done using the Littrow configuration however the output angle would change for varying grating angle (output wavelength).

3.8 μm vs 830 nm

		Littrow	Littman (grazing@60°)
Wavelength (λ)(μm)	3.8	FSR = 1.44 Å	FSR = 0.72 Å
Grating pitch (d)(μm)	5	Δλ = 3.96 Å	Δλ = 2.08 Å
Mode size/2 (w)(μm)	1	$\Delta\lambda_R$ = 7.53 Å	$\Delta\lambda_R$ = 3.96 Å
Littrow angle	18°		
Obj. Foc. Dist.(f)(mm)	24		

		Littrow	Littman (grazing@85°)
Wavelength (λ)(μm)	0.83	FSR = 0.069 Å	FSR = 0.034 Å
Grating pitch (d)(μm)	0.56	Δλ = 1.16 Å	Δλ = 0.106 Å
Mode size/2 (w)(μm)	0.22	$\Delta\lambda_R$ = 0.84 Å	$\Delta\lambda_R$ = 0.077 Å
Littrow angle	18°		
Obj. Foc. Dist.(f)(mm)	2		

Table 5.1: Comparison of the Littrow and Littman configuration at 3.8 μm and 830 nm.

5.3.2 Single mode operation

In order to get single mode operation we need to provide gain only in a single resonant mode of the cavity. Typically in Fabry-Perot (FP) lasers the free spectral range (FSR), determined by the cleaved facets of the chip, is much smaller than the gain bandwidth of the medium. For a 2 mm long ICL the typical FSR, given by:

$$\mathrm{FSR}(\lambda) = \frac{\lambda^2}{2n_{eff}L} \tag{5.8}$$

where n_{eff} is the effective index of the waveguide
L is the length of the cavity ,

is 1 nm, which is much smaller than the gain bandwidth[107, 108] which is of the order of 200-300 nm near RT. Therefore, in a typical Fabry-Perot laser, we get multimode lasing and mode hopping. In order to obtain single mode operation we need to introduce a narrow bandpass filter to allow only the desired mode to lase.

The role of the filter is performed by the grating and for single mode operation it has to offer a narrow bandwidth compared to the FSR of the cavity. The external cavity we are trying to build would have a typical length of 5 cm, so the new FSR = 1.44 Å. According to the parameters in table 5.1, for a 3.8 μm IC ECDL we get a $\Delta\lambda$ = 3.96 Å due to beam diffraction and 7.53 Å due to the grating resolution which is the dominant contribution to the wavelength linewidth. The spectrum of this bandpass filter is shown in figure 5.5 where even with Littrow configuration we can potentially get single mode operation, if we manage to get a cavity as short as 5 cm.

By looking closely at the table 5.1, we can see that there seems to be a very small benefit of the Littman configuration. The reason for that is the relatively small grazing angle (60 °). In the case of long wavelength lasers the diffraction angular spread $\Delta\theta$ is very significant for tight beams (eg. 2 mm). On the other hand wide beams (24 mm) at grazing incidence ∼85 ° would require a grating as big as 27.5 cm, which would dramatically increase our cavity length and therefore reduce the FSR. The improvement of the Littman configuration is very obvious in shorter wavelength lasers. Contrary to the longer wavelength lasers, the dominant cause of wavelength spreading is coming from the beam diffraction, as shown in the 830 nm example in table 5.1. By doing a simple calculation and assuming that the mode size scales with the wavelength, we see that a 2 mm wide beam gets a tenfold improvement when Littman is implemented, while for our ICL cavity the improvement is almost fully compensated by the cavity length increase. The reason is because for short wavelengths we can apply a large (∼85 °) grazing angle without

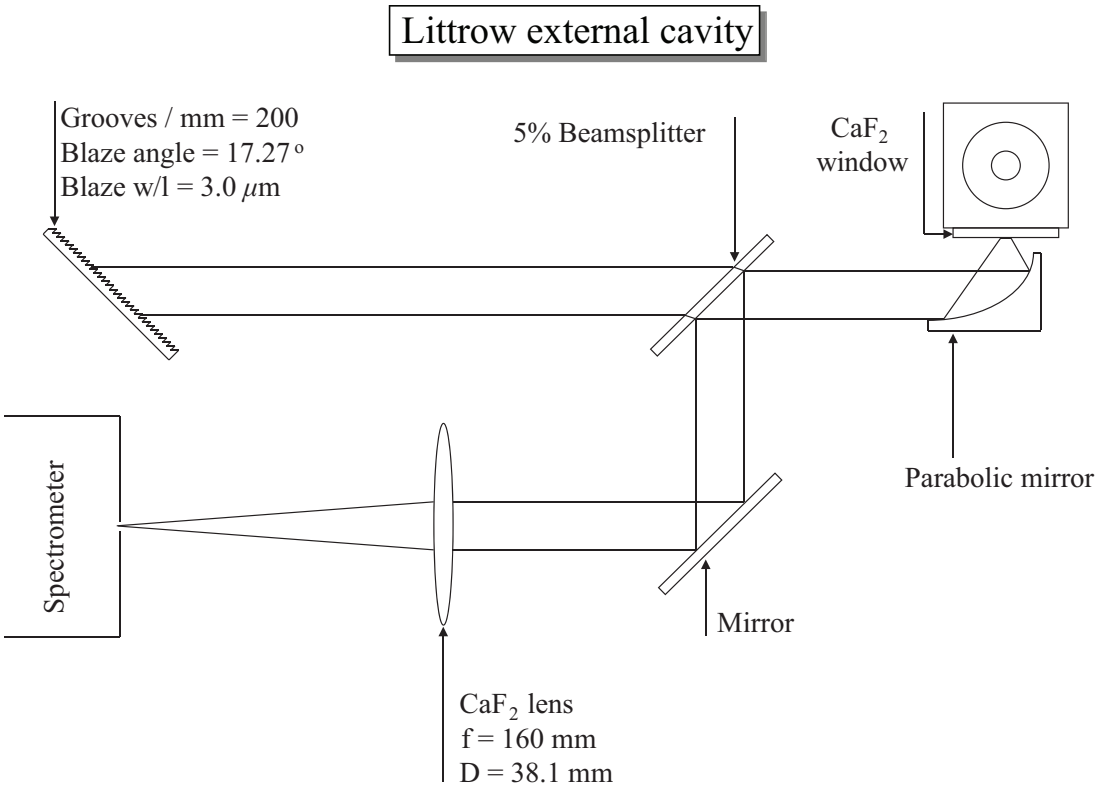

Figure 5.6: External cavity experimental setup.

significantly increasing the cavity length due to the fact that we can have a narrow beam (eg. 2 mm) without significant angular spread.

5.4 Tunability demonstration in the Mid-IR

External cavity diode lasers have been around for several years. The first demonstration of an external cavity laser was made with an external Fabry-Perot etalon. It done by Crowe *et al.*[109] in 1964. Since then there has been extensive research and widespread use in applications that require a tunable semiconductor light source. Applications like spectroscopy, atomic physics and most recently telecommunications, have been mostly based on established InP and GaAs technology. The

development of efficient light sources in the mid and far-IR in the late 90s, which later led to high power CW room temperature light sources[5, 37, 23] in the early 2000s, fueled a new interest to build external cavity lasers in those emerging wavelength regions. In 1996, mid-IR tunability was demonstrated using InAs and GaSb diode lasers[110]. Later with the development of the QCLs, broad[111, 112], mode hop free[113] tunable lasers were developed. In 2007, we pioneered the development of the first tunable interband cascade external cavity laser (IC-ECDL)[114].

5.4.1 Experimental results

The experimental setup we used, as illustrated in figure 5.6, is based on a Littrow configuration. The grating blaze angle is designed for maximum efficiency, the refractive optics are CaF_2 based, while in place of the objective lens we put a reflective parabolic component in order to avoid chromatic as well as aspheric aberrations. The lasers we used for this experiment were two 1 mm long 18 cascade ICLs one with a 70 μm wide ridge emitting at 3.8 μm and one with an 11 μm wide ridge emitting at 3.4 μm. Both lasers had a Y_2O_3 dielectric

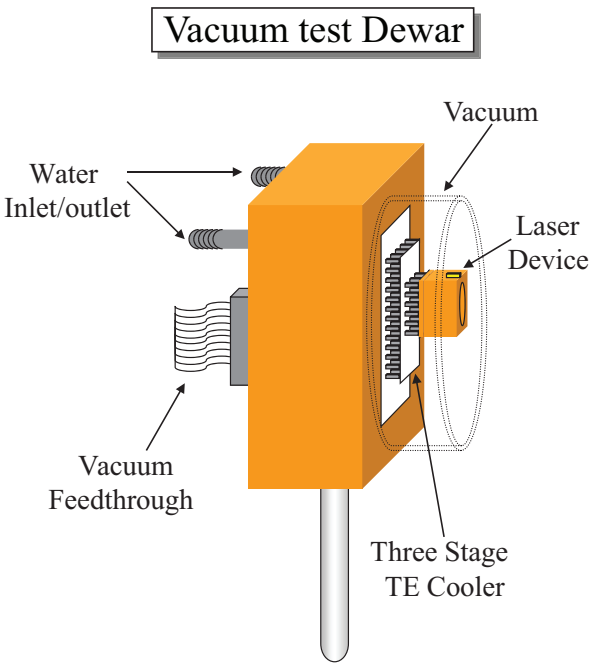

Figure 5.7: Test Dewar schematic.

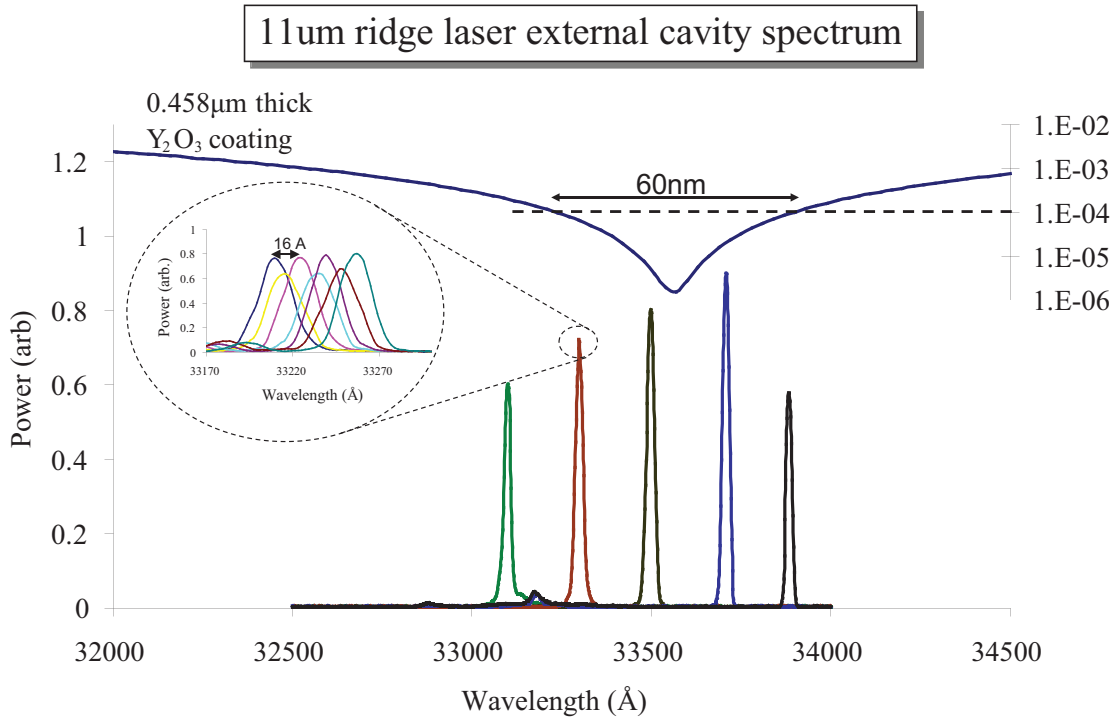

Figure 5.8: Demonstration of tunability for the 11 μm wide ridge laser.

AR coating at the front facet. We operated these lasers pulsed at 1.5 kHz with a 0.05% duty cycle at 230 K. In order to avoid condensation we build a water cooled device testing Dewar shown in figure 5.7, which allows us to operate the device in an optical setup under vacuum. As we can see from the schematic, it is hard to access the back facet of the laser when operating inside the Dewar. Therefore in order to tap off a portion of the light, we introduced inside the cavity a CaF_2 5% beam splitter, which directed the output light into a spectrometer for analysis. This modification of the cavity offered a steady output beam , however it increased our cavity length to 20 cm. The parabolic reflector has a long focal distance since close access to the laser facet is not possible due to the testing chamber's walls. In order to collect all the light we used a large and fast reflective element, which expanded

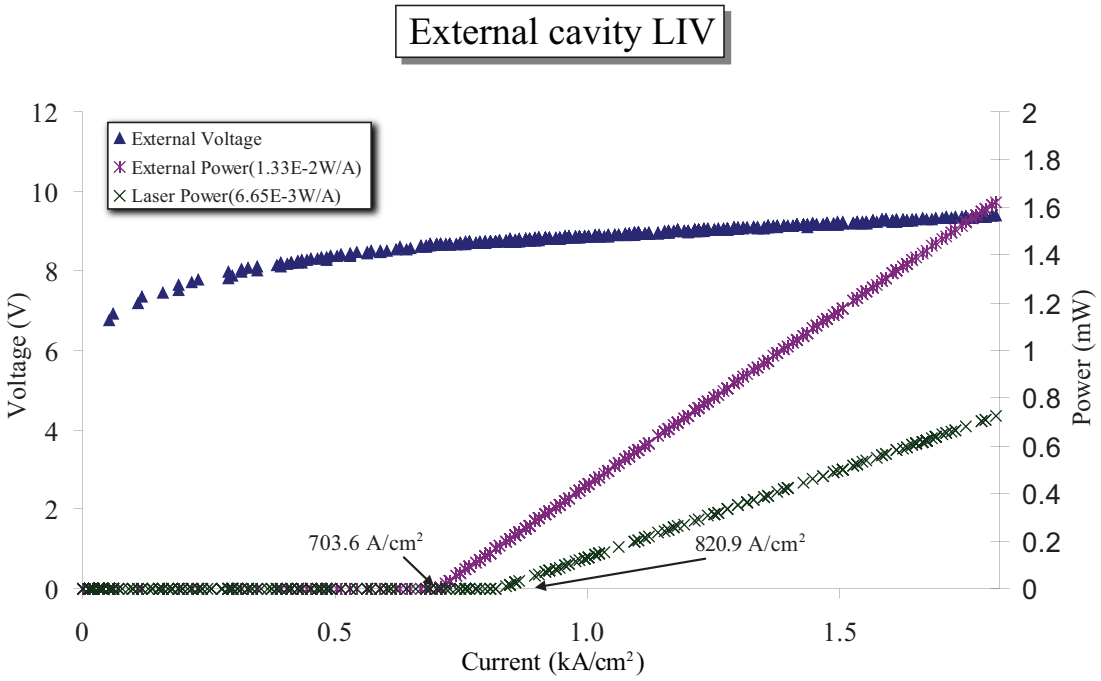

Figure 5.9: LIV of the 11 μm wide external cavity laser at 230 K.

the laser beam up to 24 mm. This wide beam also minimizes the $\Delta\theta$ diffraction angle spread mentioned earlier, and also illuminates a larger portion of the grating, increasing the resolving power of the grating.

Figure 5.8 shows the results from our 11 μm wide laser. The reflectivity of the Y_2O_3 coating is also shown in the plot. In this first demonstration we were able to obtain 80 nm tuning range. The peak linewidth was 11 Å, while due to the poor quality of the coating we see a strong ripple of 0.8 dB with a 16 Å periodicity that matches the FSR of the chip. Figure 5.9 shows the LIV characteristics of the laser. The threshold current density was 0.7 kA/cm^2 while the output peak power was 2 mW at 2.2 kA/cm^2. Note the expected threshold current density shift from 0.82 kA/cm^2 of the laser chip, when we block the grating. This power is not the

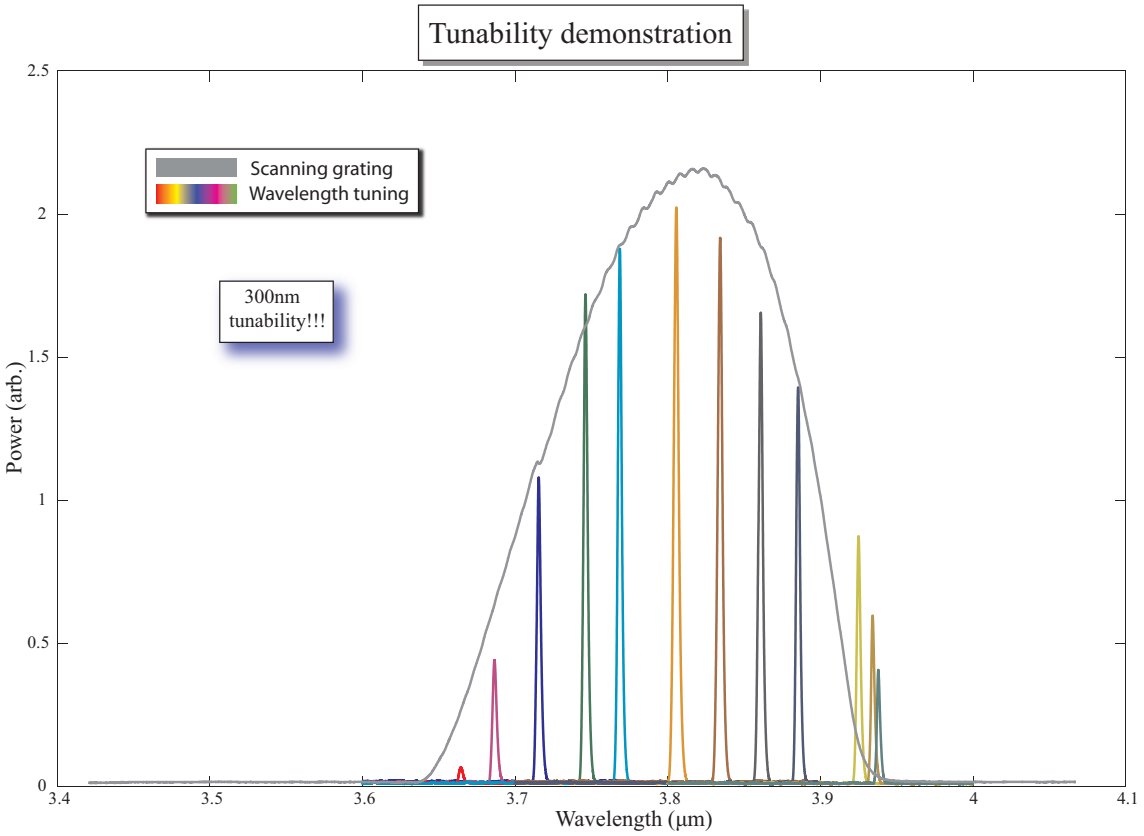

Figure 5.10: Demonstration of a 300 nm tunability range using the 70 μm ridge laser.

maximum output power since the device was operating far from the thermal roll-off point. It is expected that this power can be further optimized by adjusting the cavity losses and the length of the laser chip.

In order to improve the coupling efficiency we attempted to build an external cavity with a 70 μm wide ridge laser. This improved significantly our tuning range. Figure 5.10 demonstrates a broad tunability of 300 nm (208 cm^{-1}). To get a sense of how broad this tuning range is, we are going to compare our results with reported tunable quantum cascade laser results at 8.4 μm which gave a range of 150 cm^{-1}[115]. The FWHM of the laser linewidth was measured to be 35 Å (2.4cm^{-1}).

This linewidth indicates that the laser is not operating in a single longitudinal mode since it is much broader than the FSR of the external cavity (0.361 Å). The main reason why we got such broad linewidth is because the fast (epi-growth) axis of the laser was parallel to the grating grooves. This means that we illuminated the grating along the slow axis which results in reduced grating coverage and stronger diffraction induced angular spread effect on the collimated beam. According to 5.6 the linewidth for a Gaussian beam should have been 138 Å, however due to the higher transverse orders, diffraction resulted in larger diameter for the collimated beam. However the quality of the coating of the 70 μm device is much improved over the 11 μm device. That is obvious when one looks at the envelope of output power vs wavelength, which shows a very small ripple of 0.025dB, this was obtained by measuring the power output of the external cavity laser, while scanning the grating along the whole tuning range.

Chapter 6

Conclusions

Right below we summarize some of the challenges we had to overcome in the development process as well as present a future direction for this project in order to achieve higher power, room temperature, CW tunable light sources.

6.1 Improvements in fabrication and quantum design

In chapter 3 we went through the steps we took to improve the laser performance by altering the laser design and optimizing the fabrication process. Key challenges and conclusions are highlighted as well as a discussion on new steps we will be undertaking for further improvement of the device performance of this new material system based lasers:

- The waveguide surface roughness is very important. We know about the qual-

ity of our waveguide when we do a length dependence analysis with a large statistical sample. High quality waveguides will give a very small performance spread.

- One challenging characteristic of those lasers is their shorting after operating or being annealed at high current or high temperature. The physical process that is responsible for this is still unknown to us, but a key demonstration showed that devices that turned Ohmic after being operated at high current, recovered after we cleaved out their facets. This does not hold for annealed devices which were not able to recover.

- Increasing the lower cladding thickness to 4 μm was very critical in reducing the substrate leakage loss. Increased upper cladding thickness seemed to reduce the internal loss a_i due to reduced absorption at the metal contact, however the internal quantum efficiency seems to be higher due to increased upper cladding thickness. The benefits of having a thin upper cladding seem to win over the thick upper cladding design, so we are currently looking into new designs that feature thinner upper cladding thickness.

- We analyzed the beneficial effect of compensation doping the GaSb SCH with Te. This resulted in reduced a_i due to reduced IVBT, however the same cannot be said for the p-type doping in the active region which did not seem to affect neither the internal loss a_i nor the threshold current density J_{th}

- We tested the effect of reducing the number of cascades, which showed no

significant improvement in the a_i as well as the J_{th}. That is why in an attempt to further reduce J_{th} we are trying to further increase the confinement factor Γ. We are currently investigating new quantum well designs that have shorter injection regions and "W" type active regions.

- The importance of improving the heat design of the laser is also key. Our threshold current density is still larger than the state of the art ICLs made at the Naval research laboratory[39]. We think that better heat management is necessary for high power ICLs as well as broad area lasers.

- In an ongoing attempt to study the thermal and temperature behavior of the ICLs we presented evidence that there is no temperature dependence of the internal loss[116] in the 240-300 K temperature range. Our results contradict the recent results of Soibel and Kim *et al.*[108, 77]

- Finally we need to figure out the cause of the high temperature ohmic behavior of the lasers, since it is essential to be able to perform robust Au/Sn epi down mounting.

6.2 Improvements on the External cavity configuration

Additionally to the device improvement we are also focused on the external cavity configuration. Currently there are three external cavity improvements we are working on in order to obtain single mode operation.

- First we need to align the laser along the fast axis (rotate by 90 °) with the grating, in order to get better grating linewidth as mentioned in chapter 5.

- However, the grating efficiency is much higher when the electric field is perpendicular to the grooves rather than parallel to them. On the other hand the intrinsic laser polarization is TE for the ICLs. Therefore when the laser is aligned along the fast axis, the electric field is parallel to the grooves and thus low grating feedback is expected. In order to compensate for that, an extra half-wave plate can be inserted in the cavity in between the grating and the collimating lens. This technique has been successfully demonstrated on GaAs lasers[117]. The waveplate enhancement is the second proposed cavity improvement, but requires expensive mid-IR waveplates.

- Third we need to significantly reduce the cavity length. From our calculations we do not anticipate significant improvement if we choose the Littman configuration, however with the Littman configuration we can get a steady output beam from the reflected order of the grating, while in the Littrow configuration we would have to acquire access to the back facet of the laser, which is not very easy, especially if operating below the dew point temperature.

6.3 Coating development

AR coating development was also necessary for this application. Although the coating technology is not new, there are some new challenges that had to be met at

this new wavelength range.

- The first main challenge was to find the right materials that could create broad AR coatings at the wavelength of interest, while matching the effective index n_{eff} of our waveguide.

- The second main challenge comes from the fact that AR coatings are thicker proportionally to their wavelength. That creates delamination and reliability issues due to film stress. This is mainly dealt by evaporating dielectrics that stick well to each other, or by evaporating thin dielectrics between layers with high sticking properties.

- The third main problem is the degradation of the dielectric coating due to the high porosity of the e-beam evaporated films. Ion assisted deposition can be used to solve that problem.

6.4 Future work and final remarks

Throughout this project, the results we were able to demonstrate, show a big promise in the field of Mid-IR spectroscopy. In order for this tunable laser system to have a large commercial impact, important performance improvements need to take place. Our group has already started working towards the improvement of the device efficiency and power output. That can be realized by further reducing J_{th} by increasing the confinement factor Γ through new quantum well designs featuring shorter injection regions and "VV" type active regions. The modal behavior of

the laser needs to be improved by designing single mode waveguides. This can be achieved by reducing the large index step between the ridge and free space, using shallow waveguide trenches, as well as further improving the sidewall roughness in order to further reduce the ridge width. Single mode laser chips would also allow us to implement low reflectivity angled facet devices which do not suffer from lifetime reliability issues. Thermal resistance needs to be further improved so that we can get significant improvement when mounting the devices epi-side down, so that ICLs can be used in high power military applications.

Mid-IR lasers are going to have enormous civilian and military application potential, however their main impact will be in broad tunable light sources for spectroscopy and gas sensing. With their mid-IR emission wavelength they can be used for the detection of methane, ethane, hydrogen chloride, formaldehyde, hydrogen sulfide, nitrous oxide, and carbon monoxide and dioxide, which all have strong absorption lines between 3.3 and 4.6 μm. Methane is the primary component of natural gas, and a room-temperature laser with a narrow emission profile could provide the key component in a methane detector. Similar instruments could map out the distribution of this potent greenhouse gas in the Earth's atmosphere. Although solid-state parametric sources exist, their usefulness is limited by high cost and with some having cryogenic cooling requirements. New low cost semiconductor light sources have been developed based on novel type-II interband cascade diode laser design. We have used interband cascade lasers to design and produce the first interband cascade tunable external cavity laser with a broad tuning range of 300 nm. Our pulsed tunable light source has produced more than 2 mW of peak power at

3.4 and 3.8 μm. This long goal required successful design and fabrication of reliable efficient devices, low reflectivity AR coatings, and optical alignment which can be challenging at this invisible wavelength.

Appendix A

Fresnel reflectivity of a plane wave on a multilayer surface

The following Matlab program evaluates the reflection and transmission coefficient of a multilayered dielectric film:

```
function [r,t] = ref_trans(TEH,kz,k0,n_s,n_c,d_c,n_a)
% ref_trans gives the reflectivity r = E_r/E_i and transmitivity t = E_t/E_i
% of a plane wave incident at angle determined by atan(kz/(n_s*k0)) from a
% substrate of index n_s at given coating with index matrix n_c and
% thickness matrix d_c.  n_a is the ambient index.
%
% Syntax:
% [r,t] = ref_trans(TEH, kz, k0, n_s, n_c, d_c, n_a)
%
% TEH = 'TE' or 'TM' for TE or TM mode calculation
% kz = the kz propagation wavenumber inside the substrate
% k0 = the free space wavenumber
% n_s = kz/k0 the substrate index of refraction
% n_c = the index of refraction matrix of each coating layer.  n_c(1) is
% right next to the substrate and n_c(length(n_c)) is next to the
% ambient environment
% d_c = the thickness matrix of each coating layer.  Similarly d_c(1)
% refers to the layer right next to the substrate and
% d_c(length(d_c) refers to the layer right before the ambient
% medium
% n_a = the index of the ambient medium
%
%


format long g
cmu_inv=1;
N=eye(2);
```

```
kx2 = n_s^2*k0^2-kz^2; %square value of kx which is the same for all layers


kz_c = sqrt(n_c.^2*k0^2-kx2); %kz value for each layer
kz_a = sqrt(n_a^2*k0^2-kx2); %ambient kz value


switch TEH
  case 'TE'
    q_s = -cmu_inv*kz/k0;
    q = -cmu_inv*kz_c/k0;
    q_a = -cmu_inv*kz_a/k0;


    Q_s = [1 1; q_s -q_s];
    Q_s_inv=1/(2*q_s)*[q_s 1; q_s -1];
    Q_a = [1 1; q_a -q_a];


  case 'TM'
    q_s = -cmu_inv*n_s^2*k0/kz;
    q = -cmu_inv*n_c.^2*k0./kz_c;
    q_a = -cmu_inv*n_a^2*k0/kz_a;


    Q_s = [1/q_s 1/q_s; 1 -1];
    Q_s_inv=q_s/2*[1 1/q_s;1 -1/q_s];
    Q_a = [1/q_a 1/q_a; 1 -1];


end
    length_d_c=length(d_c);
    M=zeros(2,2,length_d_c);
    for del = 1:length_d_c


    M(:,:,del) = [cos(kz_c(del)*d_c(del)) i/q(del)*sin(kz_c(del)*d_c(del));...
      i*q(del)*sin(kz_c(del)*d_c(del)) cos(kz_c(del)*d_c(del))];
    end


    for del = 1:length_d_c
    N = N*M(:,:,del);
    end


    N = Q_s_inv*N*Q_a;


    r = N(2,1)/N(1,1);

    t = 1/N(1,1);
```

Appendix B

Interband cascade laser fabrication process

This is the mail recipe for the fabrication of ridge interband cascade lasers:

−Take PR(AZ5214E) from fridge to warm up for 20 mins

−Clean wafer

- −Acetone 30s
- −Methanol 30s
- −IPA 30s
- −Blow dry
- −Put wafer with beaker in the oven for 10mins at 110−120C

−While in oven

- −Clean mask

−rinse with acetone methanol IPA and blowdry or

−If mask is dirty, boil with acetone at 80C for 10mins and then rinse with methanol and isopropanol and blowdry

−Clean chuck for spinner

−Mix developer (AZ400K:DI=1:4=20ml:80ml)

−Mix wet etchant (30ml H3PO4, 30ml H2O2, 90ml DI, 5gr tartaric acid powder)

−Remember to leave solution for 30mins (solution is good for 5hours)

−etch rate ~65A/sec

−Spin coat AZ5214E @4000rpm for 40s

−Soft bake for 1min@90−95C

−Expose at 365nm(Ch.1) for 8s

−Develop sample for about 20−25 secs

−Hard bake @120−125C for 1min

−Wet etch

−There is no etch stop layer so the ridge depth will be determined by the etch time, also etching is isotropic etching for about 7mins and 15secs will result in a ridge about 4.2um deep

−rinse with DI

−Blowdry

−Remove PR with solvent cycle

(acetone−>methanol−>IPA−>blowdry)

−Check under microscope

Take sample clean and without any photoresist to the OXFORD PECVD machine Set parameters for SiN@200C. The growth should be around 10nm/min.

−Grow 4000A of SiN in 40 mins.

After growing 4000A of SiN, we need to pattern the dielectric opening. AZ5214E will not do the job in this case, because the ridges are so deep that we don't get full coverage at the corners resulting to current leakage paths. For that purpose we use SPR220−7

The process for the SPR 220−7 is the following:

−Set the hotplate at 105C

−Spin coat HDMS @3300rpm for 40s

−Spin coat SPR220−7 ramping to 6000rpm for 60s

−proximity bake, by placing wafer on two Q−tip wooden

sticks for 60s on 105C

−remove the wooden sticks and bake for 90s at 105C

−Expose the dielectric opening pattern for 17.5s at Ch.1

−Wait for 45mins−1h for the PR to do its thing

(post exposure bake not necessary)

−develop for 90s in 352 non diluted developper.

−rinse

−blow dry

Use RIE for etching the SiN dielectric opening

−RIE with SF6=40, O2=10, pressure=150, power=100mW

−etch for 70s

−after inspection and making sure the openings are nice and open, remove PR with standard solvent cycle and blow dry.

Once the device is clean and have the openings its time for lift−off patterning For lift−off patterning use the image reversal process which creates undercut which is good metal liftoff.

−Spin coat PR (remember to use HMDS @3300rpm for 40s)

−soft bake @90C

−expose the metal mask for 8secs

(remember the image reversal creates a negative image)

−hard bake @120C

−flood expose without mask at soft contact for 15secs

−develop for 20s(maybe 40s)(inspect while developing)

−Check under microscope

E−beam metal deposition

−Before metal deposition you need to make sure that there are no oxides on the contact interface. Therefore you immerse in a HCl:H2O=1:10 solution for 30secs

−rinse for 30 secs −ebeam deposit Ti/Au (500A/3500A)

−After top contact evaporation, immerse the sample in acetone

−Clean with methanol, isopropanol and blow dry

Mount the laser face down on a glass slide for polishing

−Get a hotplate at 160C

−Clean a small square glass slide with acetone, methanol, isopropanol and blow dry

−place the glass slide on the hotplate

–Use wax that is acetone dissolvable and place the wafer on the glass slide face down.

–Make sure the sample is completely parallel to the glass slide

–Mount the sample on a polishing jig ensuring that the sample is completely on the same plane as the polishing paper.

–Thin the wafer down to about 160um (140um actual thickness, ~20um is the wax thickness in between the wafer and the glass slide)

Appendix C

Ellipsometry theory

In this appendix we present the fundamental theory of ellipsometry used for our film characterization in section 4.3.2. Preceding any index measurement, the exact position of the azimuth angle of the polarizer and the analyzer, in reference to the plane of incidence, must be measured. Assuming that this has already been done for us, and that by convention the 0° corresponds to the p-polarization, we can calculate the light power that reaches the detector, after having reflected from the sample's surface, based on the P and A angles of the polarizer and the analyzer. Considering two main axes, one parallel to the plane of incidence (p) and one perpendicular (s), we can analyze the output of the polarizer:

$$\mathbf{E_i} = \begin{bmatrix} \cos P \\ \\ \sin P \end{bmatrix} E_i \tag{C.1}$$

The reflected field from the dielectric film is:

$$\mathbf{E_r} = \begin{bmatrix} r_p & 0 \\ 0 & r_s \end{bmatrix} \mathbf{E_i} \tag{C.2}$$

The projection of E_r on the axis of the analyzer is:

$$E_a = [\ \cos A \quad \sin A\ ]\mathbf{E_r} \tag{C.3}$$

Once E_a goes through the analyzer, we can analyze it into two s and p components again:

$$\mathbf{E_o} = \begin{bmatrix} \cos A \\ \sin A \end{bmatrix} E_a \tag{C.4}$$

E_a is the amplitude on the output of the analyzer. Its direction is determined by the analyzer, and that is why we treat it as scalar. The light intensity captured by the power detector is:

$$I(A,P) = |\mathbf{E_o}|^2 \tag{C.5}$$

Simple calculations result in the following equation:

$$I = I_0 \left(1 + \frac{|r_p|^2 - |r_s|^2 \tan^2 P}{|r_p|^2 + |r_s|^2 \tan^2 P} \cos 2A + \frac{2\Re e\{r_p^* r_s\} \tan P}{|r_p|^2 + |r_s|^2 \tan^2 P} \sin 2A \right) \tag{C.6}$$

We define ρ as follows:

$$\rho = \frac{r_p}{r_s} = \tan\psi e^{i\Delta} \tag{C.7}$$

Then I becomes:

$$I = I_0 \left(1 + \frac{\tan^2\psi - \tan^2 P}{\tan^2\psi + \tan^2 P}\cos 2A + \frac{2\tan\psi\cos\Delta\tan P}{\tan^2\psi\tan^2 P}\sin 2A\right) = \\ = I_0(1 + a\cos 2A + b\sin 2A) \tag{C.8}$$

The analyzer rotates at 10rpm, while an encoder gives information about the position of the analyzer. At a given polarization angle P we can obtain $I(A)$ which according to the quation above can give us a and b, by doing a Fourier transform. Knowledge of a and b allows us to determine ψ and Δ and therefore ρ. In case of a bulk material we can just substitute the Fresnel equations 4.1 in (C.7) and solve for the material index. In the case of a multilayer coating we would have to synthesize a coating by calculating its reflection coefficients r_p and r_s using (4.42) and using trial and error approach in solving equation (C.7). For that purpose we need to have a rough layer model as a starting point for our synthesis.

As it was mentioned earlier, the polarizer and the analyzer are considered to be aligned with the plane of incidence. That is never true at the begining when we mount a sample, therefore we have to perform a calibration step. For example let us assume that the analyzer angle is:

$$A = A_0 + A' \tag{C.9}$$

the calibration routine would allow us to determine A_0 so that we can compensate A' in order to extract the real azimuth angle with respect to the plane of incidence. If we substitute the equation above into (C.6), and use the following trigonometric identities:

$$\begin{aligned}\cos(a+b) &= \cos a \cos b - \sin a \sin b \\ \sin(a+b) &= \sin a \cos b + \cos a \sin b\end{aligned} \tag{C.10}$$

we obtain the following equation:

$$\begin{aligned}I = I_0 \left(1 + (a\cos 2A_0 - b\sin 2A_0)\cos 2A + (a\sin 2A_0 - b\cos 2A_0)\sin 2A\right) = \\ = I_0 \left(1 + a'\cos 2A + b'\sin 2A\right)\end{aligned} \tag{C.11}$$

We see exactly what we expect. The exact same result but phase shifted, based on the following identity:

$$a\sin x + b\cos x = c\cos(x+d) \tag{C.12}$$

By measuring a' and b' we can determine A_0 as follows:

$$tan2A_0 = \frac{ab' + a'b}{aa' + bb'} \tag{C.13}$$

Assuming P is aligned, then all we have to do is set it to either 0 or $\pi/2$. This would eliminate b and $a = \pm 1$. Thus:

$$tan2A_{0s,p} = \underset{p}{\overset{s}{\pm}}\frac{b'}{a'} \tag{C.14}$$

Like A, P also has some offset. The way to determine the P offset is through a series of measurements. We rotate P and each time we calculate A_0 using (C.13). We do that for a group of P values around the s-polarization as well as around the p-polarization. When a pair of P values such that $P_s - P_p = 90°$ gives $A_{0s} - A_{0p} = 90°$,

then it means that at those particular positions the polarizer is exactly aligned at s or p-polarization. That is how we determine the reference angles for the polarizer and the analyzer azimuth.

Appendix D

List of Publications

1. K. Choi, F. Yesilkoy, A. Chryssis, M. Dagenais, and M. Peckerar, New process development for planar-type cic tunneling diodes, Electron Device Letters, IEEE, vol. 31, no. 8, pp. 809 811, aug. 2010.

2. A. Chryssis, S. Saini, S. Lee, and M. Dagenais, Increased sensitivity and parametric discrimination using higher order modes of etched-core ber bragg grating sensors, Photonics Technology Letters, IEEE, vol. 18, no. 1, pp. 178 180, jan. 2006.

3. A. Chryssis, S. Saini, S. Lee, H. Yi, W. Bentley, and M. Dagenais, Detecting hybridization of dna by highly sensitive evanescent eld etched core ber bragg grating sensors, Selected Topics in Quantum Electronics, IEEE Journal of, vol. 11, no. 4, pp. 864 872, jul. 2005.

4. A. Chryssis, S. Lee, S. Lee, S. Saini, and M. Dagenais, High sensitivity evanescent eld ber bragg grating sensor, Photonics Technology Letters, IEEE, vol.

17, no. 6, pp. 1253 1255, jun. 2005.

5. A. N. Chryssis, G. Ryu, M. Dagenais, F. Towner, J. Bradshaw, and J. Bruno, Measurement of internal quantum eciency and room temperature dependence of gain and loss in interband cascade lasers near room-temperature. IEEE ISLC, Sept 2010.

6. K. Choi, G. Ryu, F. Yesilkoy, A. N. Chryssis, M. Dagenais, N. Goldsman, and M. Peckerar, Surface plasmon and geometry enhanced asymmetric rectifying tunneling diodes, EIPBN, 2010.

7. M. Dagenais, K. Choi, F. Yesilkoy, A. N. Chryssis, and M. Peckerar, Solar spectrum rectication using nano-antennas and tunneling diodes, Photonics West, January 2010.

8. A. N. Chryssis, M. Dagenais, J. D. Bruno, and J. L. Bradshaw, Tunable external cavity interband cascade laser, IEEE LEOS 20th annual meeting, October 2007.

9. M. Dagenais, A. N. Chryssis, and S. Sahand, Incoherent optical frequency domain reectometry for avionics, IEEE LEOS AVFOP, September 2006.

10. A. N. Chryssis, S. S. Saini, S. M. Lee, and M. Dagenais, Enhanced sensitivity to index changes of the surrounding medium for high order modes of etched core ber bragg grating sensors, CLEO/QELS, May 2006.

11. A. N. Chryssis, C. Stanford, J. Hee, W. E. Bentley, P. DeShong, S. S. Saini, and

M. Dagenais, High sensitivity bio-sensor based on etched ber bragg grating, Capital Science, March 2006.

12. M. Dagenais, A. N. Chryssis, S. M. Lee, S. B. Lee, and S. S. Saini, High sensitivity evanescent eld ber bragg grating chemical and biological sensors, OSA topical meeting on Integrated Photonics Research (Invited), April 2005.

13. M. Dagenais, A. N. Chryssis, S. M. Lee, S. B. Lee, W. Bentley, and S. S. Saini, Optical bio-sensors based on etched ber bragg gratings, Photonics West (Invited), January 2005.

14. A. N. Chryssis, S. M. Lee, and M. Dagenais, High sensitivity evanescent eld bragg grating sensor, IEEE LEOS, vol. 1, p. 434, November 2004.

Bibliography

[1] Mit open courseware. [Online]. Available: http://ocw.mit.edu/

[2] S. Tiwari and D. J. Frank, "Empirical fit to band discontinuities and barrier heights in iii-v alloy systems," *Appl. Phys. Lett.*, vol. 60, pp. 630–632, 1992.

[3] J. Faist, F. Capasso, D. L. Sivco, C. Sirtori, A. L. Hutchinson, and A. Y. Cho, "Quantum cascade laser," *Science*, vol. 264, no. 5158, pp. 553–556, 1994. [Online]. Available: http://www.jstor.org/stable/2883703

[4] R. Q. Yang, "Infrared laser based on intersubband transitions in quantum wells," *Superlattice Microst.*, vol. 17, p. 77, 1995.

[5] M. Beck, D. Hofstetter, T. Aellen, J. Faist, U. Oesterle, M. Ilegems, E. Gini, and H. Melchior, "Continuous wave operation of a mid-infrared semiconductor laser at room temperature," *Science*, vol. 295, pp. 301–305, 2002.

[6] J. D. Bruno, J. L. Bradshaw, N. P. Breznay, J. G. Gomes, R. L. Tober, M. S. Tobin, and F. J. Towner, "Interband cascade lasers: progress and outlook," *SPIE Proc.*, vol. 5617, pp. 233–248, 2004.

[7] R. Colombelli, K. Srinivasan, M. Troccoli, O. Painter, C. F. Gmachl, D. M. Tennant, A. M. Sergent, D. L. Sicvo, A. Y. Cho, and F. Capasso, "Quantum cascade surface-emitting photonics crystal laser," *Science*, vol. 302, pp. 1374–1377, November 2003.

[8] C. Sirtori, C. Gmachl, F. Capasso, J. Faist, D. L. Sicvo, A. L. Hutchinson, and A. Y. Cho, "Long-wavelength (lambda 8-11.5um) semiconductor lasers with waveguides based on surface plasmons," *Opt. Lett.*, vol. 23, pp. 1366–1368, September 1998.

[9] J. S. Yu, A. Evans, S. Slivken, S. R. Darvish, and M. Razeghi, "Short wavelength (lambda 4.3um) high-performance continuous-wave quantum-cascade lasers," *IEEE Photonic. Tech. L.*, vol. 17, pp. 1154–1156, June 2005.

[10] J. Faist, F. Capasso, D. L. Sivco, A. L. Hutchinson, S.-N. G. Chu, and A. Y. Cho, "Short wavelength (lambda 3.4 mu m) quantum cascade laser based on strained compensated ingaas/alinas," *Applied Physics Letters*, vol. 72, no. 6, pp. 680–682, 1998. [Online]. Available: http://link.aip.org/link/?APL/72/680/1

[11] D. G. Revin, J. W. Cockburn, M. J. Steer, R. J. Airey, M. Hopkinson, A. B. Krysa, L. R. Wilson, and S. Menzel, "Ingaas/alassb/inp quantum cascade lasers operating at wavelengths close to 3 mu m," *Applied Physics Letters*, vol. 90, no. 2, p. 021108, 2007. [Online]. Available: http://link.aip.org/link/?APL/90/021108/1

[12] J. S. Yu, A. Evans, S. Slivken, S. R. Darvish, and M. Razeghi, "Temperature dependent characteristics of λ 3.8μm room-temperature continuous-wave quantum-cascade lasers," *Appl. Phys. Lett.*, vol. 88, p. 251118, 2006.

[13] R. Teissier, J. Devenson, O. Cathabard, and A. N. Baranov, "Short wavelength quantum cascade lasers emitting around 3μm," *CLEO*, p. CTuF4, 2008. [Online]. Available: http://www.opticsinfobase.org/abstract.cfm?URI=CLEO-2008-CTuF4

[14] I. Vurgaftman and J. R. Meyer, "Analysis of limitations to wallplug efficiency and output power for quantum cascade lasers," *J. of Appl. Phys.*, vol. 99, no. 12, p. 123108, 2006. [Online]. Available: http://link.aip.org/link/?JAP/99/123108/1

[15] A. Lyakh, C. Pflugl, L. Diehl, Q. J. Wang, F. Capasso, X. J. Wang, J. Y. Fan, T. Tanbun-Ek, R. Maulini, A. Tsekoun, R. Go, and C. K. N. Patel, "1.6 w high wall plug efficiency, continuous-wave room temperature quantum cascade laser emitting at 4.6 mu m," *Applied Physics Letters*, vol. 92, no. 11, p. 111110, 2008. [Online]. Available: http://link.aip.org/link/?APL/92/111110/1

[16] S. Slivken, Y. Bai, B. Gokden, S. R. Darvish, and M. Razeghi, "Current status and potential of high power mid-infrarerd intersubband lasers," *SPIE Proc.*, vol. 7608, p. B1, 2010.

[17] Y. Bai, S. Slivken, S. R. Darvish, and M. Razeghi, "Very high wall plug efficiency of quantum cascade lasers," *SPIE Proc.*, vol. 7608, p. F1, 2010.

[18] Y. Bai, S. Slivken, S. Kuboya, S. R. Darvish, and M. Razeghi, "Quantum cascade lasers that emit more light than heat," *Nat. Photon.*, vol. 4, pp. 99–102, 2010. [Online]. Available: http://dx.doi.org/10.1038/nphoton.2009.263

[19] M. Razeghi, S. Slivken, Y. Bai, B. Gokden, and S. R. Darvish, "High power quantum cascade lasers," *New Journal of Physics*, vol. 11, no. 12, p. 125017, 2009. [Online]. Available: http://stacks.iop.org/1367-2630/11/i=12/a=125017

[20] S. Slivken, A. Evans, W. Zhang, and M. Razeghi, "High-power, continuous-operation intersubband laser for wavelengths greater than 10 um," *Applied Physics Letters*, vol. 90, no. 15, p. 151115, 2007, (Jth=0.81 kA/cm2, sl.eff=0.717W/A)@298K. [Online]. Available: http://link.aip.org/link/?APL/90/151115/1

[21] J. Faist, F. Capasso, D. L. Sicvo, A. L. Hutchinson, C. Sirtori, S. N. Chu, and A. Y. Cho, "Quantum cascade laser: Temperature dependence of the performance characteristics and high T_0 operation," *Appl. Phys. Lett.*, vol. 65, pp. 2901–2903, 1994.

[22] J. G. Kim, L. Shtererngas, R. U. Martinelli, G. L. Belenky, D. Z. Garbuzov, and W. K. Chan, "Room-temperature 2.5um ingaassb/algaassb diode lasers emitting 1w continuous waves," *Appl. Phys. Lett.*, vol. 81, pp. 3146–3148, October 2002.

[23] J. G. Kim, L. Shterengas, R. U. Martinelli, and G. L. Belenky, "High-power room-temperature continuous wave operation of 2.7 and 2.8 um in(al)gaassb/gasb diode lasers," *Appl. Phys. Lett.*, vol. 83, pp. 1926–1928, September 2003.

[24] H. K. Choi, G. W. Turner, and S. J. Eglash, "High-power gainassb-algaassb multiple quantum-well diode lasers emitting at 1.9um," *IEEE Photonic. Tech. L.*, vol. 6, pp. 7–9, January 1994.

[25] D. Z. Garbuzov, R. U. Martinelli, H. Lee, P. K. York, R. J. Menna, and J. C. Connolly, "Ultralow-loss broadened-waveguide high-power 2um algaassb/ingaassb/gasb separate-confinement quantum-well lasers," *Appl. Phys. Lett.*, vol. 69, p. 14, July 1996.

[26] D. Z. Garbuzov, H. Lee, V. Khalfin, R. Martinelli, J. C. Connolly, and G. L. Belenky, "2.3-2.7um room temperature cw operation of ingaassb-algaassb broad waveguide sch-qw diode lasers," *IEEE Photonic. Tech. L.*, vol. 11, pp. 794–796, July 1999.

[27] L. Shterengas, G. Belenky, T. Hosoda, G. Kipshidze, and S. Suchalkin, "Continuous wave operation of diode lasers at 3.36 μm at 12 °c," *Applied Physics Letters*, vol. 93, no. 1, p. 011103, 2008. [Online]. Available: http://link.aip.org/link/?APL/93/011103/1

[28] S. Suchalkin, S. Jung, G. Kipshidze, L. Shterengas, T. Hosoda, D. Westerfeld, D. Snyder, and G. Belenky, "Gasb based light emitting diodes with strained

ingaassb type i quantum well active regions," *Appl. Phys. Lett.*, vol. 93, p. 081107, August 2008.

[29] G. L. Belenky, J. G. Kim, L. Shterengas, A. Gourevitch, and R. U. Martinelli, "High-power 2.3 um laser arrays emitting 10 w cw at room temperature," *Electron. Lett.*, vol. 40, pp. 737–738, June 2004.

[30] D. Donetsky, G. Kipshidze, L. Shterengas, T. Hosoda, and G. Belenky, "2.3um type-i quantum well gainassb/algaassb/gasb laser diodes with quasi-cw output power of 1.4w," *Electron. Lett.*, vol. 43, pp. 810–811, July 2007.

[31] P. J. P. Tang, H. Hardaway, J. Heber, C. C. Phillips, M. J. Pullin, R. A. Stradling, W. T. Yuen, and L. Hart, "Efficient 300 k light-emitting diodes at lambda 5 and 8 mu m from inas/in(as[sub 1 - x]sb[sub x]) single quantum wells," *Applied Physics Letters*, vol. 72, no. 26, pp. 3473–3475, 1998. [Online]. Available: http://link.aip.org/link/?APL/72/3473/1

[32] L. Shterengas, G. Kipshidze, T. Hosoda, J. Chen, and G. Belenky, "Diode lasers emitting at 3 μm with 300 mw of continuous-wave output power," *Electron. Lett.*, vol. 45, p. 942, 2009.

[33] R. Q. Yang, "Infrared laser based on intersubband transitions in quantum wells," *Superlattice. Microst.*, vol. 17, no. 1, pp. 77 – 77, 1995. [Online]. Available: http://www.sciencedirect.com/science/article/B6WXB-45R8CBR-41/2/420e2651b51464c6934a5832b0bd8254

[34] J. R. Meyer, I. Vurgaftman, R. Q. Yang, and L. R. Ram-Mohan, "Type-ii and type-i interband cascade lasers," *Electron. Lett.*, vol. 32, pp. 45–46, January 1996.

[35] W. W. Bewley, C. L. Felix, E. H. Aifer, I. Vurgaftman, L. J. Olafsen, J. R. Meyer, H. Lee, R. U. Martinelli, J. C. Connolly, A. R. Sugg, G. H. Olsen, M. J. Yang, B. R. Bennett, and B. V. Shanabrook, "Above-room-temperature optically pumped midinfrared w lasers," *Applied Physics Letters*, vol. 73, no. 26, pp. 3833–3835, 1998. [Online]. Available: http://link.aip.org/link/?APL/73/3833/1

[36] R. Q. Yang, J. L. Bradshaw, J. D. Bruno, J. T. Pham, D. E. Wortman, and R. L. Tober, "Room temperature type-ii interband cascade laser," *Appl. Phys. Lett.*, vol. 81, pp. 397–399, July 2002, 13.2A/cm2, 17

[37] M. Kim, C. L. Canedy, W. W. Bewley, C. S. Kim, J. R. Lindle, J. Abell, I. Vurgaftman, and J. R. Meyer, "Interband cascade laser emitting at lambda = 3.75 mu m in continuous wave above room temperature," *Appl. Phys. Lett.*, vol. 92, no. 19, p. 191110, 2008. [Online]. Available: http://link.aip.org/link/?APL/92/191110/1

[38] C. Canedy, I. Vurgaftman, and J. R. Meyer, "Interband cascade lasers shed their ultra-cool credentials," *Compound semiconductor*, p. 25, 2008.

[39] I. Vurgaftman, C. L. Canedy, C. S. Kim, M. Kim, W. W. Bewley, J. R. Lindle, J. Abell, and J. R. Meyer, "Mid-infrared interband cascade lasers operating at

ambient temperatures," *New J. of Phys.*, vol. 11, pp. 1–13, 2009.

[40] R. Q. Yang, C. Lin, S. J. Murry, S. S. Pei, H. C. Liu, M. Buchanan, and E. Dupont, "Interband cascade light emitting diodes in the 5-8 um spectrum region," *Appl. Phys. Lett.*, vol. 70, pp. 2013–2015, 1997, 15 Cascades 300K pulsed 700nW@77K.

[41] J. R. Meyer, L. J. Olafsen, E. H. Aifer, W. W. Bewley, C. L. Felix, I. Vurgaftman, M. J. Yang, L. Goldberg, D. Zhang, C. Lin, S. S. Pei, and D. H. Chow, "Type ii w, interband cascade and vertical-cavity surface-emitting mid-ir lasers," *IEE Proc. Optoelectron.*, vol. 145, pp. 275–280, October 1998.

[42] S. Suchalkin, M. V. Kisin, S. Luryi, G. Belenky, F. J. Towner, J. D. Bruno, C. Monroy, and R. L. Tober, "Widely tunable type-ii interband cascade laser," *Appl. Phys. Lett.*, vol. 88, p. 031103, December 2006.

[43] E. R. Crosson, K. N. Ricci, B. A. Richman, F. C. Chilese, T. G. Owano, R. A. Provencal, M. W. Todd, J. Glasser, A. A. Kachanov, B. A. Paldus, T. G. Spence, and R. N. Zare, "Stable isotope ratios using cavity ring-down spectroscopy: Determination of 13c/12c for carbon dioxide in human breath," *Analytical Chemistry*, vol. 74, no. 9, pp. 2003–2007, 2002, pMID: 12033299. [Online]. Available: http://pubs.acs.org/doi/abs/10.1021/ac025511d

[44] D. Vogler and M. Sigrist, "Near-infrared laser based cavity ringdown spectroscopy for applications in petrochemical industry," *Appl. Phys. B* -

Lasers O., vol. 85, pp. 349–354, 2006, 10.1007/s00340-006-2313-z. [Online]. Available: http://dx.doi.org/10.1007/s00340-006-2313-z

[45] G. Modugno and C. Corsi, "Water vapour and carbon dioxide interference in the high sensitivity detection of nh3 with semiconductor diode lasers at 1.5 μm," *Infrared Physics & Technology*, vol. 40, no. 2, pp. 93 – 99, 1999. [Online]. Available: http://www.sciencedirect.com/science/article/B6TJ9-3VTS9N9-6/2/e49dc0033a0ac760ba51993165b7b5a0

[46] M. E. Webber, D. S. Baer, and R. K. Hanson, "Ammonia monitoring near 1.5 μm with diode-laser absorption sensors," *Appl. Opt.*, vol. 40, no. 12, pp. 2031–2042, 2001. [Online]. Available: http://ao.osa.org/abstract.cfm?URI=ao-40-12-2031

[47] M. E. Webber, M. Pushkarsky, and C. K. N. Patel, "Fiber-amplifier-enhanced photoacoustic spectroscopy with near-infrared tunable diode lasers," *Appl. Opt.*, vol. 42, no. 12, pp. 2119–2126, 2003. [Online]. Available: http://ao.osa.org/abstract.cfm?URI=ao-42-12-2119

[48] M. Scotoni, A. Rossi, D. Bassi, R. Buffa, S. Iannotta, and A. Boschetti, "Simultaneous detection of ammonia, methane and ethylene at 1.63 μm with diode laser photoacoustic spectroscopy," *Appl. Phys. B - Lasers O.*, vol. 82, pp. 495–500, 2006, 10.1007/s00340-005-2077-x. [Online]. Available: http://dx.doi.org/10.1007/s00340-005-2077-x

[49] L. Rothman, C. P. Rinsland, A. Goldman, S. T. Massie, D. P. Edwards, J. M. Flaud, A. Perrin, C. Camy-Peyret, V. Dana, J. Y. Mandin, J. Schroeder, A. McCann, R. R. Gamache, R. B. Wattson, K. Yoshino, K. V. Chance, K. W. Jucks, L. R. Brown, V. Nemtchinov, and P. Varanasi, "The hitran molecular spectroscopic database and hawks (hitran atmospheric workstation):1996 edition," *J. Quant. Spectrosc. Ra.*, vol. 60, p. 665, 1998.

[50] F. K. Tittel, Y. Bakhirkin, A. A. Kosterev, and G. Wysocki, "Recent advances in trace gas detection using quantum and interband cascade lasers," *Laser Rev.*, vol. 34, p. 275, 2006.

[51] A. A. Kosterev, Y. A. Bakhirkin, R. F. Curl, and F. K. Tittel, "Quartz-enhanced photoacoustic spectroscopy:," *Opt. Lett.*, vol. 27, p. 1902, 2002.

[52] R. G. Dandrea and C. B. Duke, "Calculation of inas/alsb(001) band offsets: Effect of strain and interfacial atomic structure," *Appl. Phys. Lett.*, vol. 63, pp. 1795–1797, 1993.

[53] R. C. Cammarata, "Surface and interface stress effects on the growth of thin films," *J. Electron. Mater.*, vol. 26, pp. 966–968, June 1997.

[54] H. Kroemer, "The 6.1a family (inas, gasb, alsb) and its heterostructures: a selective view," *Physica E*, vol. 20, pp. 196–203, 2004.

[55] I. Vurgaftman, J. R. Meyer, and L. R. Ram-Mohan, "Band parameters for iii-v compound semiconductors and their alloys," *J. Appl. Phys.*, vol. 89, pp. 5815–5875, 2001.

[56] J. R. Meyer, C. A. Hoffman, F. J. Bartoli, and L. R. Ram-Mohan, "Type-ii quantum-well lasers for the mid-wavelength infrrared," *Appl. Phys. Lett.*, vol. 67, pp. 757–759, 1995.

[57] J. Faist, F. Capasso, C. Sirtori, D. L. Sicvo, A. L. Hutchinson, S. N. G. Chu, and A. Y. Cho, "Quantum-well intersub-band electroluminescent diode at lambda=5um," *Electron. Lett.*, vol. 29, pp. 2230–2231, December 1993.

[58] C. R. Pidgeon, C. M. Ciesla, and B. N. Murdin, "Suppression of non-radiative processes in semiconductor mid-infrarerd emitters and detectors," *Prog. Quant. Electron.*, vol. 21, pp. 361–419, 1998.

[59] J. Faist, M. Beck, T. Aellen, and E. Gini, "Quantum-cascade lasers based on a bound-to-continuum transition," *Appl. Phys. Lett.*, vol. 78, pp. 147–149, 2001.

[60] D. Hofstetter, M. Beck, T. Aellen, and J. Faist, "High-temperature operation of distributed feedback quantum-cascade lasers at 5.3um," *Appl. Phys. Lett.*, vol. 78, pp. 396–398, 2001.

[61] J. Faist, F. Capasso, C. Sirtori, D. Sicvo, L. Hutchinson, S. G. Chu, and A. Y. Cho, "Mid-infrared field-tunable intersubband electroluminescence at room temperature by photon-assisted tunneling in coupled-quantum wells," *Appl. Phys. Lett.*, vol. 64, pp. 1144–1146, 1994.

[62] J. Faist, F. Capasso, C. Sirtori, D. L. Sicvo, and A. L. Hutchinson, "Continuous wave operation of a vertical transition quantum cascade laser above t=80k," *Appl. Phys. Lett.*, vol. 67, pp. 3057–3059, 1995.

[63] J. Faist, F. Capasso, C. Sirtori, D. L. Sicvo, J. N. Baillargeon, A. L. Hutchinson, S. G. Chu, and A. Y. Cho, "High power mid-infrared (lambda 5um) quantum cascade lasers operating above room temperature," *Appl. Phys. Lett.*, vol. 68, pp. 3680–3682, 1996.

[64] D. Hofstetter, M. Beck, T. Aellen, J. Faist, U. Oesterle, M. Ilegems, E. Gini, and H. Melchior, "Continuous wave operation of a 9.3um quantum cascsade laser on a peltier cooler," *Appl. Phys. Lett.*, vol. 78, pp. 1964–1966, 2001.

[65] S. Katz, G. Boehm, and M.-C. Amann, "Low-threshold injectorless quantum cascade laser with four material compositions," *Electronics Letters*, vol. 44, no. 9, pp. 580 –580, april 2008.

[66] R. Q. Yang, J. L. Bradshaw, J. D. Bruno, J. T. Pham, and D. E. Wortman, "Mid-infrared type-ii interband cascade lasers," *IEEE J. Quantum Elect.*, vol. 38, pp. 559–568, June 2002, (DEQE=600WPE>16

[67] T. Borca-Tasciuc, D. Achimov, W. L. Liu, G. Chen, H. W. Ren, C. H. Lin, and S. S. Pei, "Thermal conductivity of inas/alsb superlattices," *Microscale Therm. Eng.*, vol. 5, pp. 225–231, 2001.

[68] R. Q. Yang, C. Lin, P. C. Chang, S. J. Murry, D. Zhang, S. S. Pei, S. R. Kurtz, A. Chu, and F. Ren, "Mid-ir interband cascade electroluminescence in type-ii quantum wells," *Electron. Lett.*, vol. 32, pp. 1621–1622, 1996.

[69] R. Q. Yang and S. S. Pei, "Novel type-ii quantum cascade lasers," *J. Appl. Phys.*, vol. 79, pp. 8197–8203, February 1996.

[70] G. G. Zegrya and A. D. Andreev, "Mechanism of suppression of auger recombination processes in type-ii heterostructures," *Applied Physics Letters*, vol. 67, no. 18, pp. 2681–2683, 1995. [Online]. Available: http://link.aip.org/link/?APL/67/2681/1

[71] G. N. Childs, S. Brand, and R. A. Abram, "Intervalence band absorption semiconductor laser materials," *Semicond. Sci. Tech.*, vol. 1, pp. 116–120, 1986.

[72] H. Sakaki, L. L. Change, R. Lideke, C.-A. Chang, G. A. Sai-Halasz, and L. Esaki, "In(1-x)ga(x)as-gasb(1-y)as(y) heterojunction by molecular beam epitaxy," *Appl. Phys. Lett.*, vol. 31, pp. 211–213, 1977.

[73] B. Z. Nosho, W. Barvosa-Carter, M. J. Yang, B. R. Bennett, and L. J. Whitman, "Interpreting interfacial structure in cross-sectional stm images of iii-v semiconductor heterostructures," *Surf. Sci.*, vol. 465, pp. 361–371, 2000.

[74] C. L. Canedy, W. W. Bewley, C. S. Kim, M. Kim, I. Vurgaftman, and J. R. Meyer, "Dependence of type ii "w" mid-infrared photoluminescence and lasing properties on growth conditions," *J. Appl. Phys.*, vol. 94, pp. 1347–1355, 2003, inSb interface results contrast other publications.

[75] C. Mourad, D. Gianardi, K. J. Malloy, and R. Kaspi, "2um gainassb/algaassb midinfrared laser grown digitally on gasb by modulated-molecular beam epitaxy," *J. Appl. Phys.*, vol. 88, pp. 5543–5546, 2000.

[76] W. W. Bewley, J. R. Lindle, C. S. Kim, M. Kim, C. L. Canedy, I. Vurgaftman, and J. R. Meyer, "Lifetimes and auger coefficients in type-ii w interband cascade lasers," *Appl. Phys. Lett.*, vol. 93, no. 4, p. 041118, 2008. [Online]. Available: http://link.aip.org/link/?APL/93/041118/1

[77] W. W. Bewley, J. R. Lindle, C. L. Canedy, M. Kim, C. S. Kim, D. C. Larrabee, I. Vurgaftman, and J. R. Meyer, "Gain, loss, and internal efficiency in interband cascade lasers emitting at lambda=3.6-4.1um," *J. Appl. Phys.*, vol. 103, p. 013114, January 2008.

[78] I. H. Kim, "Pd/ge/pd/ti/au ohmic contact to n-type ingaas," *Mater. Lett.*, vol. 54, p. 323, 2002.

[79] J. A. Robinson and S. E. Mohney, "Pd/ti/au ohmic contact for alsb/inas$_{0.7}$sb$_{0.3}$ heterostructures," *Solid State Electron.*, vol. 50, pp. 429–432, 2006.

[80] C. Heinz, "Ohmic contacts to p- and n-type gasb," *Int. J. Electron.*, vol. 54, pp. 247–254, 1983.

[81] A. Vogt, A. Simon, H. L. Hartnagel, J. Schikora, V. Buschmann, M. Rodewald, H. Fuess, S. Fascko, C. Koerdt, and H. Kurz, "Ohmic contact formation mechanism of the pdgeau system on n-type gasb grown by molecular beam epitaxy," *J. Appl. Phys.*, vol. 83, p. 7715, 1998.

[82] A. Vogt, A. Simon, J. Weber, H. L. Hartnagel, J. Schikora, V. Buschmann, and H. Fuess, "Non-annealed ohmic contacts to p-gasb grown by molecular beam epitaxy," *Mater. Sci. Eng.*, vol. B66, pp. 199–202, 1999.

[83] A. R. Giehl, M. Gumbel, C. Schwender, N. Herhammer, and H. Fouckhardt, "Waveguide based type ii heterostructure photodiode on inas substrate with broad wavelength range photoresponse," *IEEE Photonic. Tech. L.*, vol. 16, pp. 1358–1360, May 2004.

[84] K. Maki, Y. Nakajima, and K. Kinosita, "Stress in vacuum-deposited films of ag, au and cu," *J. Vac. Sci. Technol.*, vol. 6, p. 622, 1969.

[85] C. S. Kim, M. Kim, W. W. Bewley, J. R. Lindle, C. L. Canedy, J. A. Nolde, D. C. Larrabee, I. Vurgaftman, and J. R. Meyer, "Broad-stripe, single-mode, mid-ir interband cascade laser with photonic-crystal distributed-feedback grating," *Appl. Phys. Lett.*, vol. 92, no. 7, p. 071110, 2008. [Online]. Available: http://link.aip.org/link/?APL/92/071110/1

[86] C. L. Canedy, W. W. Bewley, J. R. Lindle, C. S. Kim, M. Kim, I. Vurgaftman, and J. R. Meyer, "High-power and high-efficiency midwave-infrared interband cascade lasers," *Appl. Phys. Lett.*, vol. 88, no. 16, p. 161103, 2006, 5 cascade (WPE=21http://link.aip.org/link/?APL/88/161103/1

[87] M. S. Vitiello, G. Scamarcio, V. Spagnolo, W. W. Bewley, M. Kim, C.-S. Kim, I. Vurgaftman, J. R. Meyer, and A. Lops, "Microprobe photoluminescence assessment of the wall-plug efficiency in interband cascade lasers," *J. Appl. Phys.*, vol. 104, no. 4, p. 046101, 2008. [Online]. Available: http://link.aip.org/link/?JAP/104/046101/1

[88] A. Chandola, R. Pino, and P. S. Dutta, "Below bandgap optical absorption in tellurium-doped gasb," *Semicond. Sci. Tech.*, vol. 20, p. 886, 2005.

[89] C. L. Canedy, W. W. Bewley, M. Kim, J. A. Nolde, D. C. Larrabee, J. R. Lindle, I. Vurgaftman, and J. R. Meyer, "High-temperature interband cascade lasers emitting at lambda=3.6-4.3um," *Appl. Phys. Lett.*, vol. 90, p. 181120, May 2007, 1.15kA/cm2@RT pulsed WPE=273mm.

[90] Y. Hu, "Multilayer dielectric coatings for optoelectonic devices," Ph.D. dissertation, University of Maryland, College Park, 2000.

[91] G. Haas and R. E. Thun, Eds., *Physics of thin films Vol.2.* Academic Press, 1964.

[92] F. K. Reinhart, I. Hayashi, and M. B. Panish, "Mode reflectivity and waveguide properties of double-heterostructure injection lasers," *J. Appl. Phys.*, vol. 42, p. 4466, 1971.

[93] W. Hellmich and P. P. Deimel, "Optimal ar-coating for optical waveguide devices," *J. Lightwave Technol.*, vol. 10, p. 469, 1992.

[94] R. Prakasam, S. Fox, B. P. Gopalan, S. Kareenahalli, P. J. S. Heim, and M. Dagenais, "Practical approach to design and fabrication of antirerflection coatings for semiconductor optical amplifiers," *IEEE Photonic. Tech. L.*, vol. 8, p. 509, 1996.

[95] M. C. Farries, J. Buus, and D. J. Robbins, "Analysis of antireflection coatings on angled facet semiconductor laser amplifiers," *Electron. Lett.*, vol. 26, p. 381, 1990.

[96] J. Buus, M. C. Farries, and D. J. Robbins, "Reflectivity of coated and tilted semiconductor facets," *IEEE J. Quantum Elect.*, vol. 27, p. 1837, 1991.

[97] T. Saitoh, T. Mukai, and O. Mikami, "Theoretical analysis and fabrication of antireflection coatings on laser-diode facets," *J. Lightwave Technol.*, vol. LT-3, p. 288, 1985.

[98] M. C. Hutley, *Diffraction gratings*, N. H. March and H. N. Daglish, Eds. Academic Press, 1982.

[99] M. Fleming and A. Mooradian, "Spectral characteristics of external-cavity controlled semiconductor lasers," *Quantum Electronics, IEEE Journal of*, vol. 17, no. 1, pp. 44 – 59, jan. 1981.

[100] F. Favre and D. L. Guen, "82 nm of continuous tunability for an external cavity semiconductor laser," *Electron. Lett.*, vol. 27, p. 183, 1991.

[101] J. W. R. Trutna and L. F. Stokes, "Continuously tuned external cavity semiconductor laser," *J. Lightwave Technol.*, vol. 11, p. 1279, 1993.

[102] M. G. Littman and H. J. Metcalf, "Spectrally narrow pulsed dye laser without beam expander," *Appl. Optics*, vol. 17, p. 2224, 1978.

[103] K. C. Harvey and C. J. Myatt, "External-cavity diode laser using a grazing-incidence diffraction grating," *Opt. Lett.*, vol. 16, no. 12, pp. 910–912, 1991. [Online]. Available: http://ol.osa.org/abstract.cfm?URI=ol-16-12-910

[104] C. Ye, *Tunable external cavity diode lasers*, T. K. Wei, Ed. World Scientific, 2004.

[105] Z. F. Fan, "Single longitudinal mode external cavity semiconductor lasers and their application in the optical generation of radio grequency signals by heterodyne phase locking." Ph.D. dissertation, University of Maryland, College Park, 1998.

[106] D. Wandt, M. Laschek, A. Tunnermann, and H. Welling, "Continuously tunable external-cavity diode laser with a double-grating arrangement," *Opt. Lett.*, vol. 22, pp. 390–392, March 1997.

[107] S. Suchalkin, J. Bruno, R. Tober, D. Westerfeld, M. Kisin, and G. Belenky, "Experimental study of the optical gain and loss in inas/gainsb interband cascade lasers," *Appl. Phys. Lett.*, vol. 83, pp. 1500–1502, August 2003, temperature effect on gain.

[108] A. Soibel, K. Mansour, Y. Qiu, C. J. Hill, and R. Q. Yang, "Optical gain, loss, and transparency current in high performance mid-infrared interband cascade lasers," *J. Appl. Phys.*, vol. 101, p. 093104, May 2007, ai=35@270K 330A/cm2@270K.

[109] J. W. Crowe and J. R. M. Craig, "Gaas laser inewidth measurements by heterodyne detection," *Appl. Phys. Lett.*, vol. 5, p. 72, 1964.

[110] H. Q. Le, G. W. Turner, J. R. Ochoa, M. J. Manfra, C. C. Cook, and Y. Zhang, "Broad wavelength tunability of grating-coupled external cavity midinfrarerd semiconductor lasers," *Appl. Phys. Lett.*, vol. 69, pp. 2804–2806, 1996.

[111] G. Luo, C. Peng, H. Le, S. Pei, H. Lee, W. Hwang, B. Ishaug, and J. Zheng, "Broadly wavelength-tunable external cavity mid-infrarerd quantum cascade lasers," *IEEE J. Quantum Elect.*, vol. 38, pp. 486–494, may 2002.

[112] R. Maulini, A. Mohan, M. Giovannini, J. Faist, and E. Gini, "External cavity quantum-cascade laser tunable from 8.2 to 10.4 um using a gain element with a heterogeneous cascade," *Appl. Phys. Lett.*, vol. 88, p. 201113, April 2006.

[113] G. Wysocki, R. F. Curl, F. K. Tittel, R. Maulini, J. M. Bulliard, and J. Faist, "Widely tunable mode-hop free external cavity quantum cascade laser for high resolution spectroscopic applications," *Appl. Phys. B-Lasers O.*, vol. 81, pp. 769–777, September 2005.

[114] A. Chryssis, M. Dagenais, J. Bruno, and J. Bradshaw, "Tunable external cavity interband cascade laser," *IEEE LEOS Ann. Mtg.*, pp. 701 –702, oct. 2007.

[115] G. Wysocki and R. Curl, "Widely tunable, high power, mode-hop free, cw external cavity quantum cascade laser at 8.4," *CLEO*, pp. 1 –2, may. 2007.

[116] A. N. Chryssis, G. Ryu, M. Dagenais, F. Towner, J. Bradshaw, and J. Bruno, "Measurement of internal quantum efficiency and room temperature depen-

dence of gain and loss in interband cascade lasers near room-temperature." *IEEE ISLC, Sept 2010.*

[117] H. Lotem, Z. Pan, and M. Dagenais, "Tunable external cavity diode laser that incorporates a polarization half-wave plate," *Appl. Optics*, vol. 31, pp. 7530–7536, January 1992.